University of California Santa Barbara

Magnesium-Doped Gallium Nitride for Electronic and Optoelectronic Device Applications

A dissertation submitted in partial satisfaction
of the requirements for the degree of

Doctor of Philosophy

in

Electrical and Computer Engineering

by

Peter Kozodoy

Committee Members:
    Professor Umesh K. Mishra, Chairperson
    Professor Steven P. DenBaars
    Professor Evelyn L. Hu
    Dr. James Ibbetson

December 1999
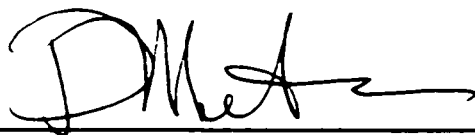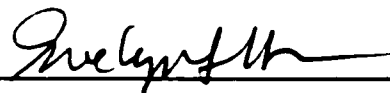
The dissertation of Peter Kozodoy

is approved:

_____

_____

_____

_____
Committee Chairperson

December 1999

Magnesium-Doped Gallium Nitride for Electronic

and Optoelectronic Device Applications

Department of Electrical and Computer Engineering

University of California Santa Barbara

Santa Barbara, CA 93106

Acknowledgments

The solid-state research groups at UCSB form an unusually tight-knit and collaborative community. This is particularly true in the nitrides, and I am glad to have spent my time as a graduate student within this dynamic environment. I am especially grateful to Umesh Mishra for his guidance throughout the years, his constant enthusiasm, and his endless streams of new ideas. I also enjoyed working with Steve DenBaars, and have benefited greatly from his knowledge of MOCVD growth. Evelyn Hu has offered insightful suggestions in many areas; her expertise in processing issues has proved particularly valuable. I have also learned a great deal from discussions with James Ibbetson, whose understanding of deep levels and transport phenomena contributed significantly to many sections of this dissertation.

The members of the Mishra group have been both colleagues and friends. I've enjoyed working closely with Lee and (more recently) Huili on the bipolar project, and many thanks also go to Can, Dan, DJ, Gia, Jae, James, Jeff, Likun, Naiqian, Nguyen, Prashant, Primit, Rama, Rob C., Rob U., Sten, and Yifeng. I'm grateful also to all the York group folks, with whom I've worked in close proximity for lo, these many years.

Thanks are also due to the MOCVD group. I'm grateful to Dave Kapolnek and Stacia & Bernd Keller for getting me started in MOCVD, and I've enjoyed working with all the growers in the lab: Amber, Archie, Beck, Brendan, Casper, Greg, Hugues, Mike C., Mike M., Monica, Patrick, Paul, Tal and Tom. Other collaborators have included Andreas, Darron, Elaine, Fumi, Heike, Kehl, and Pete. I'm grateful to Monica for x-ray measurements, Haus

for AFM, and Lifan for TEM work. I've also benefited from collaboration with the nitride MBE team, including Ben, Chris, Eric, Haus, and Yulia. None of the research at UCSB could proceed without the work of the excellent support staff, which includes Bob and Jack in the clean room, Brian in the MOCVD lab, and Cathy and Lee in Umesh's office (thanks guys!).

Temperature-dependent Hall effect measurements form an important element of this work. These experiments were performed at Wright-Patterson Air Force Base, and I'm grateful to Adam Saxler and William Mitchel out in Dayton for their work on these measurements. Thanks also go out to Lorenzo Faraone and Jarek Antoszewski at the University of Western Australia for preliminary investigations in this area.

A number of close friends have made my time as a grad student much more enjoyable. Many thanks to Amanda, Amit, Gia, Hugues, James, Lee, Mike F., Paul, Rama, and, especially, Alexis.

Vita

December 5, 1972	Born, New York City
May, 1994	B.S., Physics, Yale University, New Haven, Connecticut
1995-1999	Research Assistant, University of California, Santa Barbara
March, 1997	M.S., Electrical and Computer Engineering, University of California, Santa Barbara
December, 1999	Ph.D., Electrical and Computer Engineering, University of California, Santa Barbara

Publications

1. P. Kozodoy, S. P. DenBaars, and U. K. Mishra, "Depletion region effects in Mg-doped GaN." *J. Appl. Phys.* **in press** (2000).

2. P. Kozodoy, L. S. McCarthy, S. P. DenBaars, and U. K. Mishra, "Plasma damage to p-type GaN." *Submitted to Appl. Phys. Lett.*

3. P. Kozodoy, H. Xing, S. P. DenBaars, U. K. Mishra, A. Saxler, R. Perrin, S. Elhamri, and W. C. Mitchel, "Heavy doping effects in Mg-doped GaN." *J. Appl. Phys.* **in press** (2000).

4. I.P. Smorchkova, E. Haus, B. Heying, P. Kozodoy, P. Fini, J. P. Ibbetson, S. Keller, S. P. DenBaars, J. S. Speck, and U. K. Mishra, "Mg doping of GaN layers grown by plasma-assisted molecular beam epitaxy." *Appl. Phys. Lett.* **in press** (2000).

5. S. Chichibu, A. Abare, M. Mack, M. Minsky, T. Deguchi, D. Cohen, P. Kozodoy, S. Fleischer, S. Keller, J. Speck, J. E. Bowers, E. Hu, U. K. Mishra, L. A. Coldren, S. P. DenBaars, K. Wada, T. Sota, and S. Nakamura, "Optical properties of InGaN quantum wells." *Mat. Sci. Eng. B* **59**, 298-306 (1999).

6. M. Hansen, A. C. Abare, P. Kozodoy, T. M. Katona, M. D. Craven, J. S. Speck, U. K. Mishra, L. A. Coldren, and S. P. DenBaars, "Effect of AlGaN/GaN strained layer superlattice period on InGaN MQW laser diodes." *Phys. Status Solidi (a)* **176**, 59-62 (1999).

7. P. Kozodoy, M. Hansen, S. P. DenBaars, and U. K. Mishra, "Enhanced Mg doping efficiency in $Al_{0.2}Ga_{0.8}N$/GaN superlattices." *Appl. Phys. Lett.* **74**, 3681-3 (1999).

8. P. Kozodoy, Y. P. Smorchkova, M. Hansen, X. Huili, S. P. DenBaars, and U. K. Mishra, "Polarization-enhanced Mg doping of AlGaN/GaN superlattices." *Appl. Phys. Lett.* **75**, 2444-6 (1999).

9. J. Limb, L. McCarthy, P. Kozodoy, H. Xing, J. Ibbetson, Y. Smorchkova, S. P. DenBaars, and U. K. Mishra, "AlGaN/GaN HBTs using regrown emitter." *Electron. Lett.* **35**, 1671-3 (1999).

10. L. S. McCarthy, P. Kozodoy, M. J. W. Rodwell, S. P. DenBaars, and U. K. Mishra, "AlGaN/GaN heterojunction bipolar transistor." *IEEE Electron Device Lett.* **20**, 277-9 (1999).

11. G. Parish, S. Keller, P. Kozodoy, J. P. Ibbetson, H. Marchand, P. T. Fini, S. B. Fleischer, S. P. DenBaars, U. K. Mishra, and E. J. Tarsa, "High-performance (Al,Ga)N-based solar-blind ultraviolet p-i-n detectors on laterally epitaxially overgrown GaN." *Appl. Phys. Lett.* **75**, 247-9 (1999).

12. C. Abare, M. P. Mack, M. Hansen, R. K. Sink, P. Kozodoy, S. Keller, J. S. Speck, J. E. Bowers, U. K. Mishra, L. A. Coldren, and S. P. DenBaars, "Cleaved and etched facet nitride laser diodes." *IEEE J. Sel. Top. Quantum Electron. (USA)* **4**, 505-9 (1998).

13. C. Abare, M. P. Mack, M. W. Hansen, R. K. Sink, P. Kozodoy, S. L. Keller, E. L. Hu, J. S. Speck, J. E. Bowers, U. K. Mishra, L. A. Coldren, and S. P. DenBaars, "Pulsed operation of (Al,Ga,In) N blue laser diodes." *Proc. of SPIE Conference on In-Plane Semiconductor Lasers: from Ultraviolet to Mid-Infrared II* San Jose, CA, 103-12 (1998).

14. C.-H. Chen, S. Keller, G. Parish, R. Vetury, P. Kozodoy, E. L. Hu, S. P. Denbaars, U. K. Mishra, and W. Yifeng, "High-transconductance self-aligned AlGaN/GaN modulation-doped field-effect transistors with regrown ohmic contacts." *Appl. Phys. Lett.* **73**, 3147-9 (1998).

15. S. Chichibu, D. Cohen, M. Mack, A. Abare, P. Kozodoy, M. Minsky, S. Fleischer, S. Keller, J. Bowers, U. Mishra, L. Coldren, D. Clarke, and S. Denbaars, "Improved properties of InGaN multiple quantum well purplish-blue laser diodes by Si-doping in the InGaN barriers." *Proc. of 2nd*

International Symposium on Blue Laser and Light Emitting Diodes Chiba, Japan, 381-4 (1998).

16. S. Chichibu, D. A. Cohen, M. P. Mack, A. C. Abare, P. Kozodoy, M. Minsky, S. Fleischer, S. Keller, J. E. Bowers, U. K. Mishra, L. A. Coldren, D. R. Clarke, and S. P. DenBaars, "Effects of Si-doping in the barriers of InGaN multiquantum well purplish-blue laser diodes." *Appl. Phys. Lett.* **73**, 496-8 (1998).

17. S. P. DenBaars, A. C. Abare, M. P. Mack, M. Hansen, R. K. Sink, P. Kozodoy, S. Keller, J. S. Speck, J. E. Bowers, U. K. Mishra, and L. A. Coldren, "Blue InGaN MQW laser diodes on sapphire." *Proc. of IEEE Lasers and Electro-Optics Society 1998 Annual Meeting* Orlando, FL, 346-7 vol.2 (1998).

18. M. Hansen, P. Kozodoy, S. Keller, U. Mishra, J. Speck, and S. DenBaars, "The effect of diode area on the luminescence of InGaN quantum well light emitting diodes grown by MOCVD." *Proc. of 2nd International Symposium on Blue Laser and Light Emitting Diodes* Chiba, Japan, 540-3 (1998).

19. P. J. Hansen, Y. E. Strausser, A. N. Erickson, E. J. Tarsa, P. Kozodoy, E. G. Brazel, J. P. Ibbetson, U. Mishra, V. Narayanamurti, S. P. DenBaars, and J. S. Speck, "Scanning capacitance microscopy imaging of threading dislocations in GaN films grown on (0001) sapphire by metalorganic chemical vapor deposition." *Appl. Phys. Lett.* **72**, 2247-9 (1998).

20. P. Kozodoy, J. P. Ibbetson, H. Marchand, P. T. Fini, S. Keller, J. S. Speck, S. P. DenBaars, and U. K. Mishra, "Electrical characterization of GaN p-n junctions with and without threading dislocations." *Appl. Phys. Lett.* **73**, 975-7 (1998).

21. P. Kozodoy, S. Keller, S. P. DenBaars, and U. K. Mishra, "MOVPE growth and characterization of Mg-doped GaN." *J. Cryst. Growth* **195**, 265-9 (1998).

22. M. P. Mack, A. C. Abare, M. Hansen, P. Kozodoy, S. Keller, U. Mishra, L. A. Coldren, and S. P. DenBaars, "Characteristics of indium-gallium-nitride multiple-quantum-well blue laser diodes grown by MOCVD." *J. Cryst. Growth* **189-190**, 837-40 (1998).

23. M. P. Mack, G. D. Via, A. C. Abare, M. Hansen, P. K. Kozodoy, S. Keller, J. S. Speck, U. K. Mishra, L. A. Coldren, and S. P. DenBaars, "Improvement of GaN-based laser diode facets by FIB polishing." *Electron. Lett.* **34**, 1315-16 (1998).

24. H. Marchand, J. P. Ibbetson, P. T. Fini, P. Kozodoy, S. Keller, S. DenBaars, J. S. Speck, and U. K. Mishra, "Atomic force microscopy observation of threading dislocation density reduction in lateral epitaxial overgrowth of gallium nitride by MOCVD." *MRS Internet J. Nitride Semicond. Res.* **3** (1998).

25. H. Marchand, X. H. Wu, J. P. Ibbetson, P. T. Fini, P. Kozodoy, S. Keller, J. S. Speck, S. P. DenBaars, and U. K. Mishra, "Microstructure of GaN laterally overgrown by metalorganic chemical vapor deposition." *Appl. Phys. Lett.* **73**, 747-9 (1998).

26. L. McCarthy, P. Kozodoy, M. Rodwell, S. Denbaars, and U. Mishra, "A first look at AlGaN/GaN HBTs." *Compound Semicond.* **4**, 16-18 (1998).

27. R. K. Sink, A. C. Abare, P. Kozodoy, M. P. Mack, S. Keller, L. A. Coldren, S. P. DenBaars, and J. E. Bowers, "Pulsed operation of cleaved-facet InGaN laser diodes." *Mat. Res. Soc. Symp. Proc.* **482**, 1197-202 (1998).

28. J. S. Speck, H. Marchand, P. Kozodoy, P. T. Fini, X. H. Wu, J. P. Ibbetson, S. Keller, S. P. DenBaars, U. K. Mishra, and S. J. Rosner, "Microstructure and electronic properties of GaN laterally overgrown by metal organic chemical vapor deposition." *Proc. of 2nd International Symposium on Blue Laser and Light Emitting Diodes* Chiba, Japan, 37-43 (1998).

29. R. D. Underwood, P. Kozodoy, S. Keller, S. P. BenBaars, and U. K. Mishra, "InGaN/GaN field emitters with a piezoelectrically-lowered surface barrier." *Proc. of Eleventh International Vacuum Microelectronics Conference* Asheville, NC, 283-4 (1998).

30. R. D. Underwood, P. Kozodoy, S. Keller, S. P. DenBaars, and U. K. Mishra, "Piezoelectric surface barrier lowering applied to InGaN/GaN field emitter arrays." *Appl. Phys. Lett.* **73**, 405-7 (1998).

31. Y. F. Wu, D. Kapolnek, P. Kozodoy, B. Thibeault, S. Keller, B. P. Keller, S. P. Denbaars, and U. K. Mishra, "AlGaN/GaN MODFETs with low ohmic contact resistances by source/drain n^+ re-growth." *Proc. of IEEE Twenty-Fourth International Symposium on Compound Semiconductors* San Diego, CA, 431-4 (1998).

32. S. P. DenBaars, P. Kozodoy, S. Keller, M. P. Mack, A. Abare, X. Wu, J. S. Speck, and U. K. Mishra, "MOCVD growth of group-III nitrides for high quality photonic devices." *Proc. of 2nd Optoelectronics and Communications Conference* Seoul, South Korea, 48-9 (1997).

33. Z. Dziuba, J. Antoszewski, J. M. Dell, L. Faraone, P. Kozodoy, S. Keller, B. Keller, S. P. DenBaars, and U. K. Mishra, "Magnetic field dependent Hall data analysis of electron transport in modulation-doped AlGaN/GaN heterostructures." *J. Appl. Phys.* **82**, 2996-3002 (1997).

34. F. Hide, M. A. Diaz-Garcia, M. D. McGehee, B. J. Schwartz, P. Kozodoy, S. P. DenBaars, and A. J. Heeger, "Light emission from semiconducting polymers: LEDs, lasers, and white light for the future." *Proc. of SPIE Conference on Organic Light-Emitting Materials and Devices* San Diego, CA, 22-33 (1997).

35. F. Hide, P. Kozodoy, S. P. DenBaars, and A. J. Heeger, "White light from InGaN/conjugated polymer hybrid light-emitting diodes." *Appl. Phys. Lett.* **70**, 2664-6 (1997).

36. D. Kapolnek, S. Keller, R. Vetury, R. D. Underwood, P. Kozodoy, S. P. Den Baars, and U. K. Mishra, "Anisotropic epitaxial lateral growth in GaN selective area epitaxy." *Appl. Phys. Lett.* **71**, 1204-6 (1997).

37. P. Kozodoy, A. Abare, R. K. Sink, M. Mack, S. Keller, S. P. DenBaars, U. K. Mishra, and D. Steigerwald, "MOCVD growth of high output power InGaN multiple quantum well light emitting diode." *Mat. Res. Soc. Symp. Proc.* **468**, 481-6 (1997).

38. M. Kuball, E. S. Jeon, Y. K. Song, A. V. Nurmikko, P. Kozodoy, A. Abare, S. Keller, L. A. Coldren, U. K. Mishra, S. P. DenBaars, and D. A. Steigerwald, "Gain spectroscopy on InGaN/GaN quantum well diodes." *Appl. Phys. Lett.* **70**, 2580-2 (1997).

39. M. P. Mack, A. Abare, M. Aizcorbe, P. Kozodoy, S. Keller, U. K. Mishra, L. Coldren, and S. DenBaars, "Characteristics of indium-gallium-nitride multiple-quantum-well blue laser diodes grown by MOCVD." *MRS Internet J. Nitride Semicond. Res.* **2** (1997).

40. M. P. Mack, A. C. Abare, P. Kozodoy, M. Hanson, S. Keller, U. K. Mishra, L. A. Coldren, and S. P. DenBaars, "MOCVD growth of InGaN multiple quantum well LEDs and laser diodes." *Proc. of Proceedings of the IEEE Twenty-Fourth International Symposium on Compound Semiconductors Compound Semiconductors* San Diego, CA, 367-70 (1997).

41. P. M. Mensz, P. Kellawon, R. Van Roijen, P. Kozodoy, and S. Denbaars, "$In_xGa_{1-x}N/Al_xGa_{1-x}N$ violet light emitting diodes with reflective p-contacts for high single sided light extraction." *Electron. Lett.* **33**, 2066-8 (1997).

42. Y. F. Wu, B. P. Keller, S. Keller, D. Kapolnek, P. Kozodoy, S. P. Denbaars, and U. K. Mishra, "High power AlGaN/GaN HEMTs for microwave applications." *Solid-St. Electron.* **41**, 1569-74 (1997).

43. Y. F. Wu, S. Keller, P. Kozodoy, B. P. Keller, P. Parikh, D. Kapolnek, S. P. Denbaars, and U. K. Mishra, "Bias dependent microwave performance of AlGaN/GaN MODFET's up to 100 V." *IEEE Electron Device Lett.* **18**, 290-2 (1997).

44. Y. F. Wu, B. P. Keller, S. Keller, D. Kapolnek, P. Kozodoy, S. P. Denbaars, and U. K. Mishra, "Very high breakdown voltage and large transconductance realized on GaN heterojunction field effect transistors." *Appl. Phys. Lett.* **69**, 1438-40 (1996).

45. M. R. Deshpande, J. L. Huber, N. H. Dekker, P. Kozodoy, J. W. Sleight, M. A. Reed, C. L. Fernando, W. R. Frensley, R. J. Matyi, and Y. C. Kao, "3-D to 0-D single electron tunneling through bound states of donor impurities in resonant tunneling heterostructures." *Proc. of 22nd International Conference on the Physics of Semiconductors* Vancouver, BC, Canada, 1899-902 vol.3 (1995).

46. M. R. Deshpande, E. S. Hornbeck, P. Kozodoy, N. H. Dekker, J. W. Sleight, M. A. Reed, C. L. Fernando, and W. R. Frensley, "Low-dimensional resonant tunnelling and Coulomb blockade: a comparison of fabricated versus impurity confinement." *Semicond. Sci. Technol.* **9**, 1919-24 (1994).

Abstract

Magnesium-Doped Gallium Nitride for Electronic
and Optoelectronic Device Applications

by Peter Kozodoy

Magnesium doping of gallium nitride (GaN) for p-type conductivity is a crucial technology for a host of optoelectronic and electronic device applications. The performance of many of these devices is presently limited by the various difficulties associated with Mg doping, both fundamental (such as the deep nature of the Mg acceptor) and technological (such as the problems in forming ohmic contacts). Both types of issues are addressed in this work.

Heavy doping effects have been investigated in order to understand the consequences of the high dopant concentration typically employed; increased compensation and a reduction in the acceptor binding energy are among the effects observed. The compensation level is believed to limit the hole mobility in these films, and is found to depend on the choice of growth conditions; the results point to nitrogen vacancies as a likely candidate for one of the compensating donor species.

The optimization of various processing procedures has also been addressed. These include the annealing procedure used to remove the hydrogen passivation as well as ohmic contact recipes. In addition, the electrical effects of plasma-induced damage to the p-type GaN surface are investigated; these effects are particularly important for bipolar transistor applications where a plasma etch is needed in order to reveal the base layer.

The electrical characteristics of GaN *p-n* junctions formed both with and without dislocations are compared using the lateral epitaxial overgrowth technique; the dislocations are found to be the dominant leakage path in reverse-bias operation. The electrical consequences of the deep Mg acceptor are also addressed. These include the unusual nature of the low-frequency depletion region, and dispersion in the high-frequency depletion region due to the finite response time of the Mg acceptor. Finally, a novel scheme is presented that uses the strong polarization fields present in AlGaN/GaN superlattices to enhance the doping efficiency of the Mg acceptor. The polarization fields lead to hole accumulation in parallel sheets, resulting in a spatially-averaged hole concentration that is temperature-stable and significantly enhanced from that obtained in bulk films.

Table of Contents

Chapter 1

Introduction

1.1 Motivation for p-type GaN

Gallium nitride (GaN) and its alloys with aluminum and indium comprise a semiconductor system of great interest for a variety of device applications. The large band-gap tunability of these alloys (figure 1.1) enables optoelectronic devices which operate over the entire visible wavelength range as well as deep into the ultraviolet. GaN also possesses a large breakdown field (E_{bk}) and high electron velocity (v_{sat}), making it an ideal material for high-power, high-frequency electronic devices (table 1.1). Because of the wide band-gap (E_g) of GaN, these devices should be capable of high-temperature operation; the physical robustness of the material will also permit operation in harsh chemical environments.

Conductivity control through doping is an obvious prerequisite for the development of high-performance devices in a new materials system. The p-n junction is a basic building block for the creation of a host of useful devices including light emitting diodes (LEDs), lasers, photodiodes, and bipolar junction transistors (BJTs). While n-type GaN is readily achieved, the development and optimization of p-type GaN has proven more difficult, posing both the practical problem of achieving efficient and controlled doping and the fundamental problem of a deep acceptor energy (ΔE_A), an issue common to many of the wide band-gap materials (table 1.2).

Early breakthroughs in the p-type doping of GaN, and subsequent evolutionary improvements in understanding, have played a major role in catalyzing the rapid development of GaN research in recent years. In the field of

1

light-emitting devices in particular, the tremendous progress made since *p*-type GaN was first achieved in 1989 has already led to new commercial products with very large markets and the potential to revolutionize fields such as optical data-storage and white lighting. Despite this tremendous success, the difficulties associated with *p*-type doping of GaN remain major stumbling blocks in the performance of many devices, particularly bipolar transistors. This dissertation comprises a number of experiments on the growth, processing, and electrical characterization of Mg-doped *p*-type GaN and AlGaN, with the goal of improving device performance through a more complete understanding of the material.
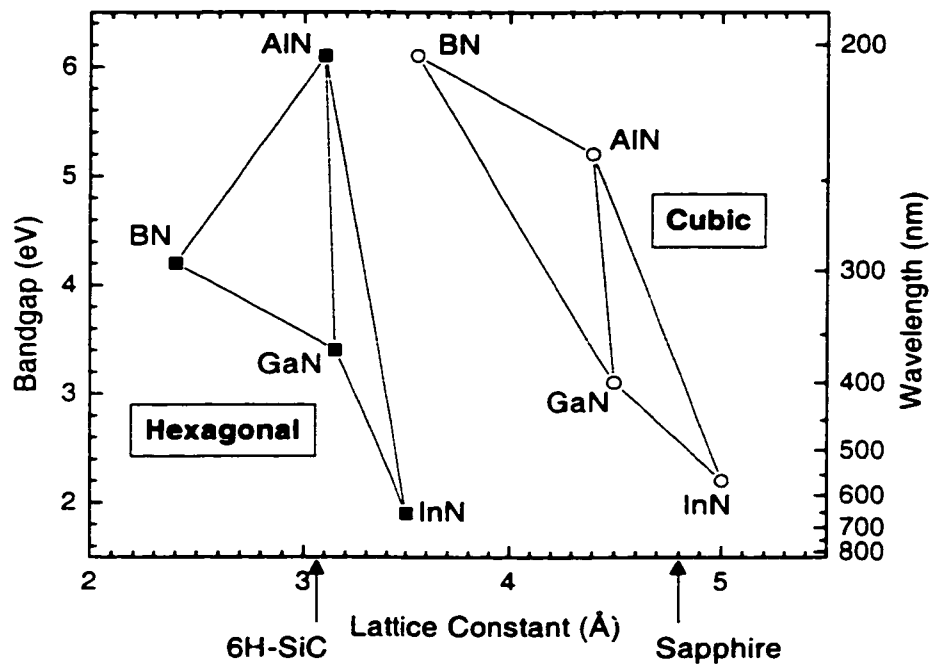

Figure 1.1 Band-gap as a function of lattice constant for the nitride materials system.

1.2 Research background

Although GaN was first created in powder form in 1932,[1] little research occurred in this field until the achievement of hydride vapor phase epitaxy (HVPE)-grown GaN crystals in 1969.[2] These crystals permitted a number of preliminary studies, however device work was still impossible due to the rough surface and poor crystal quality of these heteroepitaxial films. This problem was solved in the early 1980s, when smooth single-crystal wurtzite GaN films were first grown by metalorganic chemical vapor deposition (MOCVD) on sapphire substrates using a thin (~ 200 Å) low-temperature grown "nucleation layer" of AlN or GaN.[3-5] The use of a nucleation layer also reduced the background electron concentration and increased the measured electron mobility in these layers.[6] However, a high threading dislocation density (10^8 to 10^{10} cm^{-2}) remained in these heteroepitaxial films, a problem that persists today and may have a significant impact on electrical properties.

Efforts to produce p-type conduction in GaN layers remained unsuccessful until 1989. A number of acceptor dopants were tried without success; table 1.3 lists the acceptor energy obtained from photoluminescence measurements on GaN films unsuccessfully doped with various potential acceptors.[7] In 1989, Professor Akasaki's group succeeded in producing p-type GaN by subjecting a Mg-doped GaN film to a low-energy-electron-beam-irradiation (LEEBI) treatment—the

	E_g (eV)	E_{bk} (MV/cm)	V_{sat} (cm/s)
Si	1.1	0.3	6×10^6
GaAs	1.4	0.4	1×10^7
InGaP	1.9	0.6	1×10^7
GaN	3.4	2.0	2×10^7 *

Table 1.1 Physical parameters relevant to high-power electronics, presented for various semiconductors. (* Estimated)

3

resulting film had a room temperature hole concentration of $p = 2 \times 10^{16}$ cm^{-3} and mobility $\mu = 8$ cm^2/Vs.[8] Nakamura later confirmed these results, obtaining hole concentrations as high as 3×10^{18} cm^{-3}.[9] In 1992, Nakamura's group discovered that a similar effect could be achieved using a thermal anneal in N_2 instead of electron irradiation.[10] Further research established that the role of the LEEBI or thermal annealing step (hereafter called the "activation step") was to reduce hydrogen passivation of the Mg acceptor.[11,12] It was this hydrogen passivation, which occurs during MOCVD growth, that had prevented successful p-type doping in all previous experiments. In confirmation of this model, Molnar, et al. found that as-grown p-type conductivity was obtained in Mg-doped GaN using hydrogen-free growth techniques such as molecular beam epitaxy (MBE).[13]

The discovery of the activation step for producing p-type GaN led directly to an explosion of GaN-based device work. Nakamura's group led the way in light-emitters, introducing a double-heterostructure LED in 1993, a single quantum well LED in 1995, and the first GaN-based laser diode in 1996.[14] The first GaN-based p-n photodiode was reported in 1995 by Chen, et al.[15] and the first bipolar transistor was produced at the University of California, Santa Barbara (UCSB) in 1998.[16] Research into the properties of p-type GaN continued during these years, and published papers have covered a broad range of subjects

	E_g (eV)	Donor	Acceptor
Ge	0.66	P (12 meV)	B (10 meV)
Si	1.12	P (45 meV)	B (45 meV)
InP	1.35	Si (6 meV)	Zn (20 meV)
GaAs	1.42	Si (6 meV)	Be (28 meV)
SiC (6H)	3.0	N (~ 85 meV)	Al (~ 200 meV)
GaN	3.4	Si (15 meV)	Mg (~ 160 meV)
C (Diamond)	5.5	N (1.7 eV)	B (370 meV)

Table 1.2 Common dopants (and their binding energies) for various semiconductors.

including the optimization of growth conditions, the binding energy of the Mg acceptor, the mechanism of hydrogen passivation, the formation of ohmic contacts, and the study of material properties through Raman and photoluminescence spectroscopy.

The experiments described in this dissertation form a part of this larger research effort to understand the properties of p-type GaN. Our research has always been conducted with the goal of improved device performance in mind. As a result, the experiments have focused mainly on the electrical characterization of Mg-doped GaN, rather than structural or optical characterization.

While early device work focused on LEDs and laser diodes, our research efforts soon shifted towards the fabrication of the first GaN-based bipolar transistor. A comparison of these two device structures (light emitters and bipolar transistors) is shown in figure 1.2. Due to its geometry and the need for high-speed operation, the n-p-n bipolar transistor depends much more critically on the properties of the p-type GaN layer than a p-n diode light emitter does. Among the requirements for the p-type base are high lateral conductivity, low-resistance Ohmic contacts, and sharp dopant profiles for precise junction placement. A low-damage etch technique is needed to reveal the base layer, Mg-doping of alloys is desired in order to implement a graded-base technology, and an understanding of

Dopant	ΔE_A (meV)
Li	750
Be	700
C	860
Mg	250
Zn	340
Cd	550
Hg	410

Table 1.3 Estimated binding energy (from photoluminescence) for various possible acceptors in GaN. From Ref. 7.

the time response of the deep Mg acceptor is important for predicting the high-frequency performance of these devices. These are the concerns which have motivated most of the research in this dissertation. Our goals have been two-fold: to develop a set of recipes for the optimized growth and processing of Mg-doped GaN, and to identify and examine the fundamental issues which are likely to limit device performance.

1.3 Synopsis of the dissertation

Chapters 2 and 3 of this dissertation deal with the practical questions of growth and processing. In chapter 2, the optimization of all MOCVD growth parameters is discussed, with particular attention paid to the Mg-dopant concentration. A detailed study of heavy-doping effects is carried out using temperature-dependent Hall effect measurements. High compensation levels in heavily-doped films are found to play a role in limiting the hole concentration and mobility that are obtained.

Processing issues are addressed in chapter 3, which covers the optimization of activation procedures and a number of experiments on ohmic
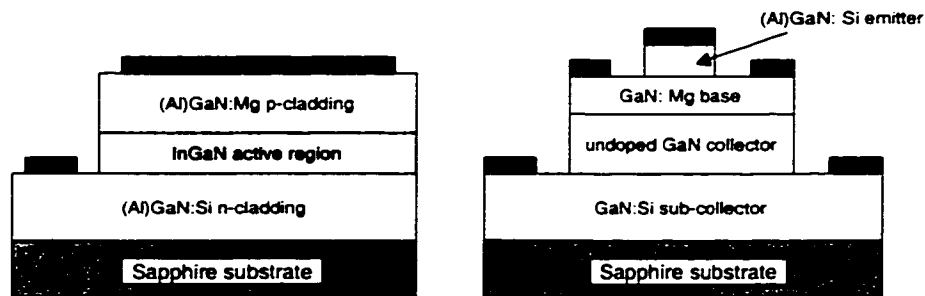
Figure 1.2 Layer structures for GaN-based light emitting devices (left) and bipolar transistors (right).

6

contact formation. The catastrophic degradation of these ohmic contacts which results from plasma exposure of the GaN surface is discussed in detail.

Chapter 4 presents the results of electrical characterization experiments on GaN p-n junctions, which typically exhibit very high reverse-bias leakage currents and junction ideality factors. The leakage current is shown to result primarily from the high density of threading dislocations within the film, and may be drastically reduced by eliminating the dislocations through the use of lateral epitaxial overgrowth (LEO); the ideality factor, however, remains unchanged.

Depletion region effects resulting from the deep nature of the Mg-acceptor are discussed in chapter 5. The DC band-bending is analyzed, and both large- and small-signal dispersion are discussed. The small-signal dispersion in GaN p-n junctions is found to occur at frequencies between 100 kHz and 2 MHz.

Mg-doped AlGaN/GaN superlattices are discussed in chapter 6. These superlattices represent a novel approach that increases lateral conduction by circumventing the carrier freeze-out effect responsible for the low hole concentrations in bulk Mg-doped films. The technique relies on the strong piezoelectric and spontaneous polarization fields that are present in GaN. Both theoretical calculations and experimental results are presented. The measured enhancement in hole concentration over a bulk film is approximately one order of magnitude at room temperature, and greater than five orders of magnitude at reduced temperatures.

It is worth noting that the experiments and calculations described in this dissertation were not performed in the order in which they are presented—instead the organization of the dissertation has been planned for maximum clarity. (For example, the ohmic contact development presented in chapter 3 necessarily preceded the electrical measurements discussed in chapter 2). Any small inconsistencies in experimental procedure or in the values used for calculations

7

must therefore be attributed to a slowly evolving understanding of the material properties of p-type GaN.

1.4 Device results

Since device concerns have dominated the research in this dissertation, it is worth describing some of the device achievements at UCSB that have benefited from the study of p-type GaN presented here.

Early work focused on the growth of blue LEDs with multiple InGaN quantum well active regions.[17] These LEDs, which were processed and packaged by Hewlett-Packard, exhibited a high external quantum efficiency of 4.5%. When operated in pulsed mode to minimize heating, a very high output power of 53 mW was achieved. This value was considerably higher than that obtained from commercially available single quantum well devices, presumably because the multiple quantum well reduced carrier overflow problems. The current-voltage (I-V) characteristics of these diodes were quite poor as a result of an immature p-type contact technology, with an operating voltage above 6 V for a forward current of 20 mA.

An improved contact technology, described in chapter 3, played an important role in the achievement of an electrically-pumped GaN-based blue laser diode in 1997, the first such diode created in any university.[18] The laser emission was centered at 420 nm, and peak output powers as high as 17 mW were achieved in these initial devices. The GaN laser diode is the subject of continued research at UCSB.

GaN and AlGaN-based p-n photodiodes are of great interest for light detection in the ultraviolet wavelength range. In these devices it is important to reduce the dark current of the p-n junction in order to maximize sensitivity. The

experiments described in chapter 4 demonstrated that threading dislocations are the dominant source of leakage current in GaN *p-n* diodes. By reducing the dislocation density in GaN photodiodes using epitaxial lateral overgrowth, leakage currents as low as 10 nA/cm^2 at a reverse bias of 5 V have been achieved.[19] These photodetectors had responsivities as high as 0.05 A/W and a sharp wavelength cutoff at 285 nm.

The first GaN-based BJT was achieved at UCSB in 1998.[16] The common emitter I-V curves for this device, which had a maximum current gain of $\beta = 3$, are shown in figure 1.3. These transistors were processed and tested at UCSB by Lee McCarthy. The low current gain is attributed to a high recombination rate within the neutral base, and the unexpectedly high offset voltage is a consequence of the high base contact and access resistance. As discussed in chapter 3, the plasma etch which is used to reveal the base layer results in a highly damaged
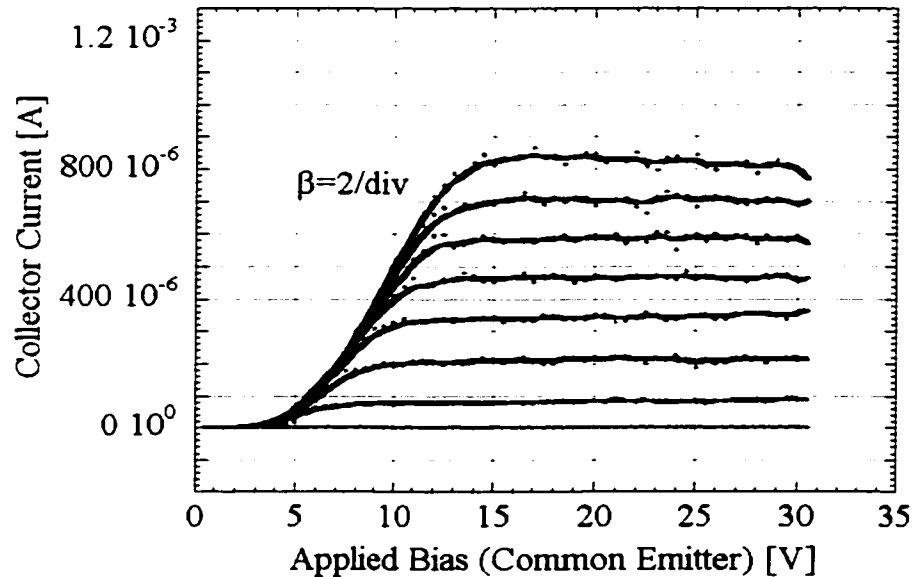

Figure 1.3 Common emitter I-V characteristics of the first GaN-based BJT. The base current increases 50 µA per step, and the device size is 1 µm × 20 µm. From Ref. 16.

surface layer and consequently poor base contacts. Various approaches have been employed to circumvent this problem, including selective re-growth of extrinsic base material to bury the etch damage[16] and selective emitter regrowth on an un-etched base/collector structure.[20] The most recent devices have demonstrated reduced offset voltages, improved stability of the I-V curves, and base-collector breakdown voltages as high as 160V. Because of difficulties in controlling the base width in MOCVD growth (due to the memory effect–see chapter 2), the ongoing device work in this area is focussing primarily on MBE growth. GaN-based bipolar transistors are still in their infancy, and the continuing research in this field is likely to bring both significant improvements in DC characteristics and the achievement of high-frequency device operation in the near future.

1.5 References

1   W. C. Johnson, J. B. Parsons, and M. C. Crew, "Nitrogen Compounds of Gallium III: Gallic Nitride." *J. Phys. Chem.* **36**, 2651-4. (1932).

2   H. P. Maruska and J. J. Tietjen, "The preparation and properties of vapor-deposited single-crystalline GaN." *Appl. Phys. Lett.* **15**, 327-329 (1969).

3   S. Yoshida, S. Misawa, and S. Gonda, "Epitaxial growth of GaN/AlN heterostructures." *J. Vac. Sci. Technol. B* **1**, 250-3 (1983).

4   H. Amano, N. Sawaki, I. Akasaki, and Y. Toyoda, "Metalorganic vapor phase epitaxial growth of a high quality GaN film using an AlN buffer layer." *Appl. Phys. Lett.* **48**, 353-355 (1986).

5   S. Nakamura, "GaN growth using GaN buffer layer." *Jpn. J. Appl. Phys.* **30**, L1705-7 (1991).

6   I. Akasaki and H. Amano, "Crystal growth and conductivity control of group III nitride semiconductors and their application to short wavelength light emitters." *Jpn. J. Appl. Phys.* **36**, 5393-408 (1997).

7   S. Strite and H. Morkoc, "GaN, AlN, InN: A review." *J. Vac. Sci. Technol. B* **10**, 1237-66 (1992).

8   H. Amano, M. Kito, K. Hiramatsu, and I. Akasaki, "P-type conduction in Mg-doped GaN treated with low-energy electron beam irradiation (LEEBI)." *Jpn. J. Appl. Phys.* **28**, L2112-4 (1989).

9   S. Nakamura, M. Senoh, and T. Mukai, "Highly p-typed Mg-doped GaN films grown with GaN buffer layers." *Jpn. J. Appl. Phys.* **30**, L1708-11 (1991).

10

10 S. Nakamura, T. Mukai, M. Senoh, and N. Iwasa, "Thermal annealing effects on p-type Mg-doped GaN films." *Jpn. J. Appl. Phys.* **31**, L139-42 (1992).

11 J. A. Van Vechten, J. D. Zook, R. D. Horning, and B. Goldenberg, "Defeating compensation in wide gap semiconductors by growing in H that is removed by low temperature de-ionizing radiation." *Jpn. J. Appl. Phys.* **31**, 3662-3 (1992).

12 S. Nakamura, N. Iwasa, M. Senoh, and T. Mukai, "Hole compensation mechanism of p-type GaN films." *Jpn. J. Appl. Phys.* **31**, 1258-66 (1992).

13 R. J. Molnar, R. Singh, and T. D. Moustakas, "Blue-violet light emitting gallium nitride p-n junctions grown by electron cyclotron resonance-assisted molecular beam epitaxy." *Appl. Phys. Lett.* **66**, 268-70 (1995).

14 S. Nakamura and G. Fasol, *The Blue Laser Diode* (Springer-Verlag, Berlin, 1997).

15 Q. Chen, M. A. Khan, C. J. Sun, and J. W. Yang, "Visible-blind ultraviolet photodetectors based on GaN p-n diodes." *Electron. Lett.* **31**, 1781-1782 (1995).

16 L. S. McCarthy, P. Kozodoy, M. J. W. Rodwell, S. P. DenBaars, and U. K. Mishra, "AlGaN/GaN heterojunction bipolar transistor." *IEEE Electron Device Lett.* **20**, 277-9 (1999).

17 P. Kozodoy, A. Abare, R. K. Sink, M. Mack, S. Keller, S. P. DenBaars, U. K. Mishra, and D. Steigerwald, "MOCVD growth of high output power InGaN multiple quantum well light emitting diode." *Mat. Res. Soc. Symp. Proc.* **468**, 481-6 (1997).

18 M. P. Mack, A. Abare, M. Aizcorbe, P. Kozodoy, S. Keller, U. K. Mishra, L. Coldren, and S. DenBaars, "Characteristics of indium-gallium-nitride multiple-quantum-well blue laser diodes grown by MOCVD." *MRS Internet J. Nitride Semicond. Res.* **2** (1997).

19 G. Parish, S. Keller, P. Kozodoy, J. P. Ibbetson, H. Marchand, P. T. Fini, S. B. Fleischer, S. P. DenBaars, U. K. Mishra, and E. J. Tarsa, "High-performance (Al,Ga)N-based solar-blind ultraviolet p-i-n detectors on laterally epitaxially overgrown GaN." *Appl. Phys. Lett.* **75**, 247-9 (1999).

20 J. Limb, L. McCarthy, P. Kozodoy, H. Xing, J. Ibbetson, Y. Smorchkova, S. P. DenBaars, and U. K. Mishra, "AlGaN/GaN HBTs using regrown emitter." *Electron. Lett.* **35**, 1671-3 (1999).

Chapter 2

Bulk Mg-doped GaN: Growth and electrical characterization

2.1 Introduction

Mg-doped GaN may be produced using a variety of techniques. The most thoroughly investigated technique is metalorganic chemical vapor deposition (MOCVD), which was used to produce the first successful p-type layers. Since then, many researchers have studied the optimization of Mg-doping by MOCVD and the electrical, optical, and structural properties of the films that have been produced.[1-15] Reported results vary widely, presumably due to differences both in growth conditions and activation procedures. The best reported room temperature resistivity values are in the range 0.1 to 0.3 Ω cm; Yuan, et al. have reported films with a room temperature hole concentration of 5×10^{18} cm^{-3} and mobility 20 cm^2/Vs.[3] Various Mg-containing precursors have been used successfully including biscyclopentadienyl-magnesium (Cp$_2$Mg), bismethyl-cyclopentadienyl-magnesium [(MeCp)$_2$Mg],[16] and bisethylcyclopentadienyl-magnesium [(ECp)$_2$Mg].[9]

Considerable research has also been conducted on the growth of Mg-doped GaN by molecular beam epitaxy (MBE). Some films have been grown using gas source MBE, in which gaseous ammonia is used as the N source.[17-22] However, most research has focused on plasma-assisted MBE, in which an RF-plasma cracked N$_2$ source is used.[23-30] There are also reports on growth of Mg-doped GaN using electron cyclotron resonance (ECR)-cracked N$_2$,[31] and laser-induced MBE in which laser ablation of a metallic Ga target is carried out in a N$_2$ ambient.[32] While the electrical quality of MBE-grown material also varies

considerably, resistivity values as low as 0.2 Ω cm have been reported by plasma-assisted MBE.[23] There is no need for post-growth activation of MBE grown Mg-doped GaN films. The variation in electrical results reported by various groups may stem at least partially from differences in structural quality, which is difficult to control when MBE is used to initiate growth on sapphire.

Mg-doped GaN has also been produced by hydride vapor-phase epitaxy (HVPE)[33,34] and in high-pressure solution bulk crystal growth experiments.[35-37] The latter technique has not yet produced p-type conductivity, but the incorporation of Mg has been used to lower the background n-type carrier concentration, providing highly resistive bulk crystals.

Mg-doping of GaN has also been achieved using post-growth techniques. Ion implantation of Mg in GaN has been studied for some time.[38-43] Early experiments succeeded in producing p-type GaN only through co-implantation of Mg and P.[38] Successful doping through Mg-implantation alone has recently been achieved,[42,43] in one case with the help of a high temperature anneal (1300°C) performed with an AlN cap in order to prevent N loss.[42] Mg-doping has also been reported by vapor phase diffusion in a furnace. This experiment resulted in p-type conductivity, but the measured hole concentration was quite low.[44] The further development of these post-growth Mg-doping technologies will greatly expand the range of possible device geometries and may facilitate the development of GaN-based circuits. However, the techniques are still quite immature, and to date the best electrical properties have been obtained on films which are doped during growth.

We have seen that Mg-doping may be easily achieved during the growth of GaN films, however the electrical properties of the resulting layers differ widely. There are three important factors which may reduce the room temperature hole concentration achieved in any particular Mg-doped GaN film: (1) the deep nature (and consequent partial ionization) of the Mg acceptor, (2) the

presence of compensating donors, and (3) the incorporation of Mg atoms in electrically inactive forms (i.e. not on the desired Ga-substitutional site). The binding energy of the discrete Mg acceptor is a fairly fundamental quantity and cannot be easily adjusted. We therefore turn our attention to the other two effects.

A number of authors have discussed the possibility of compensation in Mg-doped GaN films. Significant compensation levels will reduce both the free hole concentration and the carrier mobility. A compensation level which depends strongly on growth conditions and reactor design may explain the large variations in p-type conductivity reported by various groups. Secondary-ion mass spectroscopy (SIMS) measurements on Mg-doped GaN films do not show unusually high concentrations of any particular impurity, so the compensating donor has been attributed to a native defect or a Mg-related state.[21,45] One candidate is nitrogen vacancies (V_N), which create donor states. Calculations have shown that the formation of such vacancies is much more likely in p-type GaN than in n-type GaN, due to the position of the Fermi level.[46] Kaufmann, et al. have proposed a deep donor formed by a nearest-neighbor associate of a substitutional Mg atom and a nitrogen vacancy.[47]

The incorporation of Mg in non-electrically active sites or in extended clusters is a subject that has received relatively little attention. Reboredo and Pantelides have suggested that Mg interstitials may play a significant role in limiting doping efficiency, and propose a host of Mg-related substitutional/interstitial complexes which may also occur.[48] Neugebauer and Van de Walle, in contrast, have argued that the Mg interstitial, like the incorporation of Mg on a N site, is highly unlikely. They believe the solubility of Mg in GaN may ultimately be limited by the competitive formation of magnesium nitride (Mg_3N_2), particularly at the high growth temperatures employed in MOCVD.[49]

These three important parameters (acceptor binding energy, compensation, and incorporation site) may be studied using various techniques. Of greatest relevance to the ultimate device work are Hall effect measurements. Temperature-dependent Hall effect measurements have been performed by a number of authors in order to measure the acceptor binding energy and estimate the compensation level.[2,5,8,45,50,51] Photoluminescence measurements on Mg-doped GaN have also received considerable attention; most authors appear to agree that the spectra are dominated by donor-acceptor pair recombination, indicating the presence of a compensating donor.[23,47,52-54] Deep level transient spectroscopy (DLTS) studies of deep level states in Mg-doped GaN have produced evidence of various levels within the gap.[55-58] The incorporation site and bonding configuration of Mg in GaN has been studied using Raman spectroscopy[6,59-61] and transmission electron microscopy (TEM).[6,62] Unfortunately, it is difficult to draw any convincing conclusions from this broad array of reported measurements, perhaps because the samples employed have been of widely varying quality and doping level.

The main characterization technique used in this dissertation is Hall effect measurements. Section 2.2 describes the statistics underlying the use of this technique, and section 2.3 describes the experimental setup. The results of Hall effect measurements performed on samples produced under various growth conditions are described in sections 2.6 to 2.9. The results indicate that compensation plays a major role in limiting conductivity, and suggest that the compensation level may be adjusted somewhat through proper choice of growth conditions. Heavy doping effects include a decrease in the measured acceptor concentration, strongly suggesting that Mg incorporates in a non-electrically active form, and a reduction in the acceptor binding energy, which is attributed to a Coulomb interaction.

16

2.2 Doping statistics

In this section we consider the statistics of a bulk GaN layer doped with the deep Mg acceptor (density N_A) and partially compensated with donor states (density N_D). The treatment presented in this section is partially based upon that given in *Electrical Characterization of GaAs Materials and Devices*.[63] The hole concentration and the ionized acceptor concentration are determined using the standard formulas given in equations (2.1) and (2.2). The Boltzmann approximation is used in equation (2.1). E_F represents the energy of the Fermi level, E_V is the energy of the valence band edge, E_A is the energy of the acceptor, g is the degeneracy, k is the Boltzmann constant and N_V is the valence band density of states, given by equation (2.3).

$$p = N_V \exp\left[-\frac{(E_F - E_V)}{kT}\right]$$

(2.1)

$$N_A^- = \frac{N_A}{1 + g\exp\left(\frac{E_A - E_F}{kT}\right)}$$

(2.2)

$$N_V = \frac{2(2\pi m_h^* kT)^{3/2}}{h^3}$$

(2.3)

The equilibrium hole concentration in the bulk is calculated by finding the Fermi energy which satisfies the requirement of charge neutrality. Because of the wide band-gap of GaN we can safely neglect any conduction band electrons and we assume that all the compensating donors are ionized. The charge neutrality condition is therefore:

$$p + N_D = N_A^-$$.

(2.4)

These equations are now combined yielding

$$\frac{p(p + N_D)}{N_A - N_D - p} = \phi,$$

(2.5)

where we define the quantities ϕ and ΔE_A:

$$\phi = \frac{N_V}{g} \exp\left(-\frac{\Delta E_A}{kT}\right), \tag{2.6}$$

$$\Delta E_A = E_A - E_V \ . \tag{2.7}$$

Note that (ϕg) is equal to the hole concentration that is obtained when the Fermi level is coincident with the acceptor energy. The quadratic equation given in (2.5) may be solved for p yielding

$$p = \frac{\phi + N_D}{2}\left[-1 + \sqrt{1 + \frac{4\phi(N_A - N_D)}{(\phi + N_D)^2}}\right]. \tag{2.8}$$

There are three limiting conditions in which Equation (2.8) may be simplified.

Case 1: $\phi \gg N_D$ **and** $\phi \ll (N_A - N_D)$. This is the case when the compensating donor concentration is very small. We can then simplify equation (2.8), yielding:

$$p = \sqrt{(N_A - N_D)\phi} \ . \tag{2.9}$$

Thus, the hole concentration is expected to scale as the square root of the net doping density $N_A - N_D$. A plot of ln (p) vs. $1/T$ should give a straight line with a slope of $-(\Delta E_A / 2k)$, neglecting the small temperature dependence of N_V.

Case 2: $\phi \ll N_D$ **and** $\phi \ll (N_D)^2/(N_A - N_D)$. This is the case when the compensating donor concentration is very high. We can then expand the square root in equation (2.8), yielding:

$$p = \frac{(N_A - N_D)}{N_D}\phi. \tag{2.10}$$

Thus, the hole concentration is expected to scale approximately linearly with the net doping density $N_A - N_D$. In this case, a plot of ln (p) vs. $1/T$ should give a

straight line with a slope of $-(\Delta E_A / k)$, again neglecting the small temperature dependence of N_V.

An interesting consequence of this case arises from considering a system where the compensation ratio r_{comp} is fixed, independent of doping level:

$$r_{comp} = N_D / N_A. \qquad (2.11)$$

In that case equation (2.10) simplifies to

$$p = \frac{(1 - r_{comp})}{r_{comp}} \phi. \qquad (2.12)$$

Thus at high doping levels the hole concentration will actually be fixed and will not depend at all on the dopant densities N_A and N_D, so long as the compensation ratio remains constant.

Case 3: $\phi \gg N_D$ **and** $\phi \gg (N_A - N_D)$. This is the case at very high temperature. Expanding the square root in equation (2.8) we find:

$$p = (N_A - N_D). \qquad (2.13)$$

At very high temperatures all dopants will be ionized and the hole concentration is simply given by the uncompensated acceptor concentration.

In order to apply this analysis to the particular case of Mg-doped GaN there are three quantities that must be known: g, m^*_h, and ΔE_A. Unfortunately, none of these quantities are known with the precision and confidence one would desire.

The valence-band of semiconductors is typically composed of a heavy-hole band, a light-hole band, and a band split off by the spin-orbit interaction. In most bulk cubic semiconductors the heavy-hole and light-hole bands are degenerate, while the split-off band is sufficiently removed in energy that it does not play a role in the doping statistics. Thus a degeneracy value of $g = 4$ is

generally used in p-type semiconductors to account for both the two possible spin states and the heavy-hole/light-hole degeneracy of the valence bands.

In GaN, however, the situation is somewhat more complicated. The wurtzite crystal structure causes a splitting of the heavy-hole and light-hole bands, so that these are no longer degenerate at the Γ point.[64-68] However, this split is quite small (~ 6 meV) so the two bands may be safely considered degenerate at all but the lowest measurement temperatures. Another unusual feature of the GaN valence-band structure is the relative proximity of the split-off band, whose energy separation from the light-hole band is calculated to be between 20 meV and 48 meV.[65-67] While the split-off band is unlikely to play a major role in the doping statistics at room temperature, it may become more prominent at higher temperatures. Ideally, a temperature-dependent degeneracy value g should therefore be used, rising from $g = 2$ at very low temperature to $g = 4$ at intermediate temperatures and $g = 6$ at high temperatures. However such a dependence is difficult to model and complicates experimental data fitting considerably; in the calculations described in this chapter a single temperature-independent degeneracy factor of $g = 4$ has been assumed. Figure 2.1 shows a schematic diagram of the valence band structure of GaN.

The valence band effective mass m^*_h is determined by the curvature of the valence band E-k relations. There is significant variation in reported values for this parameter. Early authors found an effective mass of approximately 0.8 m_0 where m_0 is the free electron mass.[69] More recent work has suggested values of 0.6,[65] 1.1,[64] and 2.2 m_0.[70] This last and highest value is the one used for calculations in this chapter, due to the improved fit it provides to experimental data (see section 2.6). We also note that the hole effective mass is not isotropic— this is evident from the variation in the E-k diagram (figure 2.1) between the $(k_x$, $k_y)$ and k_z directions. (The values of m^*_h listed above are geometrically averaged across the three dimensions). The variation in hole mass between in-plane and

vertical motion is neglected in this dissertation, but the effect may turn out to be of some significance for specific device designs.

The third parameter of interest is the Mg-acceptor energy level ΔE_A. Photoluminescence measurements have placed this value between 203 meV[47] and 250 meV,[71] while temperature-dependent Hall effect measurements have yielded binding energies between 125 meV and 215 meV.[2,5,8,45,50,51] This wide spread in experimental data is likely the result of heavy-doping effects reducing the acceptor binding-energy from that which would be obtained in a very lightly-doped film, a subject which is explored further in section 2.6. An estimate of the expected acceptor binding energy may be obtained from the simple hydrogenic model of the acceptor impurity:

$$\Delta E_A = \frac{m_h^* q^4}{8\varepsilon^2 h^2} = 13.6 \ \mathbf{eV}\left(\frac{m_h^* \varepsilon_0^{\ 2}}{m_0 \varepsilon^2}\right),$$ (2.14)

where q is the electronic charge and ε is the dielectric constant, which is $\varepsilon = 9.5 \ \varepsilon_0$ for GaN.[71] Using values of m^*_h between 0.6 and 2.2 m_0, acceptor binding energies between 90 meV and 332 meV are obtained, a very broad range which
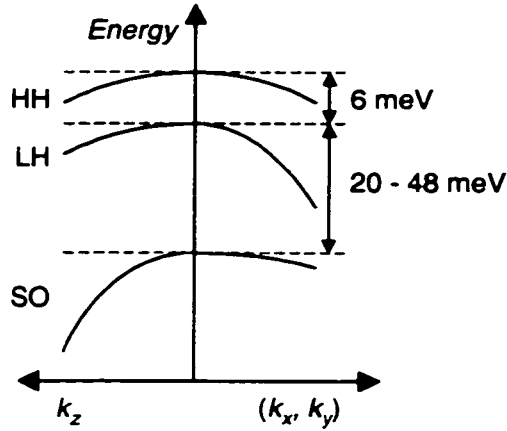

Figure 2.1   Schematic E-k diagram of the valence band of GaN near the Γ point. After Ref. 65.

includes the various measured values. However, we note that hydrogenic model is not expected to be valid at these high effective mass values because the associated Bohr radius is very small—on the order of the lattice constant or even smaller.

Using these values ($g = 4$, $m^*_h = 2.2$ m_0) we can calculate the expected doping efficiency. Figure 2.2 shows the calculated hole concentration at room temperature for an uncompensated Mg-doped GaN layer with various values of ΔE_A. The square-root dependence on dopant density characteristic of uncompensated layers (case 1) is observed.

The valence band density of states is calculated to be $N_V = 8.2 \times 10^{19}$ cm^{-3} at room temperature. For an acceptor binding energy of $\Delta E_A = 160$ meV, this yields $\phi = 4.2 \times 10^{16}$ cm^{-3}. This is a very small value compared to the high doping
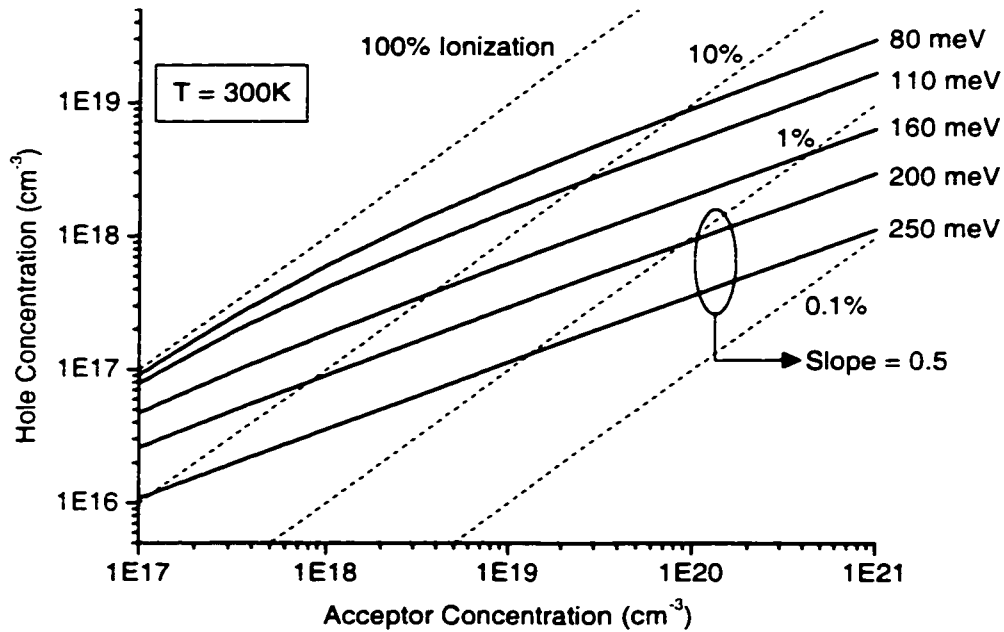

Figure 2.2 Calculated hole concentration as a function of dopant concentration for Mg-doped GaN. The calculations assume no compensation. The acceptor binding energy ΔE_A is varied.

levels (10^{19} to 10^{20} cm^{-3}) that are typically applied in order to achieve sufficient free carriers. Measured values of the compensation ratio (r_{comp}) vary between 6 % and 66 % in different films (see section 2.6). Therefore at room temperature and below, the criteria for case 2 (high compensation) are fulfilled for all but the most lightly-doped films. In general for these films at room temperature we may write the following inequality: $p \ll N_D < N_A$.

The effects of varying compensation levels are displayed in figure 2.3 (for this calculation a binding energy of $\Delta E_A = 160$ meV was assumed). In this figure we observe the saturation in hole concentration which results from a fixed compensation ratio (case 2). The effect may be understood physically as the result of the Fermi level being pinned at a particular energy in order to ionize sufficient acceptors to cancel the space-charge of the compensating donors; this
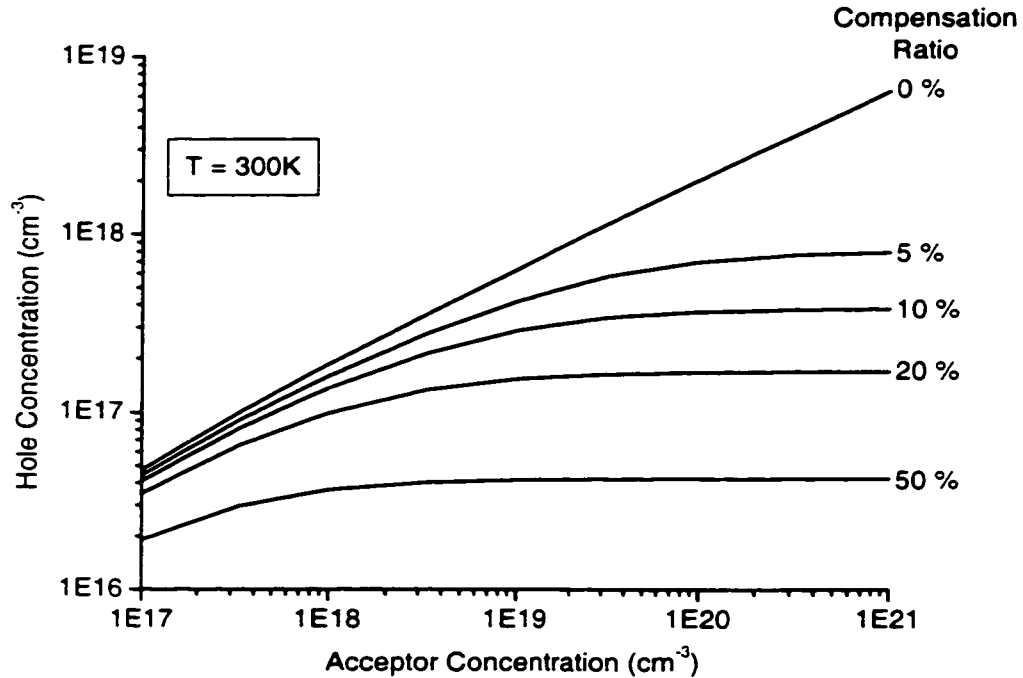

Figure 2.3   Calculated hole concentration as a function of dopant concentration for Mg-doped GaN.   The acceptor binding energy is assumed to be 160 meV; the compensation ratio $r_{comp} = (N_D/N_A)$ is varied.

23

then fixes the number of free holes as well. Since $p \ll N_D$, the ionized acceptor concentration is simply $N_A^- \approx N_D$ and the fraction of acceptors which are ionized is given by r_{comp}. Because this fraction is constant, the Fremi level (and hence the hole concentration) is fixed. The band diagram for this system is shown in figure 2.4.

We observe from figure 2.3 that compensation drastically reduces the hole concentration. This is an important phenomenon that is expected to severely effect conductivity. For example, a sample with 10^{20} cm^{-3} Mg acceptors and 3×10^{19} cm^{-3} compensating donors (leaving 7×10^{19} cm^{-3} net acceptors) will have far fewer holes at room temperature than will a film with 7×10^{19} cm^{-3} Mg acceptors and no compensation.

At the high dopant concentrations typically employed, a number of heavy doping effects may become important. These include such phenomena as valence band-tail states, impurity band formation, and dopant binding energy reduction.[72] These effects will considerably complicate the simple calculations presented here. The role played by such effects in Mg-doped GaN is investigated in section 2.6.

E_C ————————————————

E_D ———————————————— N_D

E_A ———————————————— N_A
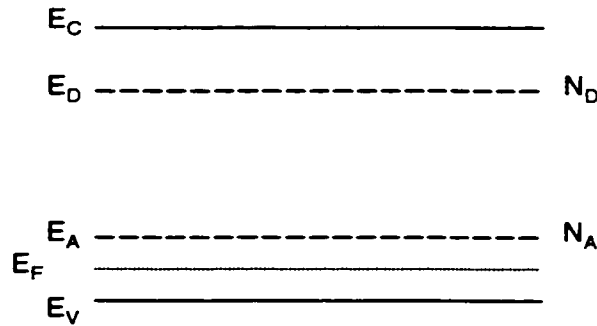E_F ════════════════════
E_V ════════════════════

Figure 2.4   Band diagram for partially-compensated Mg-doped GaN. The position of the Fermi level determines both the fraction of acceptors which are ionized and the density of holes in the valence band.

2.3 Hall effect measurements: experimental setup

Hall effect measurements were performed on Mg-doped GaN samples grown under a wide variety of growth conditions. In every case the Mg-doped layer was grown on a template of n-type GaN (either unintentionally or Si-doped), forming a p-n junction layer structure. Although the use of a p-n junction structure complicates the Hall effect measurements somewhat, it guarantees that the structural quality of the material is the same as that which will be used in devices (where an n-type under-layer is always used). Wu, et al., have shown that the grain structure and dislocation density of heteroepitaxial GaN grown on sapphire is determined during an island growth stage in the initial 0.5μm of GaN deposition on the nucleation layer.[73] Introducing heavy Mg doping during this stage could change the island coalescence process, causing a variation in template quality.

Contacts for the Hall effect measurements were lithographically defined and deposited using thermal evaporation. (The details of the contact scheme are discussed in chapter 3). Cl_2 reactive ion etching was used to isolate the Hall pattern by etching down to the n-type layer. Figure 2.5 shows the current-voltage (I-V) characteristic obtained between two contacts on a Hall pattern. The linear region of the I-V curve represents current flow through the highly resistive p-type layer. At high bias, the reverse-biased p-n junction breaks down under one contact, allowing current to flow through the less resistive n-type layer. The Hall effect measurements were always performed on the linear portion of the I-V curve, so that the current flow was constrained within the p-type layer.

The thickness of the p-type layer was typically 0.5 to 1.0 μm. Any reduction in active thickness of the p-type layer due to the depletion region at the p-n junction was neglected. This effect should be very small due to the very thin nature of the depletion region in Mg-doped GaN (see chapter 5), and at any rate is

25

negligible compared to the uncertainty in layer thickness due to growth rate variations.

Two different mask patterns were employed to perform the Hall effect measurements; these are shown in figure 2.6. In early experiments, the bar geometry was used to measure the Hall factor, and resistivity measurements were performed separately using a TLM pattern (see chapter 3). Later measurements employed a van der Pauw pattern in the shape of a Greek cross, enabling simultaneous resistivity and Hall factor measurements.

In both cases the patterns were kept quite small, as shown. Reliable measurements could not be obtained using standard large devices (several square mm) devices. This was attributed to the presence of a short path somewhere in the device that allowed the current to flow through the n-type layer. Such a path might be caused by a defect caused, for example, by a particle landing on the surface during growth. Using small patterns, a large number of Hall devices
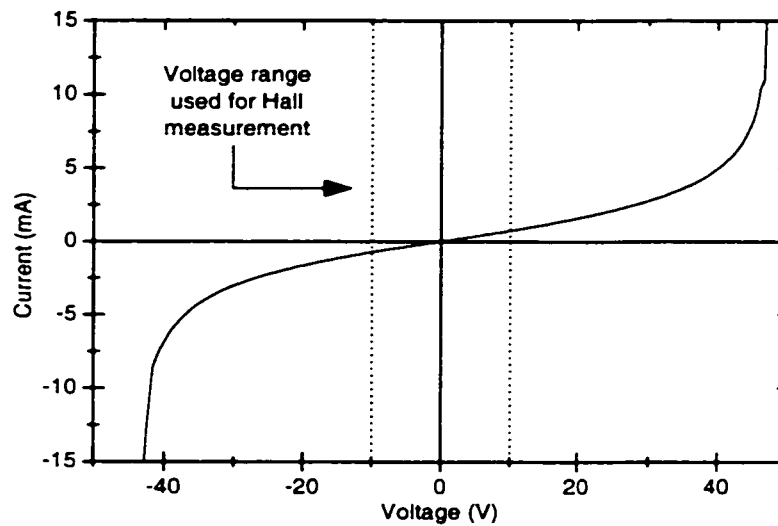

Figure 2.5 I-V characteristic between two contacts on Hall effect device.

could be packed onto a single sample, and the likelihood of any particular device containing such a defect became very low.

A high sample current is desired during the Hall measurement because the Hall voltages can otherwise be quite small and difficult to measure (due to the low hole mobility in these samples). The maximum sample current that can be applied is limited by the useable voltage range (as shown in figure 2.5) and the total resistance between the contacts. It is the need to minimize the total resistance that makes the Greek cross design preferable to other van der Pauw configurations, in which thin arms are used to connect the contact pads to larger Hall mesas. For highly resistive samples the bar geometry is best because it presents the minimum resistance, allowing the highest possible sample current. In this design, the aspect ratio of the bar (length/width) must be at least 3 in order for the full Hall voltage to develop.[63]

The Hall effect measurements performed at UCSB were done at room temperature only. The small devices were contacted using hand-manipulated needle-tip probes and the sample was placed between the poles of an electromagnet. The magnetic field was varied between −0.4 T and 0.4 T during the measurements; sample currents were typically around 30 μA. In all the Hall effect measurements, the hole concentration p was obtained from the measured
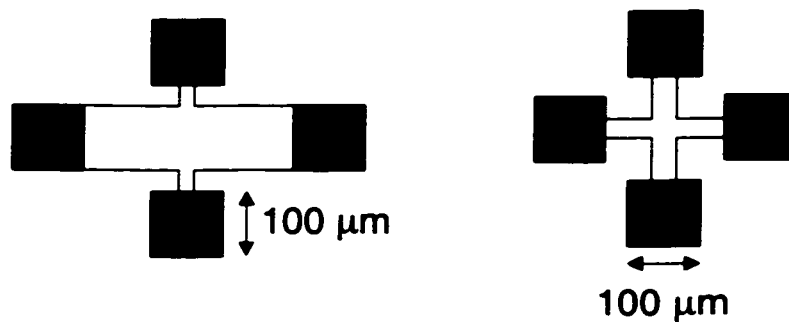

Figure 2.6 Layout of Hall effect measurement devices: bar geometry (left) and van der Pauw geometry (right).

27

Hall coefficient R_H using the equation below, with the Hall scattering factor r_H assumed to be of value unity.

$$p = r_H \, / \, qR_H .$$ (2.15)

Variable-temperature Hall effect measurements were performed on a few samples at Wright-Patterson Air Force Base in conjunction with Adam Saxler and William C. Mitchel. Separate apparatuses were used for the measurements above and below room temperature. Magnetic fields up to 1 T could be applied during high-temperature measurements and up to 2 T were used in the low-temperature measurement rig.

The preparation of these samples was fairly complicated because the measurement setup was designed for larger contact pads. In order to perform the measurements the samples were attached to sapphire carrier wafers using a high-temperature cement (Omegabond). Wire-bonding was performed to connect the contact pads on the sample with large gold contact pads that had been deposited on the sapphire carrier. Prior to the cementing, an extra thick (1 μm) gold layer was added to the contact pads and the contacts were annealed at 450°C in N_2 (2 minutes); these steps helped the bond wires to stick and kept the contact pads from peeling off during bonding. Figure 2.7 shows a diagram of a sample prepared for variable-temperature Hall effect measurements.
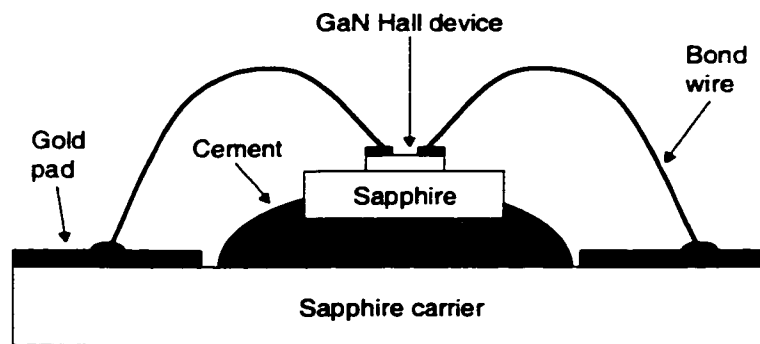

Figure 2.7 Drawing of sample mounted for variable-temperature measurements (not to scale).

2.4 MOCVD growth conditions

All the growths described in this dissertation were performed on the modified Thomas Swan MOCVD growth machine at UCSB. This is a horizontal quartz reactor with separate the group V and group III input flows, designed in order to reduce pre-reactions. The wafer is held in a graphite susceptor and the growth temperature is measured using a thermocouple placed within the susceptor. The pressure during growth may be controlled between atmosphere and approximately 30 torr. During typical GaN growth conditions, the gas ambient is composed primarily of NH_3, in addition to H_2 and N_2 (usually mainly H_2). All of these gasses are purified before entering the growth chamber. The metalorganic sources used are trimethylgallium (TMGa), trimethylaluminum (TMAl), trimethylindium (TMIn), and biscyclopentadienyl-magnesium (Cp_2Mg). Silicon doping is accomplished with a gas source of dilute disilane in H_2.

Considerable effort has been invested by a number of researchers at UCSB in optimizing the GaN growth process in this MOCVD reactor. Growth is usually performed on c-plane sapphire substrates, which are etched in a high temperature (1050°C) H_2 step prior to nucleation layer deposition. Undoped GaN films prepared in this reactor exhibit a background carrier concentration around $n = 4\times10^{16}$ cm^{-3}, mobility as high as 820 cm^2/Vs, typical x-ray diffraction peak widths of 270 on-axis (002) and 390 off-axis (102), and threading dislocation density between 10^8 and 10^9 cm^{-2}, as measured by transmission electron microscopy (TEM). This reactor has been used to grow almost all the GaN-based device structures produced at UCSB to date, including LEDs, lasers, photodetectors, high electron mobility transistors, bipolar transistors, and field emitters.

Each metalorganic source is kept in a temperature-controlled bath. For Cp_2Mg, the manufacturers (Morton Chemical and Air Products) quote the

following formula for vapor pressure (p_{Cp_2Mg}) in torr as a function of bubbler temperature (T_{Cp_2Mg}) in Kelvin:

$$\log_{10}\left(p_{Cp_2Mg}\right) = 25.14 - 2.18\ln T_{Cp_2Mg} - \frac{4198}{T_{Cp_2Mg}}, \qquad (2.16)$$

This formula is plotted in figure 2.8; its accuracy is not known.

In practice, two bubbler temperatures were used: 45.2°C and 25.2°C. The bubbler pressure was kept at 1200 torr. The source pick-up efficiency has been calculated using equation (2.16), yielding 1.6 nmol per standard cubic centimeter (scc) at 25.2°C and 9.0 nmol per scc at 45.2°C. The advantages of the lower bubbler temperature are that it allows a finer adjustment of the input source flow and is more convenient when a slow growth rate is needed. An additional benefit may be that it helps reduce problems with condensation of Cp₂Mg in any cold plumbing sections. During all growths the TMGa bubbler temperature was kept
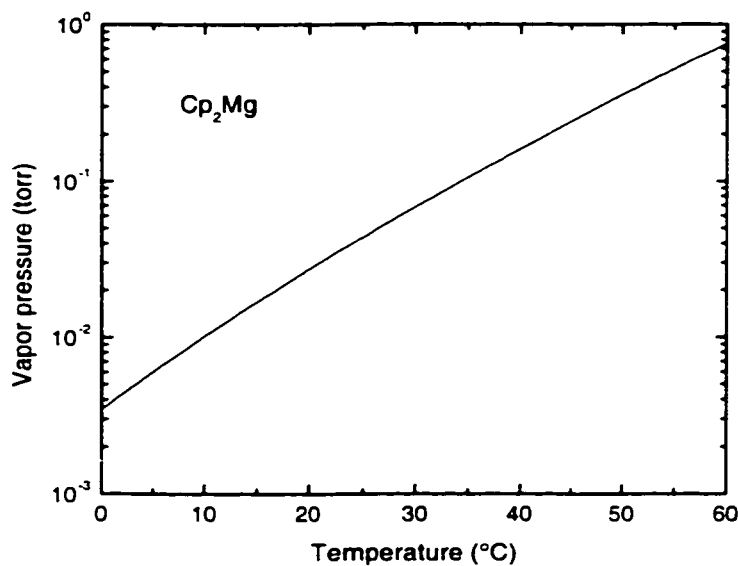

Figure 2.8 Plot of vapor pressure versus bubbler temperature for Cp₂Mg source.

at $-10°C$, corresponding to a pick-up efficiency of 1.5 μmol per scc for this source material.

In this chapter we discuss the effect of varying many different growth parameters. These are variations based on a standard set of growth conditions—these standard conditions were used to grow Mg-doped GaN for a number of experiments. For example, all the processing experiments described in chapter 3 were performed on samples grown under these conditions. Hall effect measurements on films grown under these conditions typically yield hole concentrations between 5×10^{17} cm^{-3} and 1×10^{18} cm^{-3}. Table 2.1 lists the various parameters for the "standard" growth conditions.

Several types of non-uniformity and irreproducibility plagued the research on MOCVD growth of Mg-doped GaN, even under nominally identical growth conditions. Foremost among the difficulties was a severe growth rate non-uniformity within the reactor—up to a factor of two across the width of the sample (2 cm). This results in significant uncertainty in the thickness of the layers, which can lead to errors in interpreting Hall measurement data, and makes it difficult to assess the results of various processing experiments, such as studies

Standard growth conditions	
Cp$_2$Mg Temp.	45.2°C
TMGa flow rate	13.1 sccm 19.3 μmol/min Growth rate: 1-2 μm/hr
Cp$_2$Mg flow rate	15 sccm 135 nmol/min
Growth Temp.	1000°C
Pressure	760 torr

Table 2.1 "Standard" growth conditions for Mg-doped GaN.

of different activation conditions. Temperature non-uniformity across the wafer, and temperature drift over time, were also believed to be significant issues (although this is difficult to quantify). The growth rate and flow pattern of the gasses varied considerably over time as the reactor liners were removed for cleaning or replaced altogether. A final potential source of non-uniformity is variation over time in the amount of condensation of Cp_2Mg in the plumbing or the unheated zones of the reactor chamber; it is not yet clear how important this effect may be. Throughout this research every effort was made to correct for any drifting growth conditions, and to adjust experimental measurements to minimize the error introduced by non-uniformity.

2.5 SIMS measurements

The incorporation of Mg during GaN growth has been studied using secondary ion mass spectroscopy (SIMS) measurements. For these studies thick Mg-doped layers were grown either individually or in multi-layer stacks. The Cp_2Mg bubbler temperature was kept at 45.2°C during these growths. The SIMS measurements were performed at Charles Evans East, where implanted standards were used to calibrate the measurements.

Figure 2.9 shows the measured Mg concentration in samples grown with various Cp_2Mg flows, and for two different reactor pressure values. The Mg content is found to increase linearly with Cp_2Mg flow, as expected. However, the incorporation efficiency is found to depend on the reactor pressure. For these layers the Mg incorporation efficiency is calculated to 24% of the Ga incorporation efficiency during atmospheric pressure growth; at 76 torr, this value rises to 32%. Because the GaN growth rate is independent of pressure in this reactor, the results indicate more efficient Mg incorporation during low-pressure

growth. At first, we attributed this effect to a parasitic pre-reaction between NH_3 and Cp_2Mg, which was suppressed at low pressure. Such a pre-reaction had been proposed by Haffouz, et al.[16], but later investigations by Bartram demonstrated that such pre-reactions do not actually occur.[74] The origin of this effect therefore remains uncertain. One possible explanation is Cp_2Mg condensation in the unheated portions of the stainless-steel plumbing and quartz reactor chamber directly upstream of the susceptor; such condensation would be suppressed during low-pressure growth due to the lower Cp_2Mg partial pressure.

Figure 2.10 shows SIMS measurements of the Mg concentration as the TMGa flow (and hence the growth rate) was varied. Once again, layers were grown both at atmospheric pressure and at 76 torr. During these growths the Cp_2Mg flow was scaled with the TMGa flow to keep the nominal doping level constant. As expected, the measured Mg concentration shows no dependence on the growth rate at either pressure. Again, the Mg incorporation efficiency is
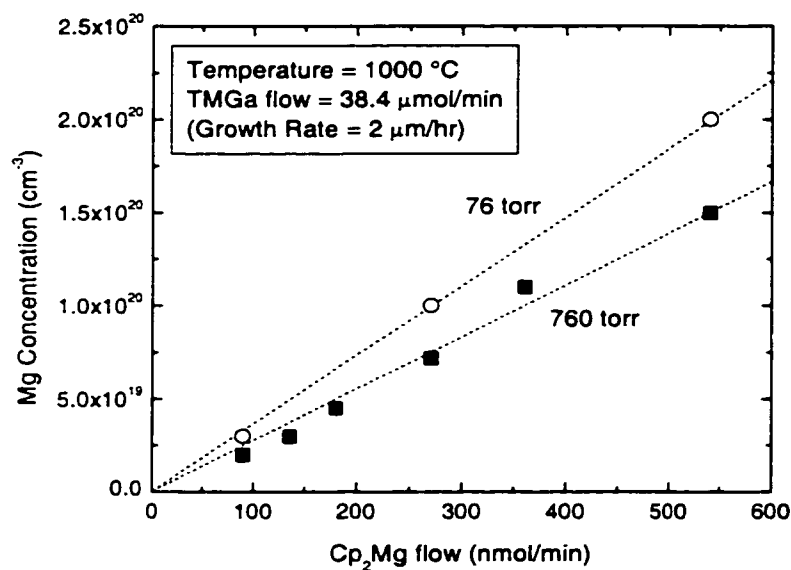

Figure 2.9 SIMS measurements of Mg concentration as a function of Cp2Mg flow during growth.

found to be lower during atmospheric pressure growth—in this series, the Mg incorporation efficiency is 13% that of Ga at 760 torr, and 32% at 76 torr. The incorporation efficiency at atmospheric pressure is reduced in these layers from that observed in figure 2.9. The origin of these variations is not known, but may be related to a varying degree of Cp_2Mg condensation due to subtle differences in reactor geometry between the various quartz reactor liners used.

The effect of growth temperature was also studied, this time using only layers grown at atmospheric pressure. The SIMS measurements are presented in figure 2.11, and show no significant variation in Mg concentration with growth temperature.

Overall, the SIMS measurements indicate that Mg-doping of GaN using Cp_2Mg is quite a well-behaved process. The incorporation efficiency is independent of Cp_2Mg flow, growth rate, and growth temperature within the range of experimental testing, and depends only on the reactor pressure. SIMS
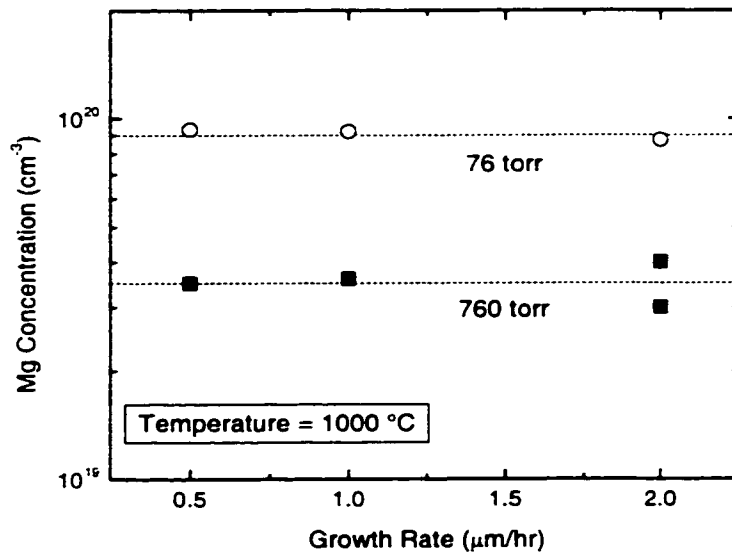

Figure 2.10   SIMS measurements of Mg concentration as a function of GaN growth rate.

measurements showed no increase in the levels of common impurities such as C, O, and Si as a result of the Mg doping. The H concentration did increase considerably in Mg-doped films compared to undoped layers, but this is an expected consequence of the dopant passivation. Finally, however, it must be noted that despite the consistent and stable SIMS results that were obtained in these short studies, over longer time scales (several months) large changes in the incorporation efficiency were observed. Again, these variations are attributed to a changing gas-flow profile due to the regular removal and replacement of the quartz reactor liner.
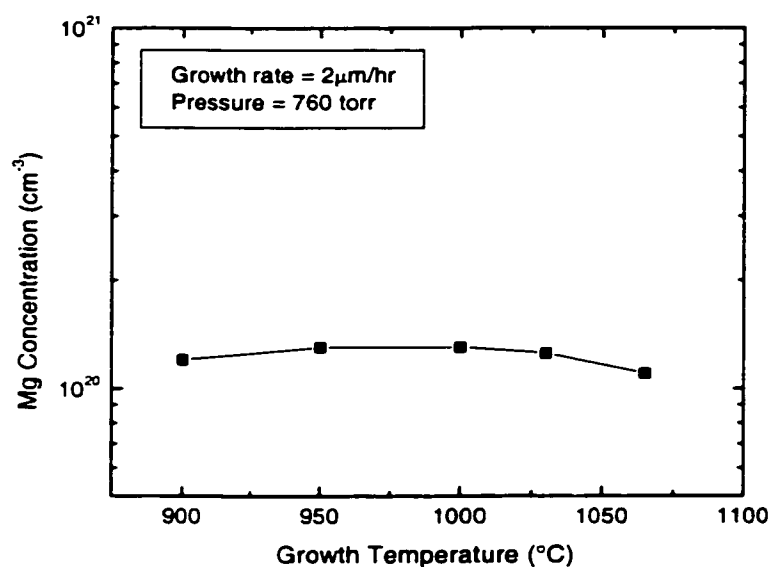

Figure 2.11 SIMS measurements of Mg concentration as a function of growth temperature.

2.6 Effect of Cp₂Mg flow: An investigation of heavy doping effects

This section describes studies performed on samples with a range of Mg-doping levels. The goal was both to identify the optimum dopant concentration and to study the evolution of heavy-doping effects below and above this point. These samples were analyzed using temperature-dependent Hall effect measurements.
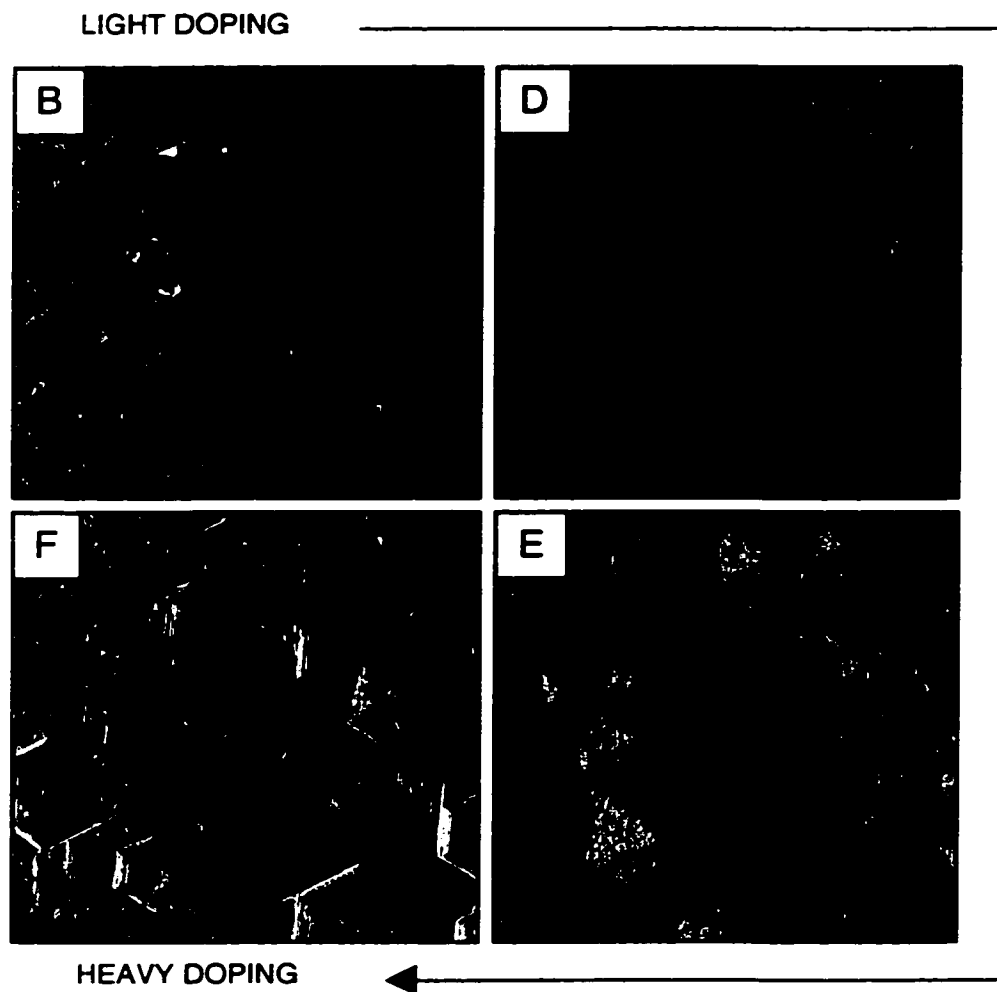

Figure 2.12 AFM amplitude images of Mg-doped GaN samples. Each image is 50 μm × 50 μm.

The Cp_2Mg bubbler temperature was 25.2°C during these growths. The Mg-doping level was varied by changing the flow of Cp_2Mg from 15 sccm to 263 sccm (24 to 428 nmol/min). In all samples the TMGa flow was 13.1 sccm (19.3 μmol/min). The Mg-doped layers were grown at 1010°C and at atmospheric pressure. SIMS measurements confirmed that the Mg concentration scaled roughly with Cp_2Mg flow; the measured values varied between 2×10^{19} and 8×10^{20} cm^{-3}. The Mg concentration in the most heavily doped sample (F) is estimated to be about 2% of the Ga concentration. On the lightly-doped samples, a thin (300 Å) heavily-doped cap layer was needed in order to produce ohmic contacts. For Hall effect measurements this cap layer was etched away using a low-power Cl_2 reactive ion etch.

Figure 2.12 shows the surface morphology of samples grown at various Cp_2Mg flows (these samples were grown without the heavily-doped cap layer). These amplitude-mode atomic force microscopy (AFM) images of the p-GaN
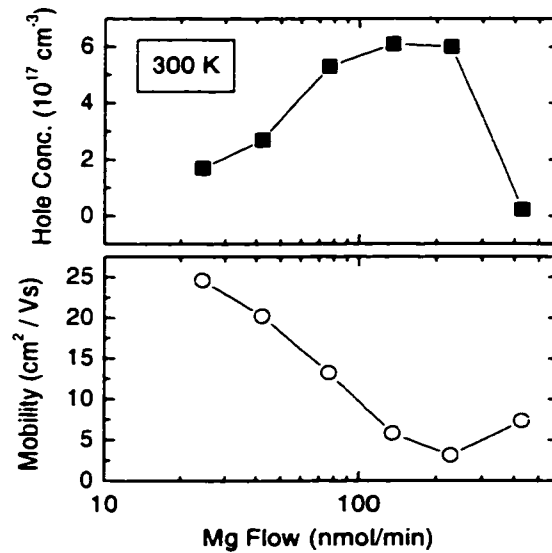

Figure 2.13 Room temperature Hall effect measurements on Mg-doped GaN samples.

37

surface were produced by Erik Haus at UCSB. The heavy Mg-doping induces hillock-type features on the surface of the film; as the Mg level is increased these hillocks develop into densely packed hexagonal features. The approximate height of these surface features has been estimated from the AFM measurements and ranges from 40 nm in the lightly doped films to 100 nm in sample E and 300 nm in sample F.

The results of room temperature Hall effect measurements are shown in figure 2.13. The hole concentration is observed to increase with Mg-doping level, however the mobility drops so rapidly that the material resistivity remains fairly constant at approximately 1 Ω cm. (In the most heavily-doped film the hole
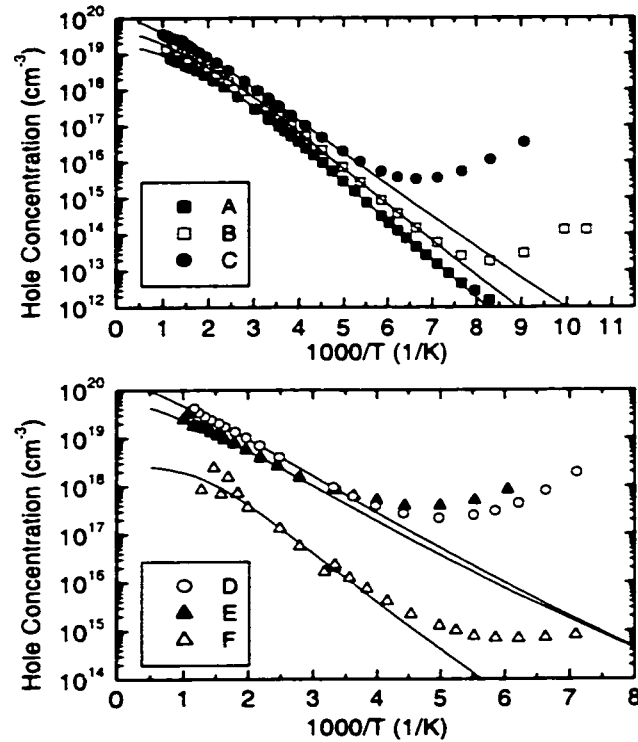

Figure 2.14 Hole concentration measured as a function of temperature on Mg-doped GaN samples. For clarity of presentation the data have been divided between two separate plots; note that the scale differs on the two plots. The solid lines represent fits to equation (2.8).

38

concentration has dropped again, and the mobility has recovered slightly.) This inability to reduce the material resistivity through heavier doping is a significant problem for device work. Temperature-dependent Hall effect measurements were performed at Wright-Patterson Air Force Base in order to investigate the origin of the effect.

Figure 2.14 shows the results of the temperature-dependent Hall effect measurements: the measured hole concentration is plotted as a function of the inverse temperature for each of the samples. An activation energy dependence is clearly evident in the high-temperature regime for all of the samples. In all but the most lightly-doped sample the measured hole concentration increases again at low temperature, indicating the onset of hopping or impurity-band conduction. In the most heavily doped samples this impurity conduction is clearly an important component of the total room temperature conductivity.

The acceptor activation energy (ΔE_A), acceptor concentration (N_A), and compensating donor concentration (N_D) were extracted by fitting the high-temperature data to equation (2.8), with the assumed values $g = 4$ and $m^*_h = 2.2$ m_0. Using this value of m^*_h provides a good agreement between the extracted

| Sample | Growth | Cp₂Mg flow | | ΔE_A (meV) | N_A (cm⁻³) | N_D (cm⁻³) |
		sccm	nmol/min			
A	990206PB	15	24.4	190	$1.8{\times}10^{19}$	$1.1{\times}10^{18}$
B	990206PA	26	42.3	174	$4.6{\times}10^{19}$	$3.0{\times}10^{18}$
C	990205PD	47	76.5	152	$1.4{\times}10^{20}$	$1.2{\times}10^{19}$
D	980901PA	83	135	118	$2.2{\times}10^{20}$	$4.1{\times}10^{19}$
E	990205PC	140	228	112	$8.6{\times}10^{19}$	$2.7{\times}10^{19}$
F	980901PE	263	428	165	$7.6{\times}10^{18}$	$5.0{\times}10^{18}$

Table 2.2 Summary of growth conditions and of fitting results from temperature-dependent Hall effect measurements.

acceptor density and the SIMS measurements of Mg concentration; using smaller values of m^*_h causes the calculated acceptor density to be considerably higher than the Mg concentration.

We note that the model used to fit the data is quite simple; equation (2.2) assumes a single acceptor level, and equation (2.3) assumes a parabolic valence band. The formation of a broad impurity band, or of valence band-tail states, is therefore beyond the scope of this model. If these effects play an important role in the heavily-doped samples, then the fitting procedure employed may provide results that are somewhat inaccurate.

Figure 2.15 and table 2.2 summarize the parameters which provide the best fit between equation (2.8) and the temperature-dependent Hall
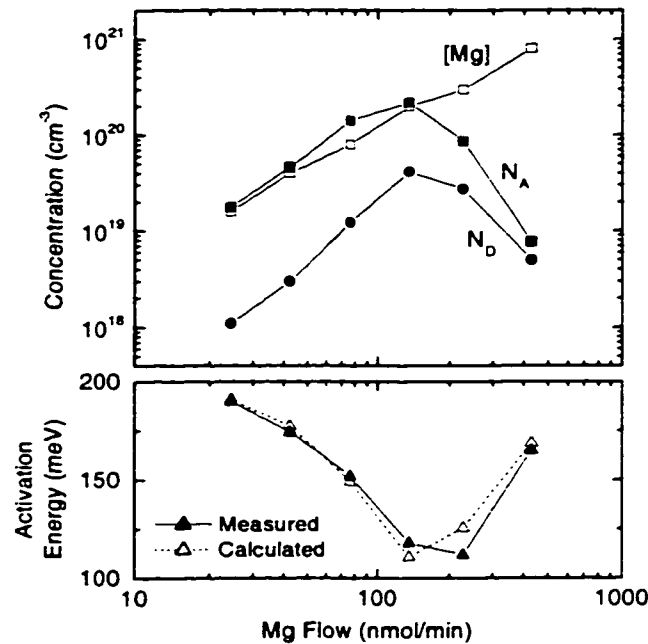
Figure 2.15 Concentration data extracted from the Hall effect and SIMS measurements are presented in the top plot. In the lower plot, the solid triangles represent the measured activation energy and the open triangles represent that predicted by equation (2.17).

measurements. The measured activation energy for the Mg acceptor decreases as the doping is increased, going from 190 meV in sample A to 112 meV in sample E. The material quality begins to degrade before the Mott transition can be reached, and the activation energy rises again in the severely over-doped sample.

The extracted values of N_A and N_D are also plotted in figure 2.15. While the activation energy can be extracted quite accurately from the least-squares fit to equation (2.8), there is considerable uncertainty in the acceptor and compensating donor concentrations. This is due not only to the assumption of the hole mass, but also to the nature of the data fit (especially in the more heavily doped samples where there is little indication of saturation in the hole concentration measured at high temperature).

Nonetheless, the extracted concentrations match closely with expected values. The acceptor concentration rises as the dopant density is increased, in good agreement with the Mg concentration as measured by SIMS. The highest acceptor concentration (around 2×10^{20} cm^{-3}) was obtained in sample D (which corresponds to the "standard" growth conditions when the change in bubbler temperature is taken into account). When the Mg concentration is increased beyond this point the extracted acceptor concentration is actually reduced, which may indicate that much of the Mg is not incorporating in the desired substitutional site. We also note that the calculated compensation level ($r_{comp} = N_D / N_A$) is observed to rise dramatically as the doping level is increased.

The measured decrease in acceptor activation energy at high doping levels may explain the variation in published results for the depth of the Mg acceptor. This phenomenon is well known from conventional semiconductors,[72-75] and may have various causes including: the formation of a broad Mg acceptor band extending toward the valence band edge, the creation of valence band-tail states extending into the forbidden gap, screening of the acceptor potential by free

carriers, and binding energy reduction through a Coulomb interaction between valence-band holes and ionized acceptors.

Götz et al.[51] have suggested an important role for the last of these effects in Mg-doped GaN. In this case the acceptor activation energy may be written as:

$$\Delta E_A \left(N_A^-\right) = \Delta E_{A,0} - f\frac{q^2}{4\pi\varepsilon}\left(N_A^-\right)^{1/3},$$ (2.17)

where $\Delta E_{A,0}$ is the inherent acceptor binding energy observed at very low doping concentrations, $\left(N_A^-\right)^{-(1/3)}$ is the average distance between ionized acceptors, q is the electronic charge, ε is the dielectric constant (assumed to be 9.5 ε_0) and f is a geometric factor of value $\Gamma(2/3)(4\pi/3)^{1/3}$.[51] We note that this formulation neglects the repulsive potential of the ionized compensating donors, an assumption which is somewhat justified because the free holes are likely to concentrate around the ionized acceptors and avoid the donors.[75]

Götz suggests that the acceptor energy in equation (2.8) be re-evaluated at each temperature depending on the ionized acceptor concentration. However, in this case we are justified in using a simpler approach in which a single temperature-independent activation energy is used for each sample. This is because the ionized acceptor concentration is determined mainly by the number of compensating donors, not the number of free holes, across the great majority of the temperature range used for data fitting. We therefore use equation (2.8) to fit the Hall effect data and then compare the measured acceptor energy to that predicted by equation (2.17) using $N_A^- \approx N_D$. Assuming an inherent binding energy of $E_{A,0} = 220$ meV, a very close agreement is obtained between the measured activation energy and that predicted by equation (2.17), as shown in figure 2.15. (In fact, the fit is surprisingly good considering the uncertainty in the values of N_D.) We note that this inherent activation energy is in reasonable agreement with the acceptor level measured by photoluminescence.[47,71]

42

Figure 2.16 presents the hole mobility measured as a function of temperature. The highest mobility recorded is 62 cm²/Vs for the lightly doped sample at T = 146 K. As the doping level is increased the peak mobility begins to drop rapidly due to the high concentration of ionized species resulting from the higher doping level and compensation ratio. In the most heavily doped sample the hole mobility is observed to increase again slightly, most likely a consequence of the reduced ionized dopant density. In most samples the measured mobility degrades slowly at high temperature but exhibits a precipitous drop at low temperature. This is due to the dominance at low temperature of the hopping conduction path.

The true mobility of the valence band (μ_{VB}) may be extracted by separating the valence band conductivity (σ_{VB}) from the impurity conductivity (σ_I). Because the hopping conduction results in a Hall coefficient (R_I) close to zero, the measured Hall coefficient is given by
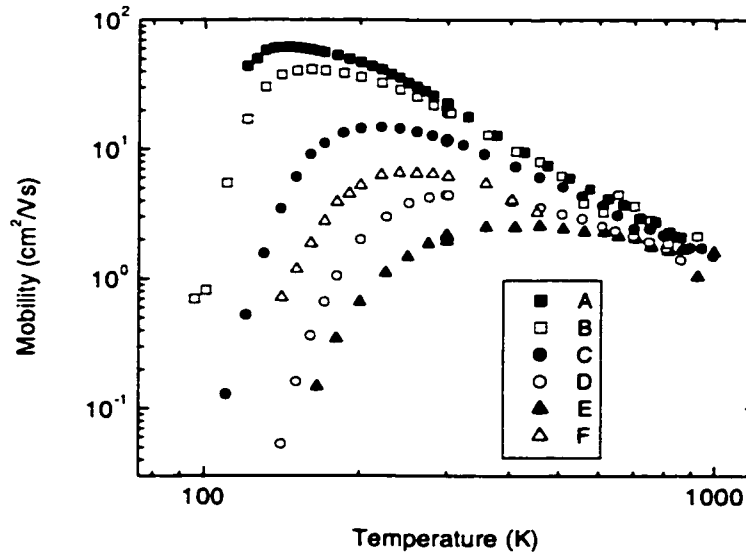

Figure 2.16 Mobility measured as a function of temperature.

43

$$R = \frac{R_{VB}\sigma_{VB}^2}{\left(\sigma_{VB}+\sigma_I\right)^2},$$ (2.18)

where R_{VB} represents the Hall coefficient of the valence band transport.[76] This quantity can be calculated from p_{VB}, which is the hole concentration in the valence band as given by equation (2.8) fitted to the experimental data. The true valence band mobility μ_{VB} is then extracted as

$$\mu_{VB} = \mu\sqrt{\frac{p}{p_{VB}}},$$ (2.19)

where p and μ represent the measured values of the hole concentration and mobility, respectively. The hopping conductivity is simply

$$\sigma_I = q(p\mu - p_{VB}\mu_{VB}).$$ (2.20)

The valence band mobility μ_{VB} for samples B through E has been calculated and is shown in figure 2.17. With the impurity conduction removed, the drop in low-temperature valence band mobility is seen to be much less steep. The factors determining the exact temperature dependence of the valence band mobility are not fully understood at this point—a more complete analysis of the mobility measurements is needed. Figure 2.17 also presents the calculated value of the hopping conductivity. As expected, the conductivity of this current path is strongly dependent on the doping concentration, increasing by several orders of magnitude over the sample range.

In conclusion, a number of heavy doping effects are observed in Mg-doped GaN, including increased impurity conduction and greater compensation. The increased compensation appears to drive other effects such as lower hole mobility values and a pronounced reduction in acceptor activation energy via a Coulomb interaction between holes and ionized acceptors. This reduction in binding energy partially offsets the effects of increased compensation, so that the

44

hole concentration does not fall precipitously as predicted in figure 2.3. The measured acceptor concentration increases with Mg concentration up to the optimum doping level of 2×10^{20} cm^{-3}, but the doping efficiency drops beyond this point and at very high doping levels severe morphological changes are observed.
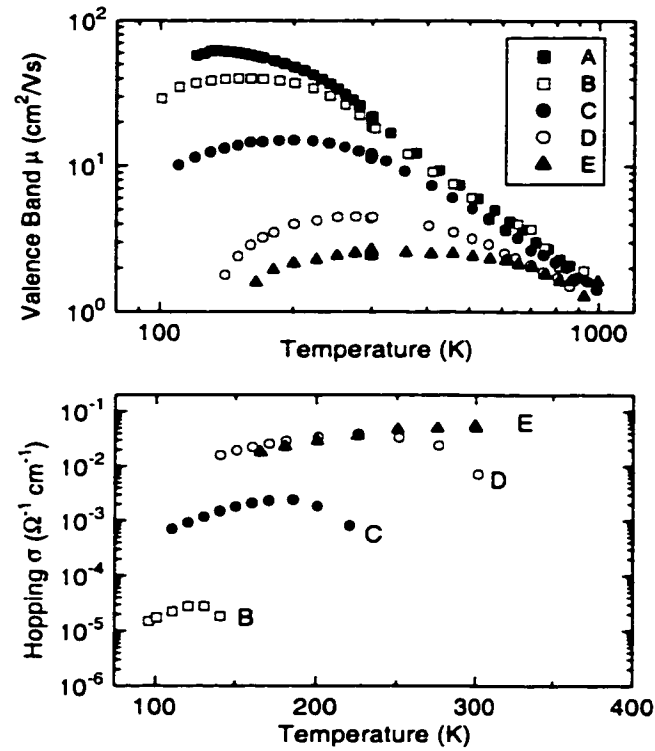

Figure 2.17 Valence band mobility and hopping conductivity as a function of temperature for the various samples under study.

2.7 Effects of growth rate, V/III ratio, and reactor pressure

The growth parameters which were varied in this study include reactor pressure, growth rate, and the molar flow ratio of NH_3 to TMGa + Cp_2Mg (V/III ratio)—all are parameters that have received scant attention in the literature. Growths were performed at both atmospheric pressure and at a reduced pressure of 76 torr, at growth rates ranging from 0.5 μm/hr to 2 μm/hr, and V/III ratios between 6,900 and 27,700. The molar flow ratio of TMGa to Cp_2Mg was 142; this was kept constant so that the nominal doping concentration is identical for all the growths. The total flow through the reactor was kept constant in all the runs and is approximately 11 standard liters per minute (slpm). The Mg bubbler temperature was 45.2°C, and the growth temperature was 1000°C.

The ten samples grown for this study are divided into three series; the growth conditions and electrical data are summarized in table 2.3. In series 1 and series 2 the GaN growth rate and the V/III ratio were varied simultaneously by changing the TMGa flow (and also the Cp_2Mg flow) while keeping the NH_3 flow constant at 6 slpm. Series 1 was grown at atmospheric pressure and series 2 was grown at 76 torr. In these growths, the TMGa flow was varied from 9.6 μmol/min to 38.4 μmol/min corresponding to a growth rate variation from 0.5 to 2.0 μm/hr (the growth rate is independent of pressure). Series 3 was grown at 76 torr and the growth rate was kept constant at 0.5 μm/hr; in this group the V/III ratio was varied by reducing the NH_3 flow (H_2 was added in order to keep the total flow constant). Two of the growths were repeated in order to check the consistency of the results.

As discussed in section 2.5, SIMS measurements have shown that the Mg concentration is independent of growth rate, but slightly higher at 76 torr than at atmospheric pressure. SIMS measurements on the samples in series 3 indicated that the Mg concentration was also unchanged as a result of varying the NH3

flow. Figure 2.18 shows the SIMS profile of a sample with a stack of layers grown under the conditions of series 1 and 2. The increased carbon concentration in layers grown at high growth rates and low pressure, which is evident in figure 2.18, is also observed in undoped GaN films. These carbon atoms are believed to occupy N sites and therefore behave as deep acceptors.[77]

The electrical characteristics of the samples have been investigated through room temperature Hall effect measurements; the results are summarized in table 3.3. The samples grown at atmospheric pressure show very little variation; the average hole concentration in these samples is 7.4×10^{17} cm^{-3} and the mobility varies between 7.4 and 10.7 cm^2/Vs. At 76 torr, however, the electrical properties demonstrate a dramatic dependence on the growth conditions. By reducing the growth rate and increasing the V/III ratio, the resistivity of the film is

Series	Sample	Pressure (torr)	TMGa (μmol/min)	NH$_3$ (slpm)	V / III Ratio	p (cm^{-3})	μ (cm^2/Vs)
1	980105PA	760	38.4	6.0	6,900	8.2×10^{17}	10.2
	970130PD	760	38.4	6.0	6,900	7.3×10^{17}	8.0
	980426PA	760	19.3	6.0	13,800	6.9×10^{17}	10.7
	970818PC	760	9.6	6.0	27,700	7.2×10^{17}	7.4
2	970714PD	76	38.4	6.0	6,900	1.1×10^{17}	6.4
	970814PC	76	19.3	6.0	13,800	9.4×10^{16}	12.1
	970818PA	76	9.6	6.0	27,700	2.5×10^{17}	19.6
3	971114PC	76	9.6	1.5	6,900	6.1×10^{16}	9.7
	971114PB	76	9.6	3.0	13,800	1.1×10^{17}	14.5
	971114PA	76	9.6	6.0	27,700	2.7×10^{17}	19.2

Table 2.3 Growth parameters and electrical data for the samples discussed in section 2.7. The samples have been divided into three series.

reduced by almost an order of magnitude. This data for the first two growth series is summarized in figure 2.19.

Figure 2.20 shows the hole concentration and mobility for low-pressure-grown films as a function of the V/III ratio. The data are quite similar for the two series, indicating that it is the V/III ratio and not simply the growth rate that is controlling the electrical characteristics. We note that both the hole concentration and the mobility increase with increasing V/III ratio, combining to give the large reduction in resistivity seen in figure 2.19. The simultaneous increase in hole mobility and concentration suggests that the improved electrical characteristics are due to a reduction in compensation.

In section 2.6, we found that the high compensation ratio in heavily-doped films was responsible for the low hole mobility and concentration obtained at room temperature. In the present section, we have found that the degree of compensation can be adjusted, at least partially, through varying the growth conditions. These growth results seem to support the model of a nitrogen
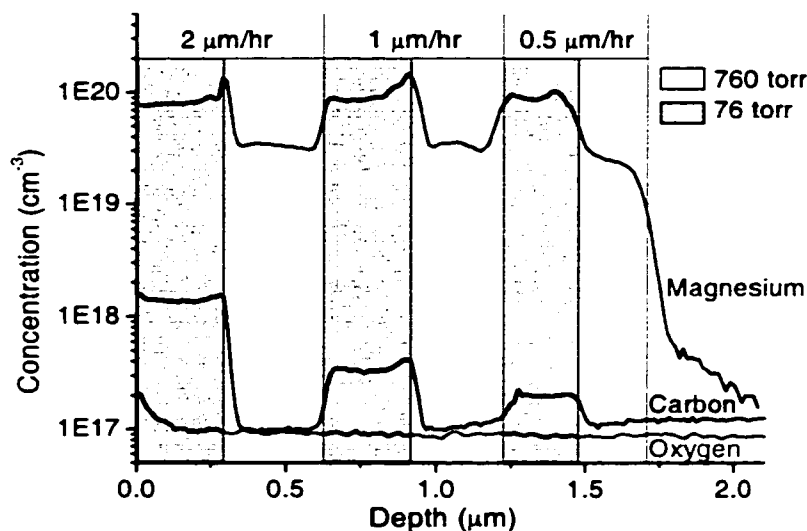

Figure 2.18 SIMS measurements on a Mg-doped GaN sample with layers grown under various different conditions.

vacancy-related donor as the compensating species, as suggested by other researchers.[21,45-47]

During growth at atmospheric pressure the absolute NH_3 over-pressure is quite high (approximately 0.6 atm) so that nitrogen vacancy formation should be minimized. Under these conditions, varying the V/III ratio had no impact on the electrical properties of the Mg-doped samples within the investigated range. At a reduced pressure of 76 torr, however, the NH_3 over-pressure is ten times lower and in this regime it is plausible that the V/III ratio during growth has a considerable impact on the nitrogen vacancy concentration. According to this model, growth at low pressure and low V/III ratio encourages the formation of compensating nitrogen vacancies and degrades the electrical characteristics of the film.

Another factor that may play a role in the increased sensitivity of the low-pressure grown films to V/III ratio is that these layers contain a higher Mg concentration, as determined by SIMS. From the results of section 2.6, it seems
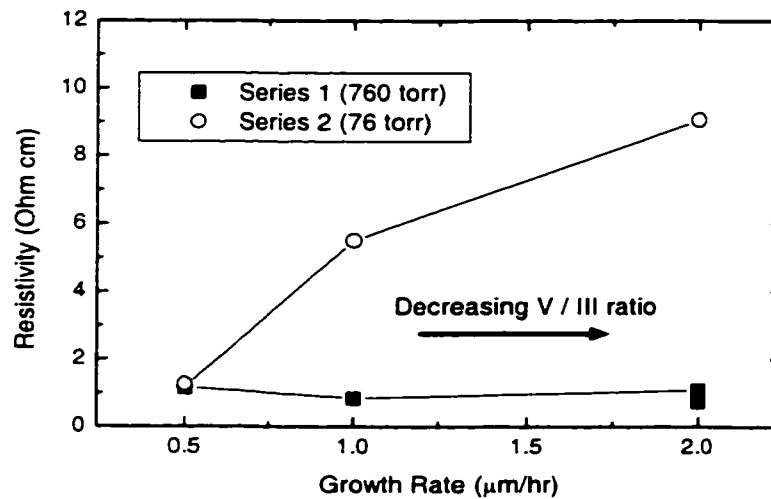

Figure 2.19 Resistivity as a function of growth rate for the samples in series 1 and series 2.

that such heavily-doped films are more susceptible to compensation. Finally, we note that even the best low-pressure-grown samples display a lower hole concentration and higher mobility than do the layers grown at atmospheric pressure, despite containing a higher concentration of Mg. The high mobility values suggest that this discrepancy is due not to compensation but rather the incorporation of Mg atoms on non-electrically-active sites. This phenomenon, too, may be related to the higher Mg concentration obtained under these conditions.
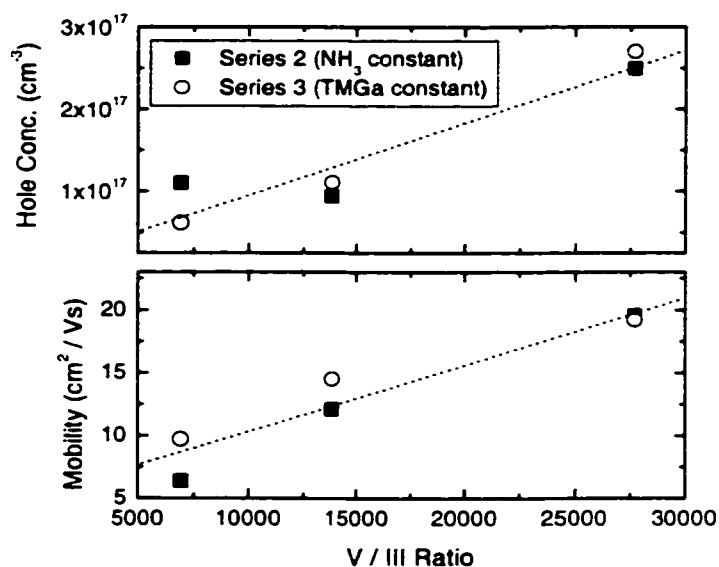

Figure 2.20 Electrical characteristics of samples grown at low pressure (76 torr). The dotted lines are eye-guides.

2.8 Effect of growth temperature

Figure 2.21 displays the results of Hall effect measurements performed on samples grown at various growth temperatures between 900°C and 1060°C (otherwise the samples were grown under the "standard" growth conditions). The variations in p and μ are fairly small over this temperature range, but the highest hole concentration was measured at a growth temperature of 1000°C. The drop in hole concentration at lower growth temperatures could be due to increased compensation under these conditions. This hypothesis is consistent with the model of nitrogen-vacancy-related donor states described in the previous section, since the NH_3 decomposition efficiency is reduced as the temperature is lowered. Above 1000°C, the measured hole concentration drops and the mobility increases,
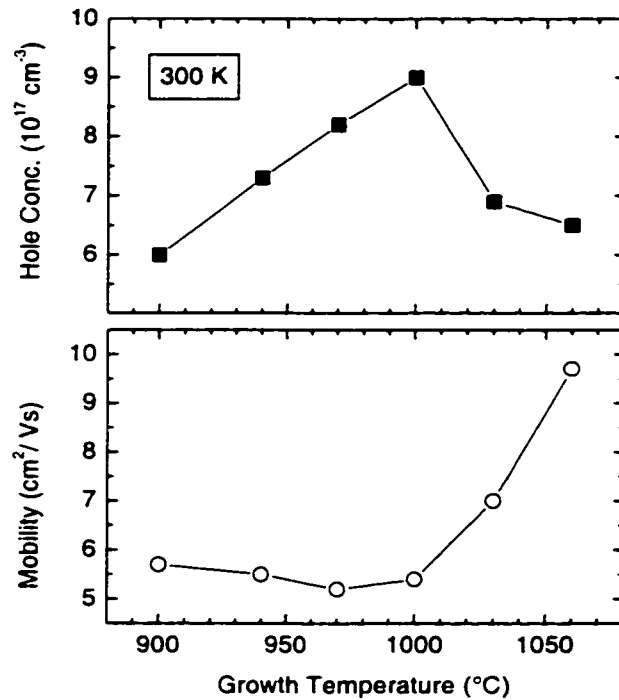
Figure 2.21 Hall effect measurements on Mg-doped GaN films grown at varying temperatures.

51

suggesting a reduction in ionized acceptor concentration. The Mg density is known from the SIMS results to be temperature-independent, leaving two possible explanations for the high-temperature results: an increase in the acceptor binding energy and/or a greater degree of Mg incorporation in non-electrically-active sites.

In figure 2.22, measurements of the specific contact resistance of Pd/Au contacts to these samples are presented. (Details of the TLM measurements are discussed in chapter 3.) There is a clear trend towards a reduced contact resistance in the high-temperature grown samples. This result also supports the model of reduced compensation at higher growth temperatures, since a higher net acceptor concentration near the surface would lead to a lower contact resistance. The observation may also prove useful in reducing the contact resistance in various device structures.
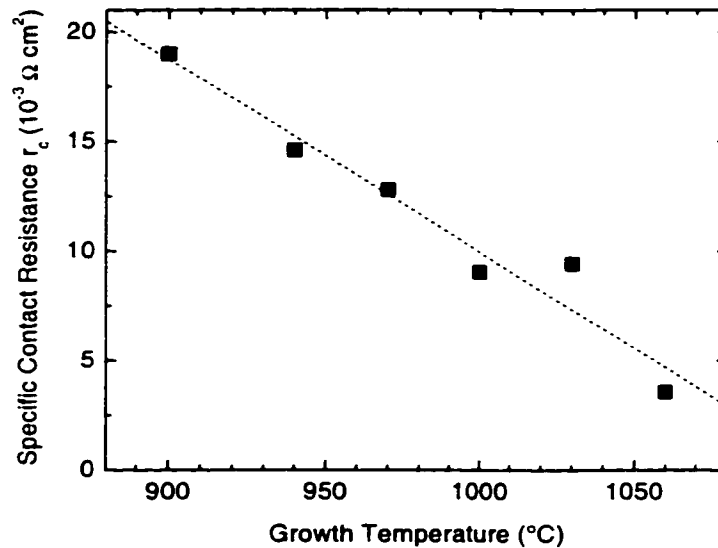

Figure 2.22 Specific contact resistance of Pd/Au contacts on Mg-doped GaN, as a function of growth temperature. The dotted line is an eye guide.

A further investigation of high-temperature growth was performed by growing a series of samples at 1065°C with different Cp_2Mg flows. Like those in the Mg-flow study described in section 2.6, these samples were grown with the Mg bubbler temperature reduced to 25.2°C (aside from the growth temperature, these samples reproduce the conditions of samples B to E of section 2.6). The Hall results for these samples are shown in figure 2.23. Surprisingly, the hole concentration is basically constant at approximately 3×10^{17} cm^{-3} (a somewhat lower value than that obtained in the previous films). The mobility, however, does depend on the doping density, dropping from 22 to 10 cm^2/Vs as the concentration is increased.

The constant hole concentration could result from Mg incorporation on non-electrically-active sites for densities beyond some maximum acceptor concentration. In that case, however, one would expect the mobility to remain
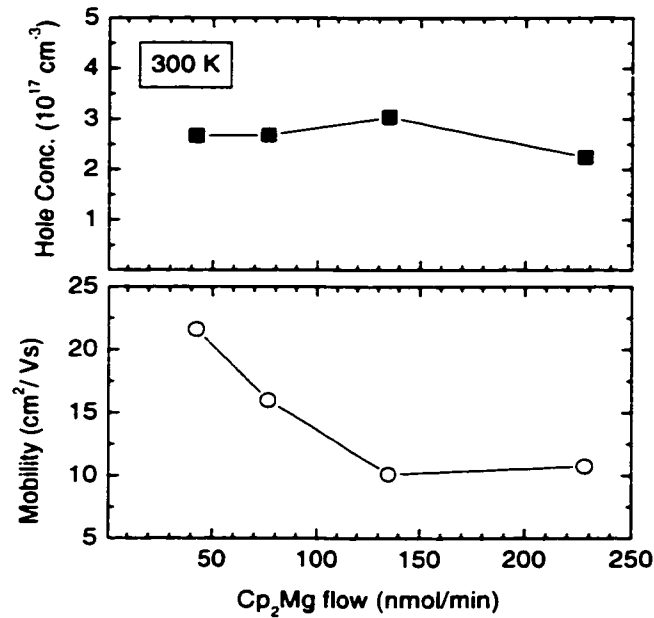

Figure 2.23 Hall effect measurements on Mg-doped GaN samples grown with various Cp_2Mg flows at 1065 °C.

fairly constant as well, since the neutral impurity scattering should be a fairly small effect. Another possible explanation is that the constant hole concentration is a result of a constant compensation ratio, as described in case 2 of section 2.2. If this is indeed the case, however, it is rather surprising that the binding energy reduction that was observed in the samples grown at 1000°C is absent in this case.

These results suggest that using a higher growth temperature than that employed in the "standard" growth conditions may be beneficial in reducing the degree of compensation. However, it is difficult to draw firm conclusions from these simple room-temperature measurements; a detailed study of temperature-dependent Hall effect measurements is needed to understand the electrical properties of these samples.

2.9 Effect of gas ambient

In 1998, Sugiura, et al. reported on the growth of Mg-doped GaN in a N_2 ambient, finding that as-grown films exhibited p-type conductivity without the need for an activation step.[14] These results were confirmed in our MOCVD system, as shown in figure 2.24. Because it was impossible to eliminate H_2 completely from the growth environment (it is the carrier gas which is used in the metalorganic source bubblers), the comparison is between "N_2 rich" growth conditions (4.5 lpm N_2, 0.25 lpm H_2, 6 lpm NH_3) and the standard "H_2 rich" conditions (0.25 lpm N_2, 4.5 lpm H_2, 6 lpm NH_3). After activation, the two films exhibited identical conductivity values. However, the as-grown conductivity of the "H_2 rich" film was immeasurably small, while that of the "N_2 rich" film was quite high—approximately half of the activated value. The N_2 rich growth is a useful technique allowing quick evaluation of device structures such as LEDs without the need for activation processing. For maximum conductivity, however,

the activation step is still important because some H-passivation remains (due to either the remaining H_2 or hydrogen from NH_3).
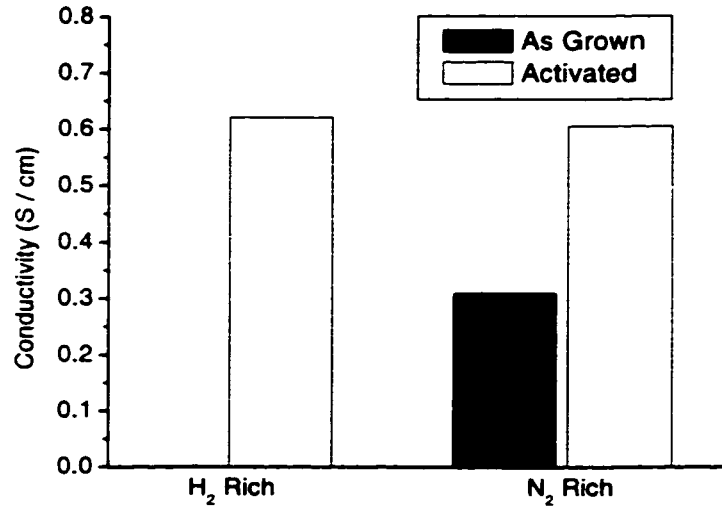

Figure 2.24 Conductivity of Mg-doped GaN films grown in H_2 rich and N_2 rich ambients.

2.10 Mg-doped AlGaN

P-type doping of AlGaN is a crucial technology for the achievement of lasers in the nitride materials system. The ability to *p*-type dope alloys will also be useful for many other devices (for example, graded base HBTs). There are a few reports in the literature discussing the characteristics of Mg-doped $Al_xGa_{1-x}N$,[2,78,79] in which *p*-type conductivity has been obtained for x < 0.3. The acceptor energy level is generally found to move slightly deeper as the Al composition is increased, but does not change as much as the effective-mass theory predicts. Similar results have been obtained in our work on Mg-doped AlGaN.

Figure 2.25 shows the results of room temperature Hall effect measurements on Mg-doped (Al)GaN samples for three different compositions. These samples were all grown at a reduced pressure of 300 torr—this is the highest pressure at which the pre-reaction between NH_3 and TMAl is effectively suppressed in this reactor. Both the measured hole concentration and mobility drop as the aluminum mole fraction is increased—a combination which hints that compensation, not a deeper acceptor level, is the origin of the reduced hole concentration.

The acceptor binding energy in these layers has been estimated from temperature-dependent resistivity measurements, as shown in figure 2.26. An activation energy is extracted by neglecting the temperature-dependence of both the mobility and the valence band density of states. These results are in agreement with the published reports and suggest very little variation in Mg acceptor binding energy up to an aluminum composition of 18%.
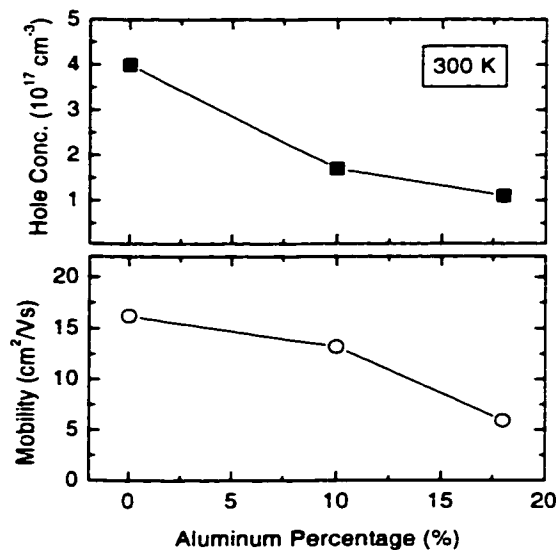

Figure 2.25 Room temperature Hall effect measurements on Mg-doped (Al)GaN films.
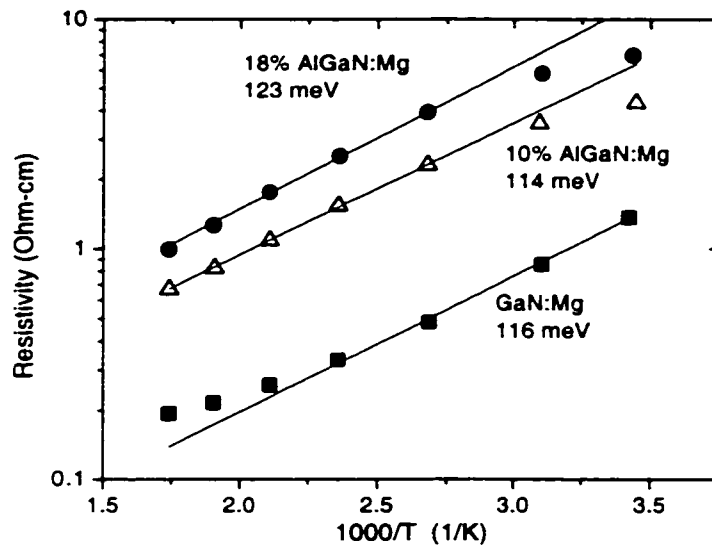
Figure 2.26 Arrhenius plot of temperature-dependent resistivity measurements on Mg-doped (Al)GaN samples. The solid lines represent fitting to an activation energy dependence, as indicated.

2.11 Memory effect

Mg is rarely used in MOCVD growth of conventional III-V materials because of the strong "memory effect" when doping with this source.[80,81] The memory effect introduces doping delays, prevents sharp interfaces, and can lead to a non-linear dependence of incorporated Mg on the source flow. The origin of the memory effect is the tendency of the Mg source molecules to stick to the plumbing and reactor walls, and may also involve a surface-riding effect.[82] The memory effect is a major problem for p-type doping of GaN by MOCVD. This effect is expected to be strongly dependent on reactor geometry, and may be considerably reduced in reactors in which wall effects do not play a significant role.

57

Figure 2.27 shows SIMS measurements of the Mg and Si dopant profiles in an *n-p-n* (Si-Mg-Si) structure grown in our MOCVD reactor. The layer structure was grown on top of an undoped GaN template that had been prepared some time earlier. The original template was grown in a clean reactor, so the Mg concentration in this layer is below the SIMS detection limit. The background Mg concentration is much higher in the re-grown Si-doped layers, however, due to residual Mg contamination in the reactor that was used to grow the *n-p-n* structure.

The Si profile is quite sharp, and the concentration measured is constant in the doped layers. In contrast, the Mg-doped layer does not show a sharp, square profile. The first interface, when the Mg is turned on, is fairly abrupt, but the Mg turn-off is extremely slow. This asymmetry suggests that surface-riding may play a significant role in the memory effect under these growth conditions. Solid-state dopant diffusion is not believed to play a role in the Mg profiles, as
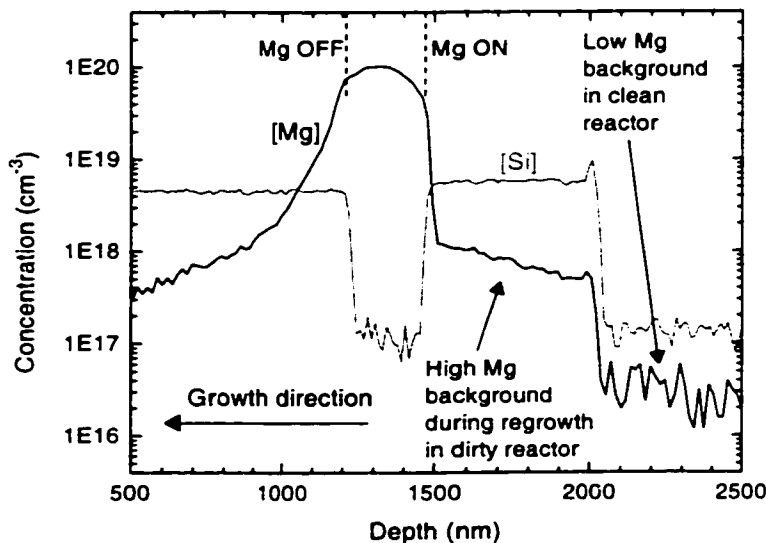

Figure 2.27 SIMS profile of a GaN *n-p-n* structure grown by MOCVD.

numerous studies have shown that this effect is minimal even at temperatures much higher than those employed in MOCVD growth.[83-85]

The relatively sharp nature of the Mg turn-on has no doubt been a major factor in the success of the optoelectronic devices grown in this reactor. For bipolar transistors, however, both interfaces are of great importance. In these devices, the memory effect severely degrades performance by causing uncontrolled base widening. As shown in figure 2.27, the base width can easily be 200 nm thicker than designed as a result of this effect. We have investigated various approaches to circumvent this problem during bipolar transistor growths. Successful devices have been fabricated by growing the emitter at low temperature (800°C); at this temperature it is possible to increase the Si-doping level considerably, and the cooler reactor walls may somewhat reduce the magnitude of the memory effect. Other approaches which have been tried (with varying degrees of success) include: employing a growth interrupt after the base
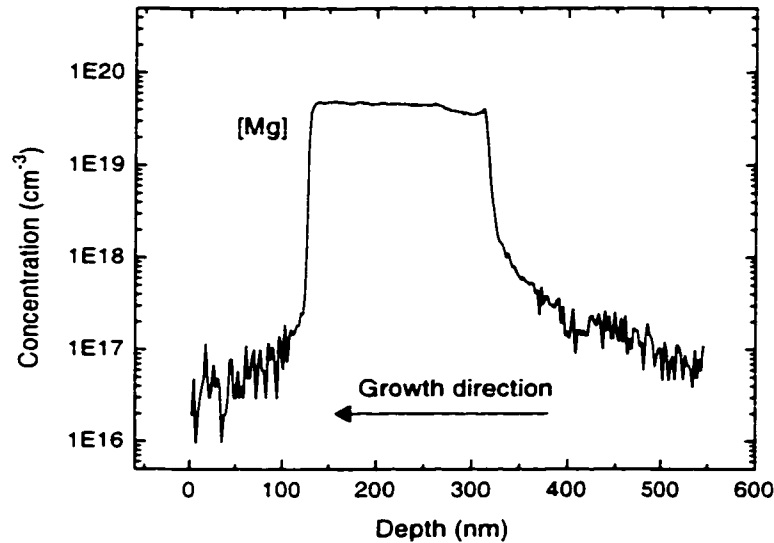

Figure 2.28 SIMS profile of a GaN *n-p-n* structure grown by MBE.

layer in order to pump and backfill the reactor repeatedly, removing the sample after the growth of the base layer in order to bake out the reactor, and removing the sample and then selectively re-growing the emitter in patterned openings. (Instead of using SIMS, electrical tests were generally used to determine the conductivity type in the surface layer for these growth experiments.) However, the best solution may be to change growth techniques completely. Figure 2.28 shows SIMS measurements of the Mg-doping profile in an n-p-n sample grown at UCSB by plasma-assisted MBE (the growth was performed by Yulia Smorchkova). A very sharp dopant profile is clearly evident.

2.12 References

1   S. Nakamura, M. Senoh, and T. Mukai, "Highly p-typed Mg-doped GaN films grown with GaN buffer layers." *Jpn. J. Appl. Phys.* **30**, L1708-11 (1991).

2   T. Tanaka, A. Watanabe, H. Amano, Y. Kobayashi, I. Akasaki, S. Yamazaki, and M. Koike, "p-type conduction in Mg-doped GaN and $Al_{0.08}Ga_{0.92}N$ grown by metalorganic vapor phase epitaxy." *Appl. Phys. Lett.* **65**, 593-594 (1994).

3   C. Yuan, T. Salagaj, A. Gurary, A. G. Thompson, W. Kroll, R. A. Stall, C. Y. Hwang, M. Schurman, Y. Li, W. E. Mayo, Y. Lu, S. Krishnankutty, I. K. Shmagin, R. M. Kolbas, and S. J. Pearton, "Investigation of n- and p-type doping of GaN during epitaxial growth in a mass production scale multiwafer-rotating-disk reactor." *J. Vac. Sci. Technol. B* **13**, 2075-80 (1995).

4   H. Lu and I. Bhat, "Magnesium doping of GaN by metalorganic chemical vapor deposition." *Mat. Res. Soc. Symp. Proc.* **395**, 497-502 (1996).

5   H. Nakayama, P. Hacke, M. R. H. Khan, T. Detchprohm, T. D. Kazumasa, K. Hiramatsu, and N. Sawaki, "Electrical transport properties of p-GaN." *Jpn. J. Appl. Phys.* **35**, L282-4 (1996).

6   A. Cros, R. Dimitrov, H. Angerer, O. Ambacher, M. Stutzmann, S. Christiansen, M. Albrecht, and H. P. Strunk, "Influence of magnesium doping on the structural properties of GaN layers." *J. Cryst. Growth* **181**, 197-203 (1997).

7   C. J. Eiting, P. A. Grudowski, J. Park, D. J. H. Lambert, B. S. Shelton, and R. D. Dupuis, "Characteristics of Mg-doped GaN grown by metallorganic chemical vapor deposition." *J. Electrochem. Soc.* **144**, L219-21 (1997).

8   C. J. Eiting, P. A. Grudowski, and R. D. Dupuis, "Growth of low resistivity p-type GaN by metal organic chemical vapour deposition." *Electron. Lett.* **33**, 1987-9 (1997).

9   Y. Ohuchi, K. Tadatomo, H. Nakayama, N. Kaneda, T. Detchprohm, K. Hiramatsu, and N. Sawaki, "New dopant precursors for n-type and p-type GaN." *J. Cryst. Growth* **170**, 325-8 (1997).

10   N. Akutsu, H. Tokunaga, I. Waki, A. Yamaguchi, and K. Matsumoto, "Epitaxial growth and properties of Mg-doped GaN film produced by atmospheric MOCVD system with three layered laminar flow gas injection." *Mat. Res. Soc. Symp. Proc.* **482**, 113-18 (1998).

11   L. Eckey, U. Von Gfug, J. Holst, A. Hoffmann, B. Schineller, K. Heime, M. Heuken, O. Schoen, and R. Beccard, "Compensation effects in Mg-doped GaN epilayers." *J. Cryst. Growth* **189-190**, 523-7 (1998).

12   C. J. Eiting, P. A. Grudowski, and R. D. Dupuis, "P- and N-type doping of GaN and AlGaN epitaxial layers grown by metalorganic chemical vapor deposition." *J. Electron. Mater.* **27**, 206-9 (1998).

13   C. R. Lee, J. Y. Leem, S. K. Noh, S. E. Park, J. I. Lee, C. S. Kim, S. J. Son, and K. Y. Leem, "Characteristics of Mg-doped GaN epilayers grown with the variation of Mg incorporation." *J. Cryst. Growth* **193**, 300-4 (1998).

14   L. Sugiura, M. Suzuki, J. Nishio, K. Itaya, Y. Kokubun, and M. Ishikawa, "Characteristics of Mg-Doped GaN and AlGaN grown by H_2-ambient and N_2-ambient metalorganic chemical vapor deposition." *Jpn. J. Appl. Phys.* **37**, 3878-81 (1998).

15   H. Tokunaga, I. Waki, A. Yamaguchi, N. Akutsu, and K. Matsumoto, "Growth condition dependence of Mg-doped GaN film grown by horizontal atmospheric MOCVD system with three layered laminar flow gas injection." *J. Cryst. Growth* **189-190**, 519-22 (1998).

16   S. Haffouz, B. Beaumont, M. Leroux, M. Laugt, P. Lorenzini, P. Gibart, and L. G. Hubert-Pfalzgraf, "p-doping of GaN by MOVPE." *MRS Internet J. Nitride Semicond. Res.* **2**, 37 (1997).

17   Z. Yang, L. K. Li, and W. I. Wang, "P-type Mg-doped GaN grown by molecular beam epitaxy using ammonia as the nitrogen source." *Mat. Res. Soc. Symp. Proc.* **395**, 169-73 (1996).

18   W. Kim, A. Salvador, A. E. Botchkarev, O. Aktas, S. N. Mohammad, and H. Morcoc, "Mg-doped p-type GaN grown by reactive molecular beam epitaxy." *Appl. Phys. Lett.* **69**, 559-61 (1996).

19   R. F. Davis, T. W. Weeks, Jr., M. D. Bremser, S. Tanaka, R. S. Kern, Z. Sitar, K. S. Ailey, W. G. Perry, and C. Wang, "Growth of AlN and GaN thin films via OMVPE and gas source MBE and their characterization." *Solid-St. Electron.* **41**, 129-34 (1997).

20   R. F. Davis, M. J. Paisley, Z. Sitar, D. J. Kester, K. S. Ailey, K. Linthicum, L. B. Rowland, S. Tanaka, and R. S. Kern, "Gas-source molecular beam epitaxy of III-V nitrides." *J. Cryst. Growth* **178**, 87-101 (1997).

21   S. N. Mohammad, A. E. Botchkarev, A. Salvador, W. Kim, O. Aktas, and H. Morkoc, "Proposed explanation of the anomalous doping characteristics of III-V nitrides." *Philosoph. Mag. B* **76**, 131-143 (1997).

22 N. Grandjean, J. Haassies, and M. Leroux, "Si and Mg doped GaN layers grown by gas source molecular beam epitaxy using ammonia." *Mat. Res. Soc. Symp. Proc.* **482,** 211-16 (1998).

23 J. M. Myoung, K. H. Shim, C. Kim, O. Gluschenkov, K. Kim, S. Kim, D. A. Turnbull, and S. G. Bishop, "Optical characteristics of p-type GaN films grown by plasma-assisted molecular beam epitaxy." *Appl. Phys. Lett.* **69,** 2722-4 (1996).

24 R. P. Vaudo, I. D. Goepfert, T. D. Moustakas, D. M. Beyea, T. J. Fray, and K. Meehan, "Characteristics of light-emitting diodes based on GaN p-n junctions grown by plasma-assisted molecular beam epitaxy." *J. Appl. Phys.* **79,** 2779-83 (1996).

25 S. Guha, N. A. Bojarczuk, and F. Cardone, "Mg in GaN: incorporation of a volatile species at high temperatures during molecular beam epitaxy." *Appl. Phys. Lett.* **71,** 1685-7 (1997).

26 J. M. Myoung, K. H. Shim, O. Gluschenkov, C. Kim, K. Kim, S. Kim, and S. G. Bishop, "Effect of growth temperature on the properties of p-type GaN grown by plasma-assisted molecular beam epitaxy." *J. Cryst. Growth* **182,** 241-6 (1997).

27 M. C. Yoo, M. Y. Park, S. K. Kang, H. D. Cho, and J. W. Lee, "Growth and p-type doping of GaN on c-plane sapphire by nitrogen plasma-assisted molecular beam epitaxy." *J. Cryst. Growth* **175-6,** 100-6 (1997).

28 B. Y. Ber, Y. A. Kudriavtsev, A. V. Merkulov, S. V. Novikov, D. E. Lacklison, J. W. Orton, T. S. Cheng, and C. T. Foxon, "Secondary ion mass spectroscopy investigations of magnesium and carbon doped gallium nitride films grown by molecular beam epitaxy." *Semicond. Sci. Technol.* **13,** 71-4 (1998).

29 D. J. Dewsnip, J. W. Orton, D. E. Lacklison, L. Flannery, A. V. Andrianov, I. Harrison, S. E. Hooper, T. S. Cheng, C. T. Foxon, S. N. Novikov, B. Y. Ber, and Y. A. Kudriavtsev, "MBE growth and characterization of magnesium-doped gallium nitride." *Semicond. Sci. Technol.* **13,** 927-35 (1998).

30 C. T. Foxon, T. S. Cheng, N. J. Jeffs, J. Dewsnip, L. Flannery, J. W. Orton, I. Harrison, S. V. Novikov, B. Y. Ber, and Y. A. Kudriavtsev, "Studies of p-GaN grown by MBE on GaAs(111)B." *J. Cryst. Growth* **189-190,** 516-18 (1998).

31 T. D. Moustakas, "Epitaxial growth of GaN films produced by ECR-assisted MBE." *Mat. Res. Soc. Symp. Proc.* **395,** 111-22 (1996).

32 M. Gross, G. Henn, J. Ziegler, P. Allenspacher, C. Cychy, and H. Schroder, "Characteristics of undoped and magnesium doped GaN films grown by laser induced MBE." *Mater. Sci. Eng. B* **59,** 94-7 (1999).

33 L. Chul, K. Jae-Eun, P. Hae Yong, S. T. Kim, and H. Lim, "Defect-related luminescence of Mg-doped n-GaN grown by hydride vapour-phase epitaxy." *J. Phys., Condens. Matter* **10,** 11103-10 (1998).

34 A. E. Nikolaev, Y. V. Melnik, N. I. Kuznetsov, A. M. Srelchuk, A. P. Kovarsky, K. V. Vassilevski, and V. D. Dmitriev, "GaN pn-structures grown by hydride vapor phase epitaxy." *Mat. Res. Soc. Symp. Proc.* **482,** 251-6 (1998).

35 T. Suski, P. Perlin, M. Leszczyrski, H. Teisseyre, I. Grzegory, J. Jun, M. Bodkowski, S. Porowski, K. Pakula, A. Wysmolek, and J. M. Baralowski, "Growth and properties of bulk single crystals of GaN." *Mat. Res. Soc. Symp. Proc.* **395**, 15-25 (1996).

36 I. Grzegory, M. Bockowski, B. Lucznik, M. Wroblewski, S. Krukowski, J. Weyher, G. Nowak, T. Suski, M. Leszczynski, H. Teisseyre, E. Litwin-Staszewska, and S. Porowski, "GaN crystals: growth and doping under pressure." *Mat. Res. Soc. Symp. Proc.* **482**, 15-26 (1998).

37 S. Porowski, "Bulk and homoepitaxial GaN-growth and characterisation." *J. Cryst. Growth* **189-190**, 153-8 (1998).

38 S. J. Pearton, C. B. Vartuli, J. C. Zolper, C. Yuan, and R. A. Stall, "Ion implantation doping and isolation of GaN." *Appl. Phys. Lett.* **67**, 1435-7 (1995).

39 J. S. Chan, N. W. Cheung, L. Schloss, E. Jones, W. S. Wong, N. Newman, X. Liu, E. R. Weber, A. Gassman, and M. D. Rubin, "Thermal annealing characteristics of Si and Mg-implanted GaN thin films." *Appl. Phys. Lett.* **68**, 2702-4 (1996).

40 A. Edwards, M. V. Rao, B. Molnar, A. E. Wickenden, O. W. Holland, and P. H. Chi, "Ion implantation doping of OMCVD grown GaN." *J. Electron. Mater.* **26**, 334-9 (1997).

41 J. C. Zolper, "Ion implantation in group III-nitride semiconductors: a tool for doping and defect studies." *J. Cryst. Growth* **178**, 157-67 (1997).

42 X. A. Cao, S. J. Pearton, R. K. Singh, C. R. Abernathy, J. Han, R. J. Shul, D. J. Rieger, J. C. Zolper, R. G. Wilson, M. Fu, J. A. Sekhar, H. J. Guo, and S. J. Pennycook, "Rapid thermal processing of implanted GaN up to 1500 degrees C." *MRS Internet J. Nitride Semicond. Res.* **4S1**, G6.33 (1999).

43 E. V. Kalinina, V. A. Solov'ev, A. S. Zubrilov, and V. A. Dmitriev, "GaN p-n structures fabricated by Mg ion implantation." *MRS Internet J. Nitride Semicond. Res.* **4S1**, G6.53 (1999).

44 C. J. Pan and G. C. Chi, "The doping of GaN with Mg diffusion." *Solid-St. Electron.* **43**, 621-3 (1999).

45 W. Kim, A. E. Botchkarev, A. Salvador, G. Popovidi, H. Tang, and H. Morkoc, "On the incorporation of Mg and the role of oxygen, silicon, and hydrogen in GaN prepared by reactive molecular beam epitaxy." *J. Appl. Phys.* **82**, 219-226 (1997).

46 C. G. Van de Walle, C. Stampfl, and J. Neugebauer, "Theory of doping and defects in III-V nitrides." *J. Cryst. Growth* **189/190**, 505-10 (1998).

47 U. Kaufmann, M. Kunzer, M. Maier, H. Obloh, A. Ramakrishnan, B. Santic, and P. Schlotter, "Nature of the 2.8 eV photoluminescence band in Mg doped GaN." *Appl. Phys. Lett.* **72**, 1326-8 (1998).

48 F. A. Reboredo and S. T. Pantelides, "Novel defect complexes and their role in the p-type doping of GaN." *Phys. Rev. Lett.* **82**, 1887-90 (1999).

49 J. Neugebauer and C. G. Van de Walle, "Theory of point defects and complexes in GaN." *Mat. Res. Soc. Symp. Proc.* **395**, 645-56 (1996).

50 W. Gotz, N. M. Johnson, J. Walker, D. P. Bour, and R. A. Street, "Activation of acceptors in Mg-doped GaN grown by metalorganic chemical vapor deposition." *Appl. Phys. Lett.* **68**, 667-9 (1996).

51 W. Gotz, R. S. Kern, C. H. Chen, H. Liu, D. A. Steigerwald, and R. M. Fletcher, "Hall-effect characterization of III-V nitride semiconductors for high efficiency light emitting diodes." *Mat. Sci. Eng. B* **59**, 211-17 (1999).

52 H. Teisseyre, B. Kozankiewicz, M. Leszczynski, I. Grzegory, T. Suski, M. Bockowski, S. Porowski, K. Pakula, P. M. Mensz, and I. B. Bhat, "Pressure and time-resolved photoluminescence studies of Mg-doped and undoped GaN." *Phys. Status Solidi B* **198**, 235-41 (1996).

53 E. Oh, H. Park, and Y. Park, "Excitation density dependence of photoluminescence in GaN:Mg." *Appl. Phys. Lett.* **72**, 70-2 (1998).

54 M. A. Reshchikov, G. C. Yi, and B. W. Wessels, "Defect luminescence in heavily Mg doped GaN." *MRS Internet J. Nitride Semicond. Res.* **4S1**, G11.8 (1999).

55 W. Gotz, N. M. Johnson, and D. P. Bour, "Deep level defects in Mg-doped, p-type GaN grown by metalorganic chemical vapor deposition." *Appl. Phys. Lett.* **68**, 3470-2 (1996).

56 P. Hacke, H. Nakayama, T. Detchprohm, K. Hiramatsu, and N. Sawaki, "Deep levels in the upper band-gap region of lightly Mg-doped GaN." *Appl. Phys. Lett.* **68**, 1362-4 (1996).

57 H. Nagai, Q. S. Zhu, Y. Kawaguchi, K. Hiramatsu, and N. Sawaki, "Hole trap levels in Mg-doped GaN grown by metalorganic vapor phase epitaxy." *Appl. Phys. Lett.* **73**, 2024-6 (1998).

58 A. A. Sliwinski, K. P. Korona, K. Pakula, and J. M. Baranowski, "Deep level transient spectroscopic studies of MOCVD GaN layers grown on sapphire." *Acta Physica Polonica A* **90**, 955-8 (1996).

59 S. C. Y. Tsen, D. J. Smith, K. T. Tsen, W. Kim, and H. Morkoc, "Microstructural study of Mg-doped p-type GaN: correlation between high-resolution electron microscopy and Raman spectroscopy." *J. Appl. Phys.* **82**, 6008-11 (1997).

60 L. Eckey, U. Von Gfug, J. Holst, A. Hoffmann, A. Kaschner, H. Siegle, C. Thomsen, B. Schineller, K. Heime, M. Heuken, O. Schon, and R. Beccard, "Photoluminescence and Raman study of compensation effects in Mg-doped GaN epilayers." *J. Appl. Phys.* **84**, 5828-30 (1998).

61 A. Kaschner, H. Siegle, A. Hoffmann, C. Thomsen, U. Birkle, S. Einfeldt, and D. Hommel, "Influence of doping on the lattice dynamics of gallium nitride." *MRS Internet J. Nitride Semicond. Res.* **4S1**, G3.57 (1999).

62 V. Ramachandran, R. M. Feenstra, W. L. Sarney, L. Salamanca-Riba, J. E. Northrup, L. T. Romano, and D. W. Greve, "Inversion of wurtzite GaN(0001) by exposure to magnesium." *Appl. Phys. Lett.* **75**, 808-10 (1999).

63 D. C. Look, *Electrical Characterization of GaAs Materials and Devices* (John Wiley & Sons, Chichester, England, 1989).

64 M. Suzuki and T. Uenoyama, "First-principles calculation of effective mass parameters of gallium nitride." *Jpn. J. Appl. Phys.* **34**, 3442-6 (1995).

65   G. D. Chen, M. Smith, J. Y. Lin, H. X. Jiang, W. Su-Huai, M. A. Khan, and C. J. Sun, "Fundamental optical transitions in GaN." *Appl. Phys. Lett.* **68,** 2784-6 (1996).

66   S.-H. Wei and A. Zunger, "Valence band splittings and band offsets of AlN, GaN, and InN." *Appl. Phys. Lett.* **69,** 2719-21 (1996).

67   Y. C. Yeo, T. C. Chong, and M. F. Li, "Electronic band structures and effective-mass parameters of wurtzite GaN and InN." *J. Appl. Phys.* **83,** 1429-36 (1998).

68   G. B. Ren, Y. M. Liu, and P. Blood, "Valence-band structure of wurtzite GaN including the spin-orbit interaction." *Appl. Phys. Lett.* **74,** 1117-19 (1999).

69   J. J. Pankove, S. Bloom, and G. Harbecke, "Optical Properties of GaN." *RCA Rev.* **36,** 163-176 (1975).

70   J. S. Im, A. Moritz, F. Steuber, V. Harle, F. Scholz, and A. Hangleiter, "Radiative carrier lifetime, momentum matrix element, and hole effective mass in GaN." *Appl. Phys. Lett.* **70,** 631-3 (1997).

71   S. Strite and H. Morkoc, "GaN, AlN, InN: A review." *J. Vac. Sci. Technol. B* **10,** 1237-66 (1992).

72   E. F. Schubert, *Doping in III-V Semiconductors* (Cambridge University Press, Cambridge, UK, 1993).

73   X. H. Wu, P. Fini, S. Keller, E. J. Tarsa, B. Heying, U. K. Mishra, S. P. DenBaars, and J. S. Speck, "Morphological and structural transitions in GaN films grown on sapphire by metal-organic chemical vapor deposition." *Jpn. J. Appl. Phys.* **35,** L1648-51 (1996).

74   M. Bartram, private communication (1999).

75   P. P. Debye and E. M. Conwell, "Electrical properties of n-type germanium." *Phys. Rev.* **93,** 693-706 (1954).

76   D. C. Look, D. C. Walters, G. D. Robinson, J. R. Sizelove, M. G. Mier, and C. E. Stutz, "Annealing dynamics of molecular-beam epitaxial GaAs grown at 200 C." *J. Appl. Phys.* **74,** 306-10 (1993).

77   P. Boguslawski and J. Bernholc, "Doping properties of C, Si, and Ge impurities in GaN and AlN." *Phys. Rev. B, Condens. Matter (USA)* **56,** 9496-505 (1997).

78   M. D. Bremser, W. G. Ferry, N. V. Edwards, T. Zheleva, N. Parikh, D. E. Aspnes, and R. F. Davis, "Growth and doping of $Al_xGa_{1-x}N$ deposited directly on alpha (6H)-SiC(0001) substrates via organometallic vapor phase epitaxy." *Mat. Res. Soc. Symp. Proc.* **395,** 195-200 (1996).

79   M. Katsuragawa, S. Sota, M. Komori, C. Anbe, T. Takeuchi, H. Sakai, H. Amano, and I. Akasaki, "Thermal ionization energy of Si and Mg in AlGaN." *J. Cryst. Growth* **189-190,** 528-31 (1998).

80   M. L. Timmons, P. K. Chiang, and S. V. Hattangady, "An alternative Mg precursor for p-type doping of OMVPE grown material." *J. Cryst. Growth* **77,** 37-41 (1986).

81   T. F. Kuech, P. J. Wang, M. A. Tischler, R. Potemski, G. J. Scilla, and F. Cardone, "The control and modeling of doping profiles and transients in MOVPE growth." *J. Cryst. Growth* **93,** 624-30 (1988).

82 Y. Ohba and A. Hatano, "A study on strong memory effects for Mg doping in GaN metalorganic chemical vapor deposition." *J. Cryst. Growth* **145**, 214-218 (1994).

83 R. G. Wilson, S. J. Pearton, C. R. Abernathy, and J. M. Zavada, "Thermal stability of implanted dopants in GaN." *Appl. Phys. Lett.* **66**, 2238-40 (1995).

84 C. Ying-Lan, M. Ludowise, D. Lefforge, and B. Perez, "Study of Mg diffusion during metalorganic chemical vapor deposition of GaN and AlGaN." *Appl. Phys. Lett.* **74**, 688-90 (1999).

85 X. A. Cao, R. G. Wilson, J. C. Zolper, S. J. Pearton, J. Han, R. J. Shul, D. J. Rieger, R. K. Singh, M. Fu, V. Scarvepalli, J. A. Sekhar, and J. M. Zavada, "Redistribution of implanted dopants in GaN." *J. Electron. Mater.* **28**, 261-5 (1999).

Chapter 3

Processing of Mg-doped GaN

3.1 Introduction

There are three major issues for the processing of Mg-doped p-type GaN. The first is optimization of the activation procedure, a thermal anneal which is used to dissociate the Mg-H complex and create active Mg acceptors. The second concern is to develop a recipe for producing ohmic contacts. The final item is the development of a low-damage etch technique. The first two subjects have received considerable attention in the literature, however no consensus has emerged on optimized procedures. The literature on ohmic contacts is particularly difficult to interpret, as it is plagued by variations in experimental procedure and measurement techniques. Damage induced in GaN by plasma etching techniques has received some attention in the literature for the case of n-type material, but very little experimental work has been performed on p-type GaN. However, with the advent of GaN-based bipolar transistors, which require an etch step to reveal the p-type base layer, this has become an important issue.

Sections 3.2 and 3.3 of this dissertation present experimental work on activation procedures and ohmic contacts, respectively. The "standard" procedures developed in this work are summarized in Appendix A, and a detailed discussion of the contact resistance measurement technique is presented in Appendix B. Experiments on plasma-induced damage to p-type GaN are described in section 3.4.

3.2 Activation

The nature of the hydrogen passivation mechanism within Mg-doped GaN has been the subject of extensive study ever since the phenomenon was first identified. Following the early experimental work by Akasaki's and Nakamura's groups,[1-4] a number of theoretical studies have been published on the energetics of hydrogen passivation and the nature of the Mg-H bond.[5-11] Experimental work has utilized Hall effect measurements,[12-16] Raman spectroscopy,[17] photoluminescence,[16,18,19] and re-hydrogenation[20] or deuteration.[15] It appears that the incorporation of hydrogen during the growth of Mg-doped GaN is an energetically favorable process, resulting in films that are highly resistive until annealed at temperatures above ~600°C. At this point the Mg-H bond is broken, although the hydrogen does not necessarily leave the crystal. Re-passivation of the acceptors occurs upon subsequent exposure to hydrogen or deuterium at temperatures greater than ~450°C. The optimum annealing conditions reported have varied widely, with temperatures between 700°C and 1140°C and anneal times between 20 min and 60 seconds. The activation process can be enhanced (and therefore will occur at lower temperatures) if it is performed under UV light[21] or minority carrier injection in a p-n junction.[22,23] There is also some evidence that the activation process is dependent on the dislocation and defect density within the film.[24,25]

For device considerations, the paramount issue is simply the optimization of the activation anneal for the highest possible p-type conductivity. Our initial experiments in this area were performed using 3-minute treatments in a rapid thermal annealer (RTA) with a N_2 atmosphere. These experiments were performed before the ohmic contact and Hall measurement processes for p-type GaN were developed; as a result, the material was characterized only through resistivity measurements and measurements of the turn-on voltage of p-n diodes.

The results of this first activation study are presented in figures 3.1 and 3.2. The measured resistivity dropped to around 1 Ω cm as the samples were annealed at higher temperature, as shown in figure 3.1. The turn-on voltages of p-n junctions fabricated from these layers are shown in figure 3.2 (For this study, we defined the turn-on voltage as the intercept of a line fit to the I-V curve between 40 mA and 60 mA.) The turn-on voltages are quite high, which results from the non-ohmic nature of the p-contacts on these samples. For uncapped samples, the turn-on voltage drops as the activation temperature is increased to 900°C, but then increases again. The higher turn-on voltage for the uncapped sample annealed at 950°C is attributed to a poorer tunneling contact, most likely a result of compensation of the near-surface layers due to nitrogen loss during the high temperature anneal.

In order to combat this nitrogen loss, we began using a SiO_2 cap during the activation procedure. This cap is 1000 Å thick and deposited by plasma-
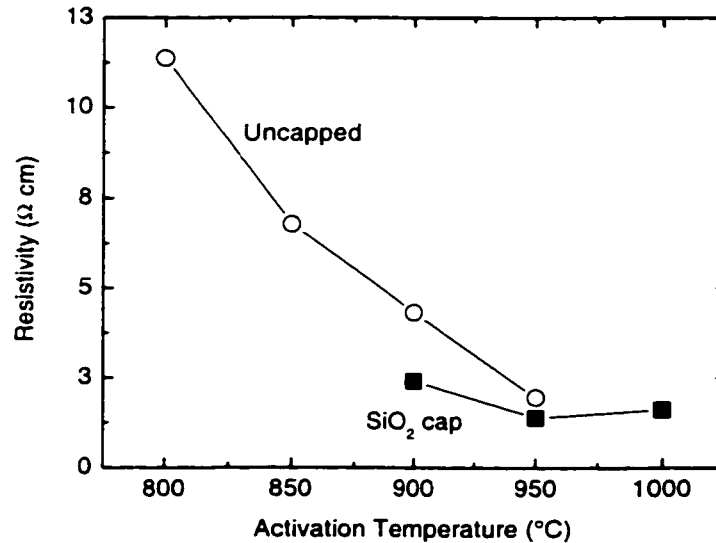

Figure 3.1   Resistivity of Mg-doped GaN layers as a function of activation anneal temperature. The anneals were performed for 3 minutes in a N_2 atmosphere using an RTA.

enhanced chemical vapor deposition (PECVD). As shown in figure 3.2, use of the SiO_2 cap permits activation at 950°C without degradation of the contact properties, although the contact does degrade if the temperature is raised to 1000°C. Figure 3.1 shows that the resistivity obtained with the SiO_2 cap is as low or lower than that obtained on uncapped samples. After the anneal, the SiO_2 cap is removed using a long soak (10 min) in buffered HF (BHF) acid. This long soak was found to be necessary in order to fully remove the cap, perhaps because the SiO_2 densifies during the annealing step or because slow-etching SiN_xO_y forms near the interface.

Following these results, we adopted the 3-minute 950°C anneal with SiO_2 cap as our "standard" activation procedure. This activation procedure was used to activate all the Mg-doped GaN films whose characteristics are described in other sections of this dissertation. The process flow for this activation anneal is given in Appendix A.
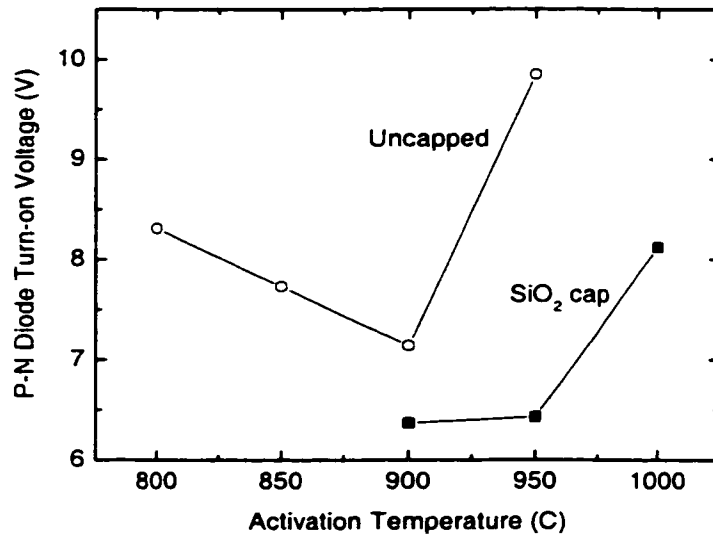

Figure 3.2 Turn-on voltage of GaN *p-n* diodes as a function of the activation anneal temperature.

70

A number of other activation conditions were examined in later studies. Of particular interest were longer anneals at lower temperatures, which we hoped might give comparable electrical results while minimizing damage to the crystal (especially any InGaN layers), and could be compatible with some metallizations providing greater freedom in process design. Figure 3.3 shows Hall effect measurement results on a number of activation anneal studies performed at different temperatures and for different lengths of time. All of these samples had 1000 Å thick SiO_2 caps. A separate growth was used for each isochronal study. All the anneals were performed in the RTA except for the 1 hour samples; these were annealed in a tube furnace.
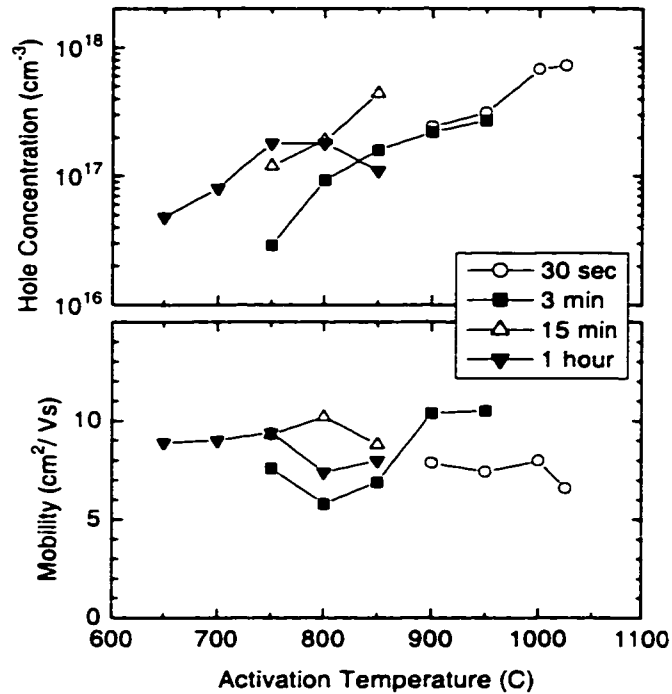

Figure 3.3 Hall effect measurements on Mg-doped GaN films as a function of activation anneal time and temperature. All samples were capped with 1000Å SiO_2 during the anneal.

71

It appears from figure 3.3 that the room-temperature hole concentration of the films is determined primarily by the activation temperature, while the anneal time plays a secondary role. Overall, the best results were obtained on samples annealed at higher temperatures and for shorter times. While this trend is quite clear, one must be careful in comparing the specific data presented in figure 3.3 because of significant variations in doping and compensation level that may exist in the various samples used. For example, a piece from the growth used for the 15 minute anneal study was activated using the "standard" procedure, resulting in a hole concentration of 6×10^{17} cm^{-3}. This value is twice that obtained on a different growth under the same activation conditions (the 3-minute sample at 950°C in figure 3.3) The disparity suggests that the 15-minute sample is either more heavily doped or more lightly compensated. Finally, we note that the measured hole mobility is basically independent of activation conditions. This is consistent with the model presented in chapter 2, where it was suggested that the
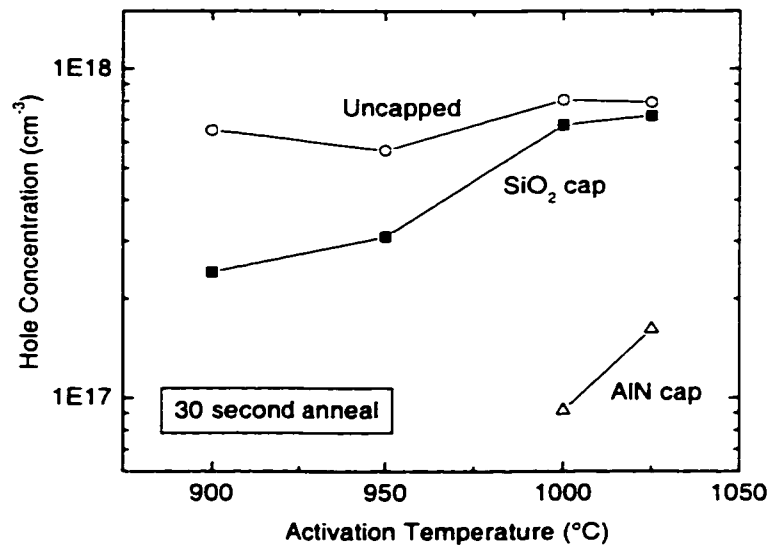

Figure 3.4 Hole concentration measured on Mg-doped GaN samples activated with different cap materials.

hole mobility in these films is primarily controlled by the density of compensating donors (and should therefore be unaffected by the activation anneal).

The material used to cap the sample during activation has also been investigated in several experiments. Figure 3.4 presents the hole concentration measured on samples activated at various temperatures for 30 seconds. In this experiment, a slightly lower hole concentration was obtained using an SiO_2 cap than no cap at all. Using a sputtered AlN cap, the hole concentration was lower still. Similar results were obtained in an experiment comparing PECVD-deposited SiN and SiO_2 caps in a 950°C 3-minute anneal: the resulting hole concentration was 7×10^{17} cm^{-3} using SiO_2, but only 1×10^{16} cm^{-3} using SiN. These results suggest that some cap materials suppress the activation process, perhaps by keeping hydrogen trapped within the crystal.

In summary, a number of activation conditions have been investigated. Comparisons are made difficult because of material quality variations, but the trends suggest that short, high-temperature anneals may provide the optimal results. Care should be taken in applying these results to device structures containing InGaN, however, as that material may degrade at the higher temperatures. Capping the sample helps the surface survive the anneal; of the investigated materials, SiO_2 provides the best cap. The "standard" activation procedure given in appendix A is a good starting point but does not necessarily represent an optimized activation procedure.

3.3 Ohmic contacts

The development of an ohmic contact technology for p-type GaN is of obvious importance for device work and has been the subject of considerable research by various groups around the world. An ohmic contact recipe consists of three parts: surface preparation, choice of metals, and annealing procedure. These three elements are all addressed in this section.

Before addressing the process recipes, however, it is important to discuss the measurement technique that is used to characterize the contacts. The transfer length model (TLM) technique is typically used to analyze ohmic contacts to semiconductors. Contact pads separated by varying distances are used to separate the specific contact resistance (r_C) from the sheet resistance of the material. However, the contacts to p-type GaN are usually not perfectly ohmic, and so they cannot be accurately described by a single contact resistance value. This fact has been ignored by many authors, and has led others to define various new measurement techniques, some of which are ill defined or provide incorrect results. As a result, the literature on ohmic contacts to p-type GaN is especially difficult to interpret and contains many conflicting results and meaningless numbers. Nonetheless, certain trends can be observed where consistent analysis has been performed.

In this work, the contacts have been characterized using a modified TLM technique in which the dynamic resistance is measured from the slope of the I-V curve. For each contact spacing, the dynamic resistance is recorded at the same current level; the results are fit to the standard TLM equation to yield the contact resistance *at that current value* (in this work, a current of 100 μA was used). It is important to keep the current level the same so that each measurement is taken with the contact under the same electrical bias. If a constant voltage is applied instead, then the contact bias will vary as the spacing changes—as a result

74

erroneously low contact resistance values are calculated. The application of TLM measurements to non-ohmic contacts is discussed in detail in Appendix B.

Surface preparation

Surface contamination prior to metallization may occur either as a result of air exposure or photoresist scum left on the surface after photolithography. The latter can be avoided by using a blanket evaporation followed by a metal etch for patterning, but this technique cannot be easily applied if there are pre-existing metal contacts on the wafer. When lithography is performed before metallization, a brief oxygen plasma treatment is typically used after development in order to remove any photoresist scum left in the opening. In our studies on p-type GaN, however, it emerged that such an oxygen plasma treatment led to substantial surface damage and severely degraded the contact qualities. This plasma damage is discussed in section 3.4.

Various alternatives to the oxygen plasma treatment for removing photoresist scum were tested. Figure 3.5 shows the I-V characteristics obtained between two Pd/Au contacts on p-type GaN where various different scum removing treatments were applied after developing the photoresist. In each case, acid treatments were employed after the scum removal to clean up any oxide. The treatments tested were: 30 second oxygen plasma exposure at 100 W, 30 second dip in NH_4OH diluted with de-ionized (DI) water 1:1, 30 minute ozone exposure, and a second lithographic step. The last of these, in which the sample was exposed again (blanket exposure) to the UV light source and then developed again, was designed to ensure that all the photoresist scum is developed away. This technique provided the best results and was therefore used regularly; it forms part of the p-contact recipe provided in Appendix A. We note that in these experiments image-reversal photoresist was used. Using this sort of photoresist allows the "second exposure" technique to be used without any danger of

destroying the desired lithographic pattern. If normal positive resist is needed in a process step, the double exposure technique will likely not work well. In this case, there is another process which works equally well but is somewhat more time consuming: an evaporated SiO_2 layer (~1000 Å) is used to protect the surface of the GaN from the photoresist processing. With the SiO_2 protection, an oxygen plasma descum may be safely employed. Using BHF acid, the SiO_2 in the opening is then removed prior to evaporation.

Cleaning procedures to remove atmosphere-induced contamination of GaN surfaces have received some attention in the literature. Smith, et al. and King, et al. have found that HCl solutions are more effective than HF solutions in removing surface oxides, judging from Auger electron spectroscopy measurements of the surface chemistry,[26,27] while Prabhakaran, et al. have obtained good results with NH_4OH solutions.[28] For the particular case of Mg-doped GaN, Lee, et al. have found surface treatment to be of great importance and
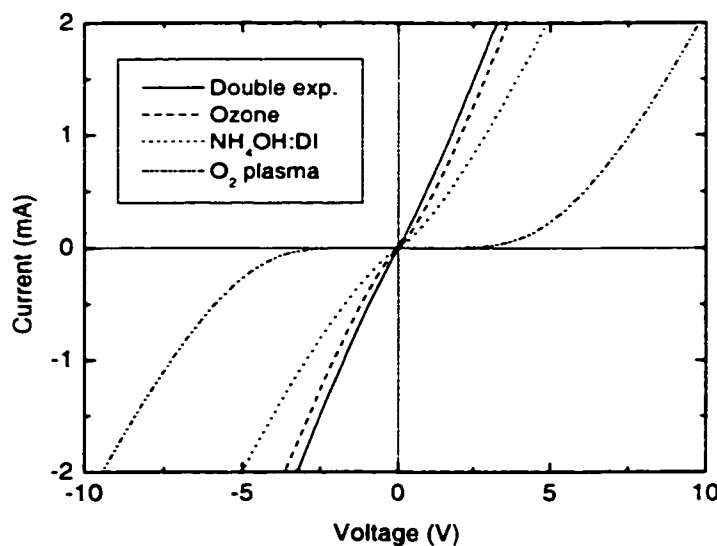

Figure 3.5 I-V characteristics between two p-contacts formed using various different treatments to remove photoresist scum.

report significantly improved contacts as a result of surface cleaning in boiling KOH,[29] or boiling aqua regia (HCl:HNO$_3$ 3:1).[30] They also report x-ray photoelectron spectroscopy measurements indicating that these surface treatments yield a lower surface concentration of oxygen than that found on a sample treated with HCl alone. We note that both of these treatments will destroy photoresist and must therefore be applied before lithography; the time taken for lithography may then emerge as an important parameter. Another phenomenon that could be of importance in considering surface treatments is unintentional hydrogenation and consequent acceptor passivation. SIMS measurements have revealed significant hydrogen incorporation from exposing GaN films to boiling water or to KOH-based solutions;[31] the electrical consequences of this effect have not been measured.

We performed a small study of different surface treatments in order to improve the p-type contacts obtained on our material. Several pieces were cut from the same sample and all were processed with the double-exposure
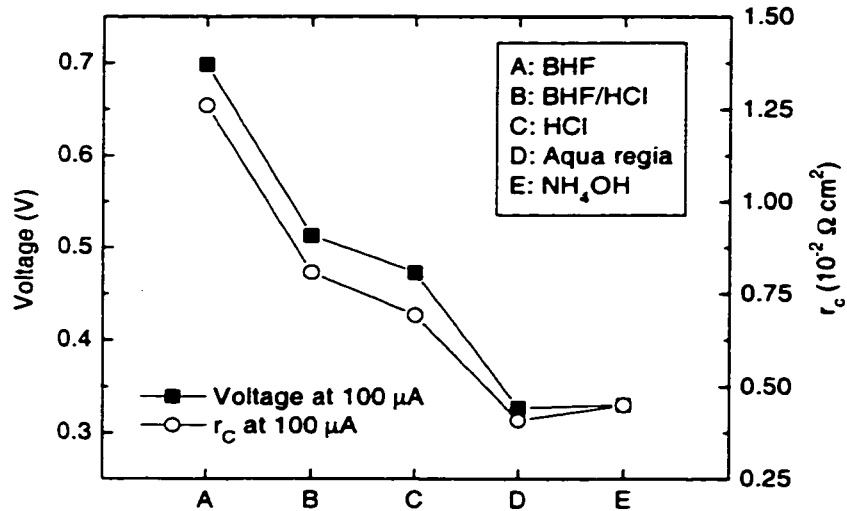

Figure 3.6 Specific contact resistance r_C at 100 μA and voltage at 100 μA for samples with different cleaning treatments prior to metal evaporation (the treatments are described in the text).

lithography technique. After lithography, sample A was soaked in BHF for 10 minutes, while sample B was soaked first in BHF (20 seconds) and then in HCl:DI 1:4 (20 seconds), and sample C was soaked in undiluted HCl for 10 minutes. Samples D and E were used to test pre-lithography treatments: sample D was placed in boiling aqua regia (120 °C) for 10 minutes, while sample E was soaked in undiluted NH_4OH (room temperature) for 10 minutes. After lithography, both samples were given a 2 minute HCl dip and then loaded into the evaporator (total time since pre-lithography treatment was around 1.5 hours). The results of these experiments are shown in figure 3.6. This plot shows both the contact resistance measured by the modified TLM technique at a current of 100 μA and the voltage at that current between two contacts separated by 3 μm.

The results indicate that the HCl dip is important and provides a significantly lower contact resistance than a BHF dip alone. The pre-lithography cleaning steps also seem to improve the contact resistance. We note that the measured voltage tracks closely with the contact resistance, indicating that even though the contacts are not quite ohmic, the value of the specific contact resistance r_c is a useful measure for assessing the quality of the contacts. No surface chemistry analysis was performed on these samples, but the studies reported in the literature suggest that the contact improvement is likely due to a reduced surface oxide layer.

Metal	ϕ_M (eV)
Au	5.1
Cr	4.5
Ni	5.1
Pd	5.2
Pt	5.7
Ti	4.3
W	4.6

Table 3.1 Work function of various metals.

78

Finally, we note that these studies may be easily corrupted by material variation, even over different pieces from the same wafer. The contact resistance has been shown to be strongly affected by the growth temperature (see section 2.8), which is known to vary considerably over the wafer. The improved contact resistance that results from the HCl treatment has been confirmed in several experiments, so this result can be stated with some confidence. However, the effect of the pre-lithography surface clean was tested only in this one experiment, so further studies are required to ensure that the results are not an artifact of material variation.

Choice of metals

The valence band of GaN lies very deep below the vacuum level (~7.5 eV). In the absence of surface pinning, one would like to use a metal with a work function (ϕ_M) close to this value in order to minimize the surface depletion region barrier. Table 3.1 presents a list of work-function values for various
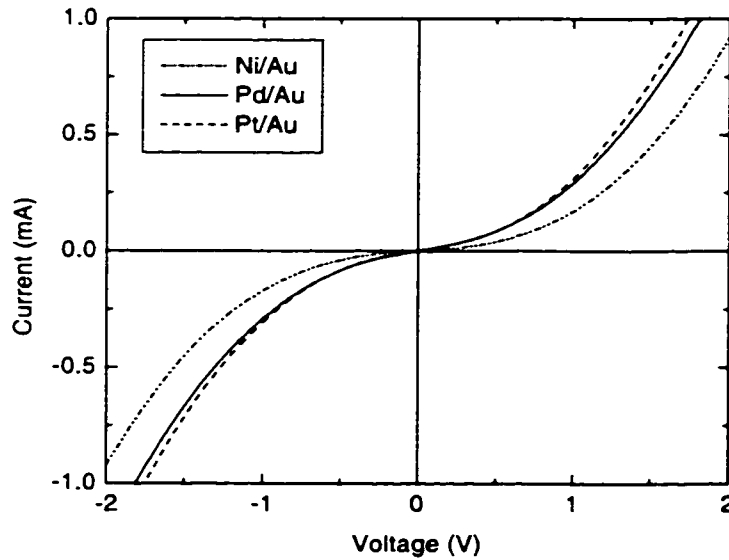

Figure 3.7 I-V characteristics of contacts as-deposited on *p*-type GaN. The contacts are 200 μm wide and separated by 3 μm.

79

metals—all are much below 7.5 eV, guaranteeing a barrier height of at least ~1.8 eV at the metal/semiconductor interface. This is doubtless one reason that it is so difficult to form ohmic contacts to p-type GaN.

A wide variety of metal combinations for contacts to p-type GaN have been reported in the literature including Au,[32,33] Ni/Au,[32,34,35] Mg/Au,[33] Pd/Au,[34,36] Pt/Au,[37] Cr/Au,[34] Cr/Ni/Au,[38] Ni/Pt/Au,[39] Ni/Si,[40] Ta/Ti,[41,42] W,[43] WSi$_x$,[43] NiIn,[44] Pt$_3$In$_7$.[45] and indium tin oxide.[46] While there is no consensus on the optimum metal scheme, most device work has used Ni/Au or Pd/Au contacts.

We have tested various metal schemes on p-type GaN. Schottky-type contacts were obtained using Al/Ni/Au and Cr/Au metallizations. Using higher work-function metals such as Ni/Au, Pd/Au, and Pt/Au, "almost-ohmic" contacts to p-type GaN have been obtained. The I-V characteristics of unannealed Ni/Au, Pd/Au, and Pt/Au contacts are shown in figure 3.7. In a number of comparisons, Pd/Au has yielded the lowest contact resistance, so this metallization scheme was adopted as the standard procedure. The typical layer thicknesses used are 250 Å of Pd and 2500 Å of Au. The contacts are quite ohmic without annealing, so they were usually left in this state. This standard metallization procedure, listed in Appendix A, was used to create the contacts for all the electrical measurements presented in this dissertation.

Contact annealing

Various authors have investigated annealing conditions for various different contact metallizations, reporting optimum anneal temperatures between 400°C and 900°C.[32,34,38,41,45] Most reported anneals are performed at 400 – 500°C in a N$_2$ ambient, and most authors cite intermixing and metal diffusion as the mechanisms responsible for the contact improvements. Two groups have reported recently on the effects of annealing in an O$_2$ containing ambient, which

leads to significantly improved Ni/Au contacts.[47-49] The authors suggest that NiO and/or Ni-Ga-O phases may contribute to the lower contact resistance.

In our experiments, we have studied the annealing of both Ni/Au and Pd/Au contacts. Figure 3.8 shows the specific contact resistance r_C measured for these samples as a function of annealing time. In order to minimize the effect of material variation, the same two samples were used throughout and annealed consecutively at higher temperature. Each anneal was performed for 1 minute in a N_2 atmosphere. For both contacts, low-temperature anneals caused the resistance to increase slightly from the as-deposited case. For the Ni/Au contact, the resistance did not recover until the anneal temperature reached 650°C. At that temperature the Ni/Au contacts began to turn dark and became quite rough on the surface. Further annealing at higher temperatures caused the contact resistance to continue dropping slowly for these Ni/Au contacts.
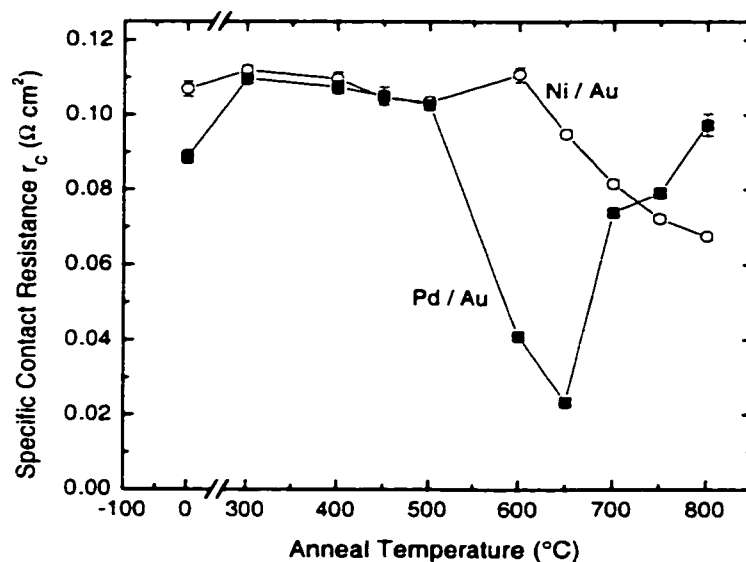

Figure 3.8 Contact resistance of Pd/Au and Ni/Au contacts as a function of anneal temperature. Anneals were carried out consecutively on the same samples. Each anneal lasted 1 minute and was performed in a N_2 ambient.

81

The contact resistance for the Pd/Au contacts dropped sharply when the anneal temperature was between 600 and 650°C. The contact resistance increased again when annealed at higher temperatures. In addition, the surface of the metal took on a silver appearance while the bottom (viewed through the substrate) took on a gold color, suggesting that the Pd may have risen to the surface. The contact resistance reduction with the 650°C anneal is significant—a factor of four from the as-deposited case. (Figure 3.9 compares the I-V curves obtained from as-deposited Pd/Au contacts and contacts annealed at 650°C.) The sharp minimum in contact resistance at the anneal temperature of 650°C suggests that there may be a new phase being formed at this temperature. We also note that it is at ~600°C that the Mg-H begins to dissociate. Pd can absorb (and transmit) large quantities of hydrogen when it is heated, so a hydrogen gettering effect which leaves a higher active acceptor concentration under the contact may play a role in
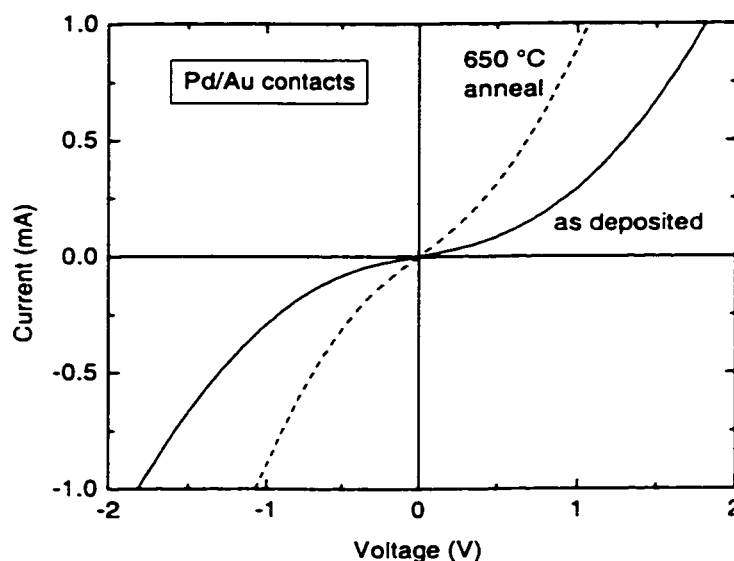

Figure 3.9 I-V characteristics between two Pd/Au contacts as-deposited (solid line), and after 650 °C anneal (dashed line). The contacts are 200 μm wide and separated by 3 μm.

the contact resistance minimum. A similar mechanism has been proposed to explain the contact resistance reduction in TaTi contacts.[42]

Appendix A lists the optimized ohmic contact recipe derived from the research presented in this dissertation. While lithographic techniques, surface treatments, metal choices, and anneal conditions have all been investigated to some degree, there is a large parameter space available of which only a small area has been tested. The contact improvements presented here have played an important role in furthering the device work at UCSB; additional incremental improvements in the contact recipe are expected as the research progresses, and will lead to enhanced device performance. Of particular interest is the optimization of the contact anneal time and temperature for Pd/Au contacts, which should be carried out in conjunction with microstructural analysis to determine the mechanism of the contact resistance reduction.

3.4 Plasma damage to p-type GaN

Plasma processing of GaN and related alloys is an important technology for the fabrication of various electronic and optoelectronic devices. Dry etching in chlorine-based gas plasmas is a widely used technique as a result of the well-documented difficulties in wet etching of the nitride materials.[50] Other gas plasmas are also commonly used in semiconductor processing, including O_2 plasmas to remove hydrocarbon contamination and fluorine-containing plasmas for dielectric etching. It is well known from conventional semiconductors that such plasma processing may induce significant damage in the near-surface region of the crystal. Various groups have investigated this plasma-induced damage in n-type GaN,[51-56] and recent research has begun to focus on p-type material.[57,58]

Plasma processing of p-type GaN can be avoided in most optoelectronic device structures, in which the p-type layers are typically placed on top.

83

However, with the recent development of bipolar junction transistors in this material system,[59-61] the need for dry etching to reveal the base layer has brought the issue of plasma damage in p-type GaN to the forefront. In these devices, ohmic base contacts have not yet been successfully obtained, and etch damage has been identified as the major stumbling block. Various approaches to circumvent this problem, including burying the etch damage with a p-type regrowth,[59] have yielded only partial success. A thorough understanding of the nature and extent of plasma damage to p-type GaN, and of post-plasma methods to reduce the damage and achieve ohmic contacts, will clearly be necessary in order to achieve high performance GaN-based bipolar transistors. In this section we present an investigation into the effect of plasma damage from reactive ion etching on contacts to p-type GaN, and also discuss techniques for recovering from the induced damage.

Several authors have documented the properties of Schottky diodes on plasma-exposed n-type GaN surfaces, finding increased leakage and reduced barrier heights in both reactive ion etching[51] and inductively coupled plasma[55] configurations. The proposed mechanism for this effect is preferential loss of nitrogen from the near-surface region, leading to an increased n-type doping level in these layers.[50,54] Indeed, low power plasma exposures have been found to improve the performance of ohmic contacts to n-type GaN.[52,62] High power plasma exposures, however, have been found in some cases to increase contact resistance, indicating that the damage may also produce other types of deep states.[52,53] In p-type GaN, the formation of any type of damage-related donor state, whether shallow or deep, will lead to compensation of the acceptors in the near-surface region and cause a severe degradation of the contact properties. The high acceptor concentration typically employed in Mg-doped p-type GaN (around 10^{20} cm^{-3}), implies that a similarly high density of compensating donors is

introduced in the surface layers by the plasma process; this is a surprisingly high damage density.

The GaN samples in this study were grown using the "standard growth conditions" and consisted of a 1 µm Mg-doped GaN layer grown on top of a 3 µm thick n-type GaN layer. The plasma exposures were carried out in a Plasma Therm SLR-770 reactive ion etcher at a pressure of 10 mT. The gas chemistry and the plasma power were varied. After the plasma exposure, a solvent clean was performed and Pd/Au contacts were deposited using the standard double-exposure process of appendix A. The contacts were tested by examining the current-voltage (I-V) characteristics between two metal contact pads 200 µm wide which were separated by 5 µm.

Figure 3.10 shows the I-V characteristics of such contacts deposited on samples etched in a Cl_2 gas plasma. The plasma power was varied between 20 W
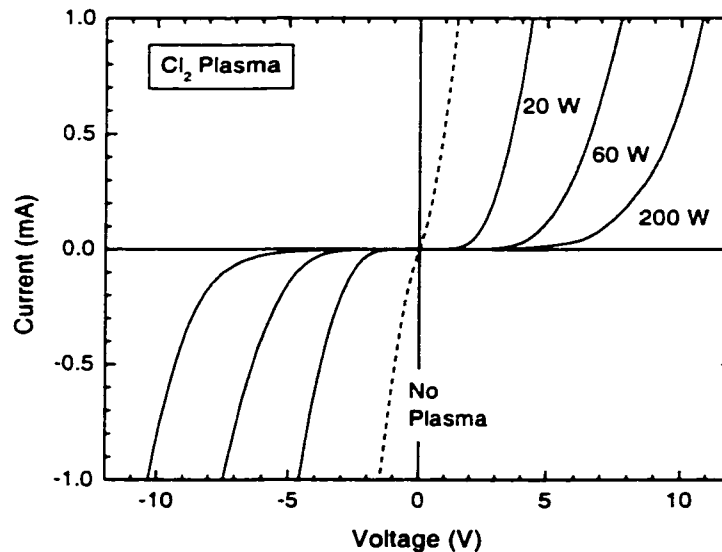

Figure 3.10 I-V characteristics obtained on samples etched in Cl_2 plasmas at different plasma powers. The dashed line is the I-V characteristic obtained on a sample which was not exposed to any plasma.

85

and 200 W, corresponding to an electrode bias between −23V and −390V. Under these conditions, the etch rate varies linearly with plasma power, and the etch time was therefore adjusted inversely with power in order to keep the etch depth constant (700 Å). It is clear from the I-V curves shown in figure 3.10 that Cl_2 plasma etching significantly degrades the p-type contacts. The I-V characteristics on the damaged samples are indicative of back-to-back Schottky type contacts, so that the current in either direction is limited by the breakdown of the reverse-biased contact. Etching at higher powers clearly exacerbates the effect. This observation is in agreement with the data of Chen et al., who found that excellent Schottky contacts to n-type AlGaN/GaN high electron mobility transistors could be obtained only by reducing the plasma power used during gate recess etching.[63] These results suggest that low power plasmas are most desirable in order to reduce the amount of physical damage to the crystal.
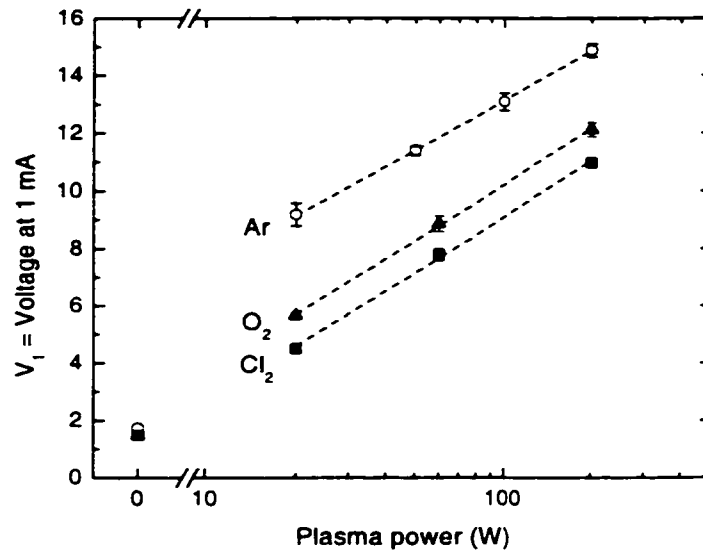

Figure 3.11   The voltage V_1 measured on samples exposed to various plasma chemistries and powers.   The open circles represent samples exposed to an Ar plasma, the solid triangles and squares indicate O_2 and Cl_2 plasmas respectively.

86

In order to quantify the experimental data we chose the voltage required to drive a current of 1 mA between two p-contacts (labeled V_I) as a measure of the extent of the plasma-induced damage. In figure 3.11, the voltage V_I is plotted for plasma exposures at various plasma powers and in various gas ambients. Oxygen plasma treatments are frequently used to remove photoresist and other hydrocarbons, but have been shown in section 3.3 to degrade contacts on p-type GaN. Argon plasmas were also tested as a comparison gas that should not interact chemically with GaN. Unlike the case with the Cl_2 plasma, all the argon and oxygen plasma exposures were performed for a constant time (2 minutes each). The GaN sputtering rate and oxide formation rates in these plasmas have not been measured. The electrode bias for these exposures varied from -37 V to -427 V.
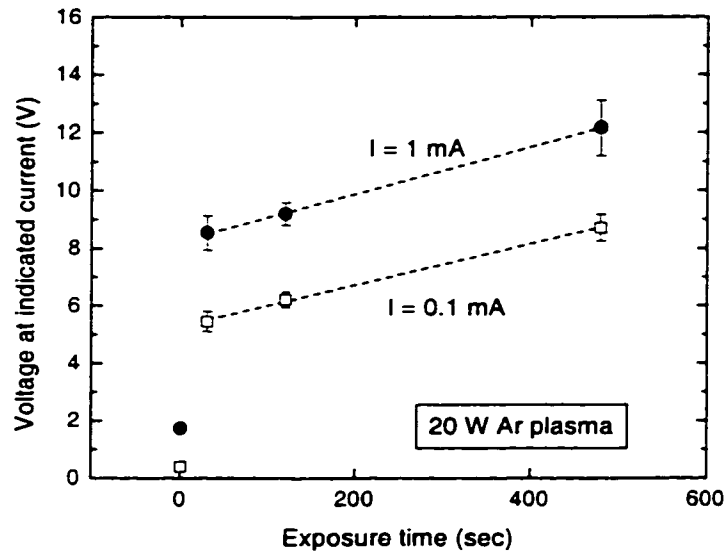

Figure 3.12 The voltages at a current of 1 mA (V_I, solid circles) and 0.1 mA ($V_{0.1}$, open squares) measured on samples exposed to a 20 W Ar plasma for varying lengths of time. The data points at an exposure time of zero were obtained from a sample that was never exposed to any plasma.

All three gas chemistries show the same trend of increasing contact degradation at higher plasma powers. In fact, the voltage V_1 appears to follow a similar logarithmic dependence on plasma power in all cases. The origin of this precise functional dependence is not understood at this time, and may indeed prove to be coincidental. Nonetheless, the similarity between the results with various gas chemistries suggests that the contact degradation is due to a purely physical damage mechanism and does not depend on chemical interactions between the process gas and the GaN sample. Cl_2 plasmas produce the smallest effect on the contact I-V, probably because the most heavily damaged material is constantly being removed by the etch process. The O_2 plasma might be expected to provide more serious contact degradation due to oxide formation, however that oxide was likely removed during the HCl dip prior to evaporation. The effect of changing the ion dose was studied by varying the exposure time in the 20 W Ar plasma, and the resulting values of V_1 are plotted in figure 3.12. It is clear that a very short exposure time creates sufficient damage to destroy the ohmic contact properties. Further increasing the dose appears to cause only a slow additional rise in V_1. For comparison, the voltage required for a current of 0.1 mA $(V_{0.1})$ has also been plotted on figure 3.12; these values are slightly lower than the V_1 values but follow the same trend.

If the plasma-induced damage was confined to a thin surface layer, ohmic contacts could be restored with an annealing step to diffuse the metal past the damaged material. In order to test this possibility, contact annealing experiments were performed on a sample etched in a 20 W Cl_2 plasma. The sample was annealed for 1 minute in a N_2 atmosphere at 300 °C, and then consecutively at higher temperatures up to 800 °C in increments of 100 °C. After each anneal the value of V_1 was measured; these data are presented in figure 3.13. There is very little variation evident in these values, which never regain the low value (1.6 V) obtained in the undamaged sample. The thickness of the damaged layer therefore

appears to be considerably larger than the metal diffusion depth for Pd/Au contacts. While these distances are not known, we note that deep damage may be expected because of channeling along the c-axis direction. (In an experiment on n-type GaN, Cao, et al. estimated a damage depth of 600 Å from an inductively coupled N$_2$ plasma).[55]

A number of approaches have been suggested in the literature for repairing damaged surfaces or removing damaged material. Among these are: a 30 second anneal in N$_2$ at 750 °C,[55] a 10 second dip in H$_3$PO$_4$ at 180 °C,[64] and ozone-induced oxide formation followed by an oxide removal in acid.[60] In our experiments the only technique which provided significant improvement of the I-V characteristics was a high temperature anneal with a sputtered AlN cap to prevent nitrogen loss. Such high temperature anneals have been used to heal implant damage in GaN and have enabled successful p-type doping through Mg
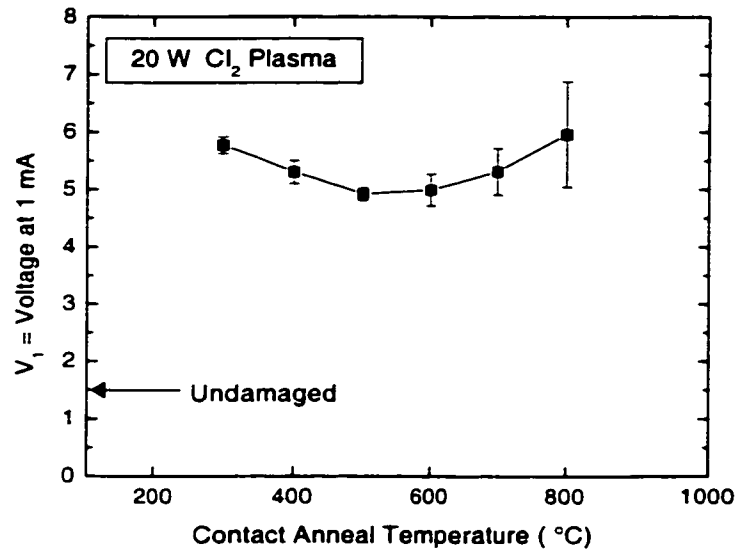

Figure 3.13 The voltage V_1 measured on a sample which was exposed to a 20 W Cl$_2$ plasma. After contact deposition, the sample was annealed at progressively higher temperatures; the voltage V_1 was measured after each anneal. The value of V_1 obtained on an undamaged sample is indicated with an arrow.

implantation.[65,66] The I-V characteristic shown in figure 3.14 was obtained using a 15 second anneal in N_2 at 1200 °C as a post-etch treatment. The contacts are significantly improved from those obtained on the damaged sample, but are still not as conductive as those measured on the undamaged film. These results are fairly preliminary; further investigations of high temperature annealing procedures to heal the p-GaN surface are needed. Among other questions, it is still unknown whether the annealing step actually heals crystal defects or simply allows them to diffuse away from the surface. We also note that the need for high temperature repair steps such as this would considerably restrict the freedom in device design since indium containing alloys would likely be unable to survive the anneal.
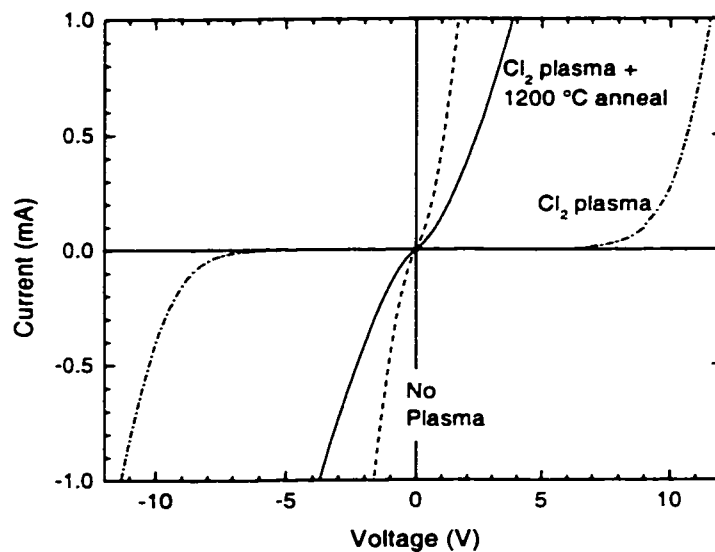

Figure 3.14 I-V characteristics obtained on a sample damaged with a Cl_2 etch (dash-dot line), and a sample damaged in the same etch and subsequently annealed for 15 seconds at 1200 °C (solid line). The I-V characteristics of an undamaged sample are shown for comparison (dashed line).

In summary, we have investigated the effects of plasma damage on contacts to p-type GaN. This material is extremely sensitive to plasma damage, and all the plasma exposure conditions investigated lead to Schottky-type contacts. Very high temperature anneals appear to be a promising technique for reducing the plasma-induced damage in this material. Further research should also focus on testing various approaches to cleaning up the physically damaged layers using wet etchants.[64,67,68]

Another solution to the etching difficulties may be the use of photo-electrochemical etching techniques. Using KOH and UV light, this technique has demonstrated reasonable etch rates and high selectivity between n-type and p-type GaN.[69,70] The properties of contacts on etched p-type GaN surfaces prepared in this way have not yet been tested, but the degradation may be minimal since little physical damage is expected. Some work will be required, however, to scale up this experimental technique to the point where it may be used routinely as a processing tool.

3.5 References

1   H. Amano, M. Kito, K. Hiramatsu, and I. Akasaki, "P-type conduction in Mg-doped GaN treated with low-energy electron beam irradiation (LEEBI)." *Jpn. J. Appl. Phys.* **28**, L2112-4 (1989).

2   S. Nakamura, M. Senoh, and T. Mukai, "Highly p-typed Mg-doped GaN films grown with GaN buffer layers." *Jpn. J. Appl. Phys.* **30**, L1708-11 (1991).

3   S. Nakamura, T. Mukai, M. Senoh, and N. Iwasa, "Thermal annealing effects on p-type Mg-doped GaN films." *Jpn. J. Appl. Phys.* **31**, L139-42 (1992).

4   S. Nakamura, N. Iwasa, M. Senoh, and T. Mukai, "Hole compensation mechanism of p-type GaN films." *Jpn. J. Appl. Phys.* **31**, 1258-66 (1992).

5   J. A. Van Vechten, J. D. Zook, R. D. Horning, and B. Goldenberg, "Defeating compensation in wide gap semiconductors by growing in H that is removed by low temperature de-ionizing radiation." *Jpn. J. Appl. Phys.* **31**, 3662-3 (1992).

6   J. Neugebauer and C. G. Van de Walle, "Role of hydrogen in doping of GaN." *Appl. Phys. Lett.* **68**, 1829-31 (1996).

7   N. M. Johnson, W. Gotz, J. Neugebauer, and C. G. Van de Walle, "Hydrogen in GaN." *Mat. Res. Soc. Symp. Proc.* **395**, 723-32 (1996).

8   C. R. Abernathy, S. J. Pearton, J. D. MacKenzie, J. W. Lee, C. B. Vartuli, R. G. Wilson, R. J. Shul, J. C. Zolper, and J. M. Zavada, "Role of C, O and H in III-V nitrides." *Mat. Res. Soc. Symp. Proc.* **395**, 685-90 (1996).

9   A. Bosin, V. Fiorentini, and D. Vanderbilt, "Hydrogen, acceptors, and H-acceptor complexes in GaN." *Mat. Res. Soc. Symp. Proc.* **395**, 503-8 (1996).

10   V. J. B. Torres, S. Oberg, and R. Jones, "Theoretical studies of hydrogen passivated substitutional magnesium acceptor in wurzite GaN." *MRS Internet J. Nitride Semicond. Res.* **2**, 35 (1997).

11   F. A. Reboredo and S. T. Pantelides, "Novel defect complexes and their role in the p-type doping of GaN." *Phys. Rev. Lett.* **82**, 1887-90 (1999).

12   T. Tanaka, A. Watanabe, H. Amano, Y. Kobayashi, I. Akasaki, S. Yamazaki, and M. Koike, "p-type conduction in Mg-doped GaN and $Al_{0.08}Ga_{0.92}N$ grown by metalorganic vapor phase epitaxy." *Appl. Phys. Lett.* **65**, 593-594 (1994).

13   S. Fujita, M. Funato, P. Doo-Cheol, and Y. Ikenaga, "Electrical characterization of MOVPE-grown p-type GaN:Mg against annealing temperature." *MRS Internet J. Nitride Semicond. Res.* **4S1** (1999).

14   C. J. Eiting, P. A. Grudowski, J. Park, D. J. H. Lambert, B. S. Shelton, and R. D. Dupuis, "Characteristics of Mg-doped GaN grown by metallorganic chemical vapor deposition." *J. Electrochem. Soc.* **144**, L219-21 (1997).

15   W. Gotz, N. M. Johnson, J. Walker, D. P. Bour, H. Amano, and I. Akasaki, "Hydrogen passivation of Mg acceptors in GaN grown by metalorganic chemical vapor deposition." *Appl. Phys. Lett.* **67**, 2666-8 (1995).

16   W. Gotz, N. M. Johnson, J. Walker, D. P. Bour, and R. A. Street, "Activation of acceptors in Mg-doped GaN grown by metalorganic chemical vapor deposition." *Appl. Phys. Lett.* **68**, 667-9 (1996).

17   H. Harima, T. Inoue, S. Nakashima, K. Furukawa, and M. Taneya, "Electronic properties in p-type GaN studied by Raman scattering." *Appl. Phys. Lett.* **73**, 2000-2 (1998).

18   Y. Li, Y. Lu, H. Shen, M. Wraback, C. Y. Hwang, M. Schurman, W. Mayo, T. Salagaj, and R. A. Stall, "Photoluminescence and SIMS studies of hydrogen passivation of Mg-doped p-type gallium nitride." *Mat. Res. Soc. Symp. Proc.* **395**, 369-74 (1996).

19   H. Lu and I. Bhat, "Magnesium doping of GaN by metalorganic chemical vapor deposition." *Mat. Res. Soc. Symp. Proc.* **395**, 497-502 (1996).

20   M. S. Brandt, N. M. Johnson, R. J. Molnar, R. Singh, and T. D. Moustakas, "Hydrogenation of p-type gallium nitride." *Appl. Phys. Lett.* **64**, 2264-6 (1994).

21   Y. Kamiura, Y. Yamashita, and S. Nakamura, "Photo-enhanced activation of hydrogen-passivated magnesium in p-type GaN films." *Jpn. J. Appl. Phys.* **37**, L970-1 (1998).

22   S. J. Pearton, J. W. Lee, and C. Yuan, "Minority-carrier-enhanced reactivation of hydrogen-passivated Mg in GaN." *Appl. Phys. Lett.* **68**, 2690-2 (1996).

23 M. Miyachi, T. Tanaka, Y. Kimura, and H. Ota, "The activation of Mg in GaN by annealing with minority-carrier injection." *Appl. Phys. Lett.* **72**, 1101-3 (1998).

24 D.-H. Youn, M. Lachab, M. Hao, T. Sugahara, H. Takenaka, Y. Naoi, and S. Sakai, "Investigation on the p-type activation mechanism in Mg-doped GaN films grown by metalorganic chemical vapor deposition." *Jpn. J. Appl. Phys.* **38**, 631-4 (1999).

25 S. J. Pearton, S. Bendi, K. S. Jones, V. Krishnamoorthy, R. G. Wilson, F. Ren, R. F. Karlicek, Jr., and R. A. Stall, "Reactivation of acceptors and trapping of hydrogen in GaN/InGaN double heterostructures." *Mat. Res. Soc. Symp. Proc.* **449**, 993-8 (1997).

26 L. L. Smith, S. W. King, R. J. Nemanich, and R. F. Davis, "Cleaning of GaN surfaces." *J. Electron. Mater.* **25**, 805-810 (1996).

27 S. W. King, J. P. Barnak, M. D. Bremser, K. M. Tracy, C. Ronning, R. F. Davis, and R. J. Nemanich, "Cleaning of AlN and GaN surfaces." *J. Appl. Phys.* **84**, 5248-60 (1998).

28 K. Prabhakaran, T. G. Andersson, and K. Nozawa, "Nature of native oxide on GaN surface and its reaction with Al." *Appl. Phys. Lett.* **69**, 3212-14 (1996).

29 J.-L. Lee, J. K. Kim, J. W. Lee, Y. J. Park, and T. Kim, "Effect of surface treatment by KOH solution on ohmic contact formation of p-type GaN." *Solid-St. Electron.* **43**, 435-8 (1999).

30 J.-L. Lee, M. Weber, J. K. Kim, J. W. Lee, Y. J. Park, T. Kim, and K. Lynn, "Ohmic contact formation mechanism of nonalloyed Pd contacts to p-type GaN observed by positron annihilation spectroscopy." *Appl. Phys. Lett.* **74**, 2289-91 (1999).

31 S. J. Pearton, C. R. Abernathy, C. B. Vartuli, J. W. Lee, J. D. MacKenzie, R. G. Wilson, R. J. Shul, F. Ren, and J. M. Zavada, "Unintentional hydrogenation of GaN and related alloys during processing." *J. Vac. Sci. Technol. A* **14**, 831-5 (1996).

32 J. T. Trexler, S. J. Miller, P. H. Holloway, and M. A. Khan, "Interfacial reactions between metal thin films and p-GaN." *Mat. Res. Soc. Symp. Proc.* **395**, 819-24 (1996).

33 L. L. Smith, R. F. Davis, M. J. Kim, R. W. Carpenter, and Y. Huang, "Microstructure, electrical properties, and thermal stability of Au-based ohmic contacts to p-GaN." *J. Mater. Res.* **12**, 2249-54 (1997).

34 J. T. Trexler, S. J. Pearton, P. H. Holloway, M. G. Mier, K. R. Evans, and R. F. Karlicek, "Comparison of Ni/Au, Pd/Au, and Cr/Au metallizations for ohmic contacts to p-GaN." *Mat. Res. Soc. Symp. Proc.* **449**, 1091-6 (1997).

35 J. K. Sheu, Y. K. Su, G. C. Chia, P. L. Koh, M. J. Jou, C. M. Chang, C. C. Liu, and W. C. Hung, "High-transparency Ni/Au ohmic contact to p-type GaN." *Appl. Phys. Lett.* **74**, 2340-2 (1999).

36 J. K. Kim, J.-L. Lee, J. W. Lee, H. E. Shin, Y. J. Park, and T. Kim, "Low resistance Pd/Au ohmic contacts to p-type GaN using surface treatment." *Appl. Phys. Lett.* **73**, 2953-5 (1998).

37 D. J. King, L. Zhang, J. C. Ramer, S. D. Hersee, and L. F. Lester, "Temperature behavior of Pt/Au ohmic contacts to p-GaN." *Mat. Res. Soc. Symp. Proc.* **468**, 421-6 (1997).

38 T. Kim, M. C. Yoo, and T. Kim, "Cr/Ni/Au ohmic contacts to the moderately doped p- and n-GaN." *Mat. Res. Soc. Symp. Proc.* **449**, 1061-5 (1997).

39   J. Ja-Soon, P. Kyung-Hyun, J. Hong-Kyu, K. Hyo-Gun, and P. Seong-Ju, "Ohmic contacts to p-type GaN using a Ni/Pt/Au metallization scheme." *J. Vac. Sci. Technol. B* **16**, 3105-7 (1998).

40   E. Kaminska, A. Piotrowska, A. Barcz, M. Guziewicz, S. Kasjaniuk, M. D. Bremser, R. F. Davis, E. Dynowska, and S. Kwiatkowski, "Ni/Si-based ohmic contacts to p- and n-type GaN." *Mat. Res. Soc. Symp. Proc.* **482**, 1077-82 (1998).

41   M. Suzuki, T. Kawakami, T. Arai, S. Kobayashi, Y. Koide, T. Uemura, N. Shibata, and M. Murakami, "Low-resistance Ta/Ti Ohmic contacts for p-type GaN." *Appl. Phys. Lett.* **74**, 275-7 (1999).

42   M. Suzuki, T. Arai, T. Kawakami, S. Kobayashi, S. Fujita, Y. Koide, Y. Taga, and M. Murakami, "Formation and deterioration mechanisms of low-resistance TaTi ohmic contacts for p-GaN." *J. Appl. Phys.* **86**, 5079-84 (1999).

43   X. A. Cao, S. J. Pearton, F. Ren, and J. R. Lothian, "Thermal stability of W and WSi_x contacts on p-GaN." *Appl. Phys. Lett.* **73**, 942-4 (1998).

44   D. B. Ingerly, Y. A. Chang, and Y. Chen, "NiIn as an ohmic contact to p-GaN." *MRS Internet J. Nitride Semicond. Res.* **4S1** (1999).

45   D. B. Ingerly, Y. A. Chang, and Y. Chen, "The electrical behavior of Pt_3In_7 and NiIn contacts to p-GaN." *Appl. Phys. Lett.* **74**, 2480-2 (1999).

46   T. Margalith, O. Buchinsky, D. A. Cohen, A. C. Abare, M. Hansen, S. P. DenBaars, and L. A. Coldren, "Indium tin oxide contacts to gallium nitride optoelectronic devices." *Appl. Phys. Lett.* **74**, 3930-2 (1999).

47   Y. Koide, T. Maeda, T. Kawakami, S. Fujita, T. Uemura, N. Shibata, and M. Murakami, "Effects of annealing in an oxygen ambient on electrical properties of ohmic contacts to p-type GaN." *J. Electron. Mater.* **28**, 341-6 (1999).

48   L.-C. Chen, F.-R. Chen, J.-J. Kai, L. Chang, J.-K. Ho, C.-S. Jong, C. C. Chiu, C.-N. Huang, C.-Y. Chen, and K.-K. Shih, "Microstructural investigation of oxidized Ni/Au ohmic contact to p-type GaN." *J. Appl. Phys.* **86**, 3826-3832 (1999).

49   J.-K. Ho, C.-S. Jong, C. C. Chiu, C.-N. Huang, K.-K. Shih, L.-C. Chen, F.-R. Chen, and J.-J. Kai, "Low-resistance ohmic contacts to p-type GaN achieved by the oxidation of Ni/Au films." *J. Appl. Phys.* **86**, 4491-7 (1999).

50   S. J. Pearton, J. C. Zolper, R. J. Shul, and F. Ren, "GaN: processing, defects, and devices." *J. Appl. Phys.* **86**, 1-78 (1999).

51   A. T. Ping, A. C. Schmitz, I. Adesida, M. A. Khan, Q. Chen, and J. W. Yang, "Characterization of reactive ion etching-induced damage to n-GaN surfaces using Schottky diodes." *J. Electron. Mater.* **26**, 266-71 (1997).

52   A. T. Ping, Q. Chen, J. W. Yang, A. M. Asif Khan, and I. Adesida, "The effects of reactive ion etching-induced damage on the characteristics of ohmic contacts to n-type GaN." *J. Electron. Mater.* **27**, 261-5 (1998).

53   J. Y. Chen, C. J. Pan, and G. C. Chi, "Electrical and optical changes in the near surface of reactively ion etched n-GaN." *Solid-St. Electron.* **43**, 649-52 (1999).

54 C. R. Eddy, Jr. and B. Molnar, "Plasma etch-induced conduction changes in gallium nitride." *J. Electron. Mater.* **28**, 314-18 (1999).

55 X. A. Cao, A. P. Zhang, D. T. Dang, H. Cho, S. J. Pearton, R. J. Shul, L. Zhang, J. R. Hickman, and J. M. van Hove, "Inductively coupled plasma damage in GaN Schottky diodes." *J. Vac. Sci. Technol. B* **17**, 1540-4 (1999).

56 X. A. Cao, H. Cho, S. J. Pearton, G. T. Dang, A. P. Zhang, F. Ren, R. J. Shul, L. Zhang, R. Hickman, and J. M. Van Hove, "Depth and thermal stability of dry etch damage in GaN Schottky diodes." *Appl. Phys. Lett.* **75**, 232-4 (1999).

57 R. J. Shul, L. Zhang, A. G. Baca, C. G. Willison, J. Han, S. J. Pearton, F. Ren, J. C. Zolper, and L. F. Lester, "High-density plasma-induced etch damage of GaN." *Mat. Res. Soc. Symp. Proc.* **573**, 271-280 (1999).

58 X. A. Cao, S. J. Pearton, A. P. Zhang, G. T. Dang, F. Ren, R. J. Shul, L. Zhang, R. Hickman, and J. M. V. Hove, "Electrical effects of plasma damage in p-GaN." *Appl. Phys. Lett.* **75**, 2569-71 (1999).

59 L. S. McCarthy, P. Kozodoy, M. J. W. Rodwell, S. P. DenBaars, and U. K. Mishra, "AlGaN/GaN heterojunction bipolar transistor." *IEEE Electron Device Lett.* **20**, 277-9 (1999).

60 R. Fan, C. R. Abernathy, J. M. Van Hove, P. P. Chow, R. Hickman, J. J. Klaasen, R. F. Kopf, C. Hyun, K. B. Jung, J. R. La Roche, G. Wilson, J. Han, R. J. Shul, A. G. Baca, and S. J. Pearton, "300 degrees C GaN/AlGaN heterojunction bipolar transistor." *MRS Internet J. Nitride Semicond. Res.* **3**, 41 (1998).

61 S. Yoshida and J. Suzuki, "High-temperature reliability of GaN metal semiconductor field-effect transistor and bipolar junction transistor." *J. Appl. Phys.* **85**, 7931-4 (1999).

62 Z. Fan, S. N. Mohammad, W. Kim, O. Aktas, A. E. Botchkarev, and H. Morkoc, "Very low resistance multilayer ohmic contact to n-GaN." *Appl. Phys. Lett.* **68**, 1672-4 (1996).

63 C.-H. Chen, S. Keller, E. D. Haberer, L. Zhang, S. P. DenBaars, E. L. Hu, U. K. Mishra, and Y. Wu, "Cl$_2$ reactive ion etching for gate recessing of AlGaN/GaN field-effect transistors." *J. Vac. Sci. Technol. B* **17**, 2755-8 (1999).

64 B. J. Kim, J. W. Lee, H. S. Park, Y. Park, and T. I. Kim, "Wet etching of (0001) GaN/Al$_2$O$_3$ grown by MOVPE." *J. Electron. Mater.* **27**, L32-4 (1998).

65 J. C. Zolper, D. J. Rieger, A. G. Baca, S. J. Pearton, J. W. Lee, and R. A. Stall, "Sputtered AlN encapsulant for high-temperature annealing of GaN." *Appl. Phys. Lett.* **69**, 538-40 (1996).

66 X. A. Cao, S. J. Pearton, R. K. Singh, C. R. Abernathy, J. Han, R. J. Shul, D. J. Rieger, J. C. Zolper, R. G. Wilson, M. Fu, J. A. Sekhar, H. J. Guo, and S. J. Pennycook, "Rapid thermal processing of implanted GaN up to 1500 degrees C." *MRS Internet J. Nitride Semicond. Res.* **4S1**, G6.33 (1999).

67 N. V. Edwards, M. D. Bremser, T. W. Weeks, Jr., R. S. Kern, R. F. Davis, and D. E. Aspnes, "Real-time assessment of overlayer removal on GaN, AlN and AlGaN surfaces using spectroscopic ellipsometry." *Appl. Phys. Lett.* **69**, 2065-7 (1996).

68 D. A. Stocker, E. F. Schubert, and J. M. Redwing, "Crystallographic wet chemical etching of GaN." *Appl. Phys. Lett.* **73**, 2654-6 (1998).

69 M. S. Minsky, A. M. White, and E. L. Hu, "Room-temperature photoenhanced wet etching of GaN." *Appl. Phys. Lett.* **68**, 1531-3 (1996).

70 C. Youtsey, G. Bulman, and I. Adesida, "Dopant-selective photoenhanced wet etching of GaN." *J. Electron. Mater.* **27**, 282-7 (1998).

Chapter 4

GaN *p-n* junction diodes

4.1 Introduction

The GaN *p-n* diode is a fundamental building block for a variety of electronic and optoelectronic device structures. The first such diode was achieved by Amano, et al., who reported a sharper turn-on in the I-V characteristics for these diodes than for m-i-n devices.[1] Most of the published work on GaN *p-n* diodes has focused on optoelectronic device applications. As a result, the characterization has emphasized electroluminescence measurements and the forward bias "turn-on" voltage. The latter is largely dependent on *p*-contact quality and does not provide useful electrical data on the nature of the diode itself.

In forward-bias operation, the electrical characteristics of a junction are usually characterized by an ideality factor *n*. The factor is derived by fitting the I-V characteristics to the diode equation:

$$J = J_S \left[\exp\left(\frac{qV}{n\,kT}\right) - 1 \right],$$

(4.1)

where J_S is the saturation current and V is the applied voltage. However, the I-V characteristics of GaN *p-n* diodes often do not fit the diode equation very well, or exhibit high values of the ideality factor, which makes physical interpretation difficult. Fedison, et al. have investigated the forward-current mechanism in GaN diodes and find three regimes are present in some devices: a tunneling current appears to dominate at low bias, at intermediate bias the current fits the diode equation with $n \approx 1.5$, and at higher bias the current exhibits an ideality of $n \approx 7$.[2] The authors attribute the tunneling current to a trap state within the gap, and the

large ideality factor at higher bias to space-charge limited current due to single-carrier injection. While these explanations are speculative, it is clear that the diode behavior deviates significantly from the ideal case. Trap levels within the gap will reduce the radiative efficiency of optoelectronic devices, as well as the injection efficiency in bipolar transistors.

In reverse-bias, the important diode figures-of-merit are leakage current and breakdown voltage. The breakdown behavior of GaN p-n diodes has been examined both theoretically[3] and experimentally.[4,5] Breakdown voltages up to ~150 V are reported, consistent with a breakdown field of approximately 2 MV/cm. The leakage current in GaN due to minority carrier diffusion should be extremely small because of the very wide band-gap. Much higher leakage currents are normally obtained, indicating the presence of trap states within the gap. The resulting leakage paths may adversely impact the performance of both photodiodes and bipolar transistors; the trap states may also act as recombination centers in forward-bias operation. For improved device operation, it is clearly important to identify and eliminate the defects which are responsible for the various trap states.
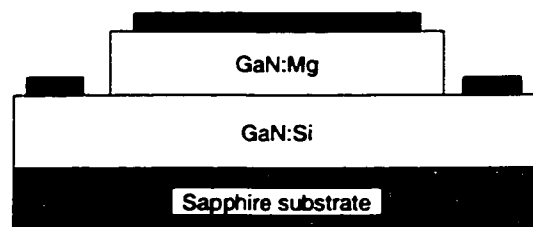

Figure 4.1 Diagram of GaN _p-n_ junction diodes.

4.2 Standard GaN p-n diodes

GaN *p-n* diodes were created by growing a Mg-doped layer above a Si-doped *n*-type layer. After activation and *p*-contact deposition, a Cl_2 reactive ion etch step was employed to reveal the *n*-type layer. Ti/Al contacts were used on the *n*-type layer, while the standard Pd/Au process was employed for *p*-contacts. Figure 4.1 shows a diagram of the GaN *p-n* diodes.

A typical I-V characteristic is shown in figure 4.2 on a linear scale. The diodes exhibit a sharp "turn-on" at a voltage near band-gap. The reverse-bias breakdown behavior is quite soft, and occurs at voltages up to ~ 100V depending on the doping level in the *n*-type layer. The breakdown voltage is obviously of great importance for developing high-power bipolar transistors. Figure 4.3 shows the maximum base-collector breakdown voltage measured on a number of bipolar transistors produced with varying thickness of the unintentionally-doped collector layer (these transistors were processed and tested by Lee McCarthy at UCSB). As
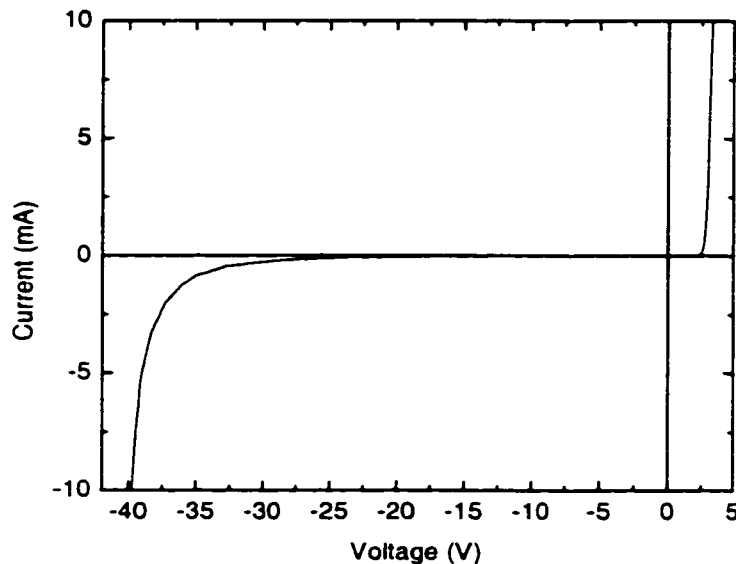

Figure 4.2 I-V Characteristic of a typical GaN *p-n* junction.

expected, the breakdown voltage increases with the collector thickness, reaching 160 V for a 1.3 μm thick collector.

Figure 4.4 shows the I-V characteristics of three devices of different sizes, plotted in a log-linear manner. The forward-bias characteristics of these devices all yield $n \sim 4$. On other devices, ideality factors between 3 and 8 have been measured. The origin of these high ideality factors is not fully understood at this time, but the presence of mid-gap states may well be a contributing factor. Detailed analysis of temperature-dependent I-V characteristics are needed in order to investigate the current flow mechanism; ideally, these measurements should be performed on samples grown under a variety of growth conditions in order to determine which factors affect the parasitic current flow paths. Such measurements have not performed as part of this dissertation, but form an important topic for future work.
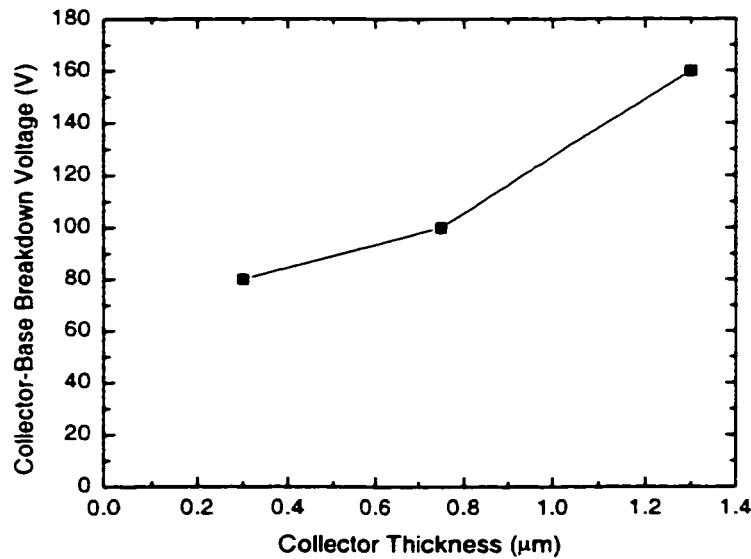

Figure 4.3   Maximum collector-base breakdown voltage measured on bipolar junction transistors as a function of collector thickness.

The I-V characteristics shown in figure 4.4 exhibit high, bias-dependent reverse leakage currents. The origin of these leakage currents is the subject of the next section.
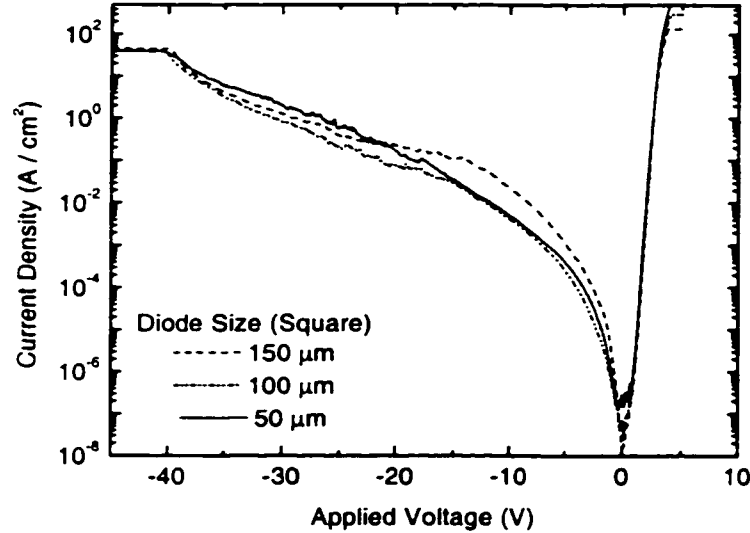

Figure 4.4 I-V characteristics of *p-n* diodes of various sizes. Each diode is a square; the length of a side of the square is indicated.

4.3 Effect of threading dislocations

GaN films grown on sapphire typically exhibit a high dislocation density; these threading dislocations (TDs) are likely to be electrically active and create states within the band-gap.[6] Such states may be responsible for the high reverse-bias leakage currents observed. Indeed, a correlation between dark current and dislocation density has been reported in various materials systems including Si,[7] SiGe,[8] and HgCdTe,[9] and has been proposed for GaN diodes.[10] In order to investigate this hypothesis, we used lateral epitaxial overgrowth (LEO) to fabricate GaN *p-n* diodes both with and without threading dislocations.

LEO of GaN has attracted considerable attention[11-13] as a method for reducing the high TD density which has historically limited device performance in the nitride system. In this technique, standard dislocated GaN layers are partially masked and then re-grown upon. GaN grown vertically through the mask openings (windows) retains a high TD density; however material which then grows laterally across the mask has a drastically reduced TD density. For example, work in our laboratory has shown a reduction in TD density from $\sim 4\times10^8$ cm^{-2} in the window region to below 10^6 cm^{-2} in the LEO region.[14]

This reduction in dislocation density is expected to both improve device performance and facilitate investigation of the fundamental properties of GaN films. Indeed, the use of LEO GaN has already yielded improved lifetime for laser diodes,[15] and there are indications that it helps eliminate pathways for dopant diffusion.[16] Measurements of the reverse bias current density in a *p-n* junction should be a sensitive tool for monitoring the benefits of dislocation reduction.

The devices were fabricated as described in the process flow shown in figure 4.5. GaN films 2 μm thick were grown on *c*-plane sapphire substrates by MOCVD and subsequently patterned with an SiO$_2$ mask for LEO regrowth. The pattern consisted of stripes with mask openings 5 μm wide separated by 45 μm of SiO$_2$. In the LEO regrowth step GaN was grown vertically through the mask openings and laterally across the mask, creating bars whose height and overgrowth width were both approximately 8 μm. The SiO$_2$ mask was then removed in the region between the LEO bars. This step exposed GaN over the entire (corrugated) surface of the wafer, so that subsequent growth was not selective epitaxy but uniform deposition. We note that despite this precaution the highly non-planar surface morphology may have affected the thickness and doping uniformity of the GaN deposited in the later growth steps.

The sample was then returned to the MOCVD machine a final time and p-n junction layers were grown. The p-n junction consisted of 1 μm unintentionally doped n-type GaN followed by 0.5 μm Mg-doped p-type GaN. On standard planar films these growth conditions typically yield electron and hole
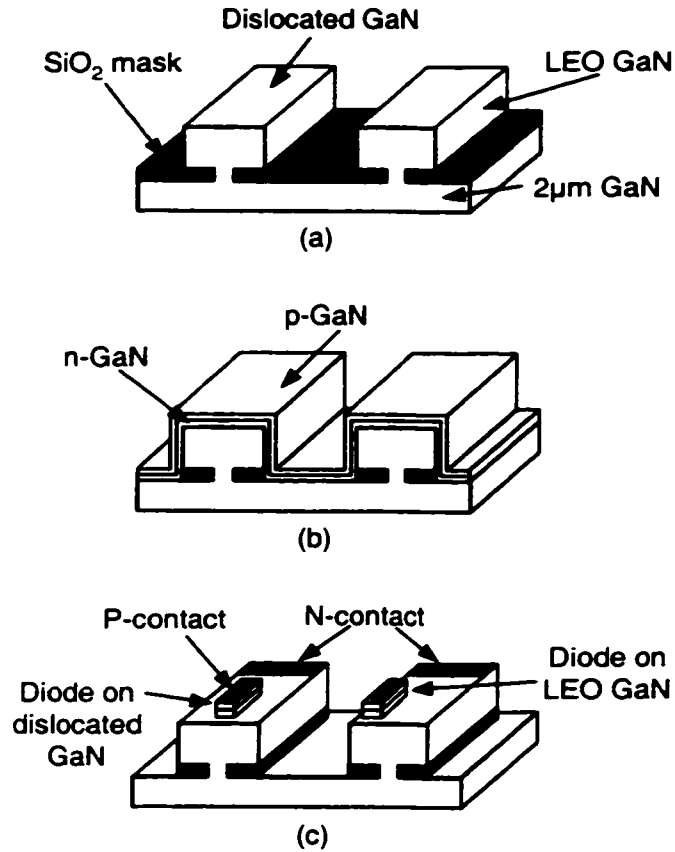

Figure 4.5 Process flow for diode growth and fabrication. Part (a): LEO growth. An SiO_2 mask is deposited on a GaN film and window stripes are opened to the GaN beneath. During regrowth dislocations propagate vertically—GaN above the window region remains dislocated while laterally grown (LEO) material has a reduced dislocation density. Part (b): SiO_2 mask is removed between the LEO bars and the p-n junction layers are grown. Part (c): Mesa is etched and metal contacts are deposited to form diode structures. Adjacent diodes lie on LEO GaN and on the window region.

103

concentrations of approximately 5×10^{16} cm^{-3} and 7×10^{17} cm^{-3}, respectively. Diode devices were fabricated on this sample using the standard activation and p-contact processes, followed by a mesa etch using Cl$_2$ RIE and the deposition of a Ti/Al n-contact on the etched surface. The devices had dimensions of 2 μm $\times$ 20 μm, and were placed so that they lay either on the LEO GaN or on the window region. In this way, p-n junction diodes were fabricated in close proximity on both the standard (highly dislocated) GaN in the window regions and on the low-dislocation density LEO GaN in the overgrown regions. The devices are sufficiently small that most of the diodes on LEO GaN contain no threading dislocations whatsoever; the devices on the window region are expected to contain approximately 200 threading dislocations on average. A photograph of the finished devices is shown in figure 4.6.
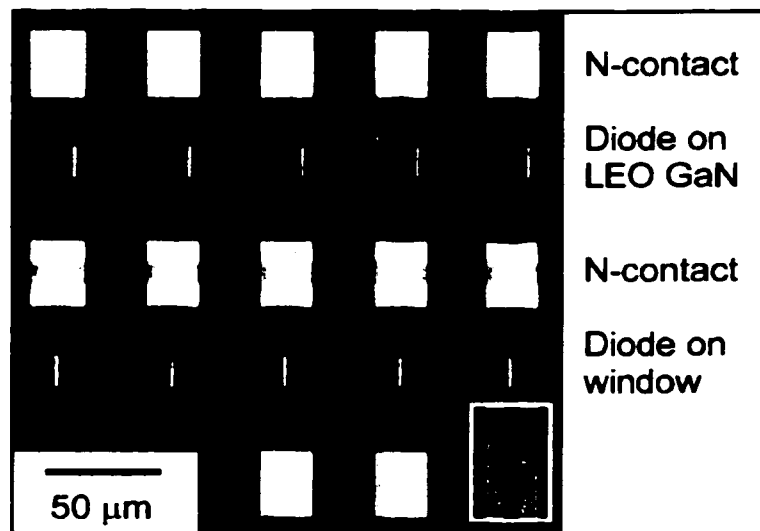

Figure 4.6 Photograph of the finished devices. The top row of diodes are on LEO GaN; those in the bottom row are on the window region (dislocated GaN). The inset (lower right) shows the position of the overgrown GaN and the window region.

104

The *p-n* junction diodes were characterized by current-voltage (I-V) measurements performed with a Hewlett-Packard 4145 semiconductor parameter analyzer. Extra care had to be employed in order to accurately measure the small leakage currents that were obtained at high reverse bias. Moisture that had accumulated on the sample surface provided a leakage path that obscured the sample current; this issue was addressed by baking the sample at 120°C prior to measurement. Another source of measurement error was leakage through the dielectric insulator used in the coaxial cables. In order to avoid incorrect results, the current flow measurement was performed on the grounded lead, where there was no potential difference between the inner and outer conductors of the coaxial cable. We believe that through the use of these precautionary steps, accurate measurements of the sample I-V characteristics were obtained.
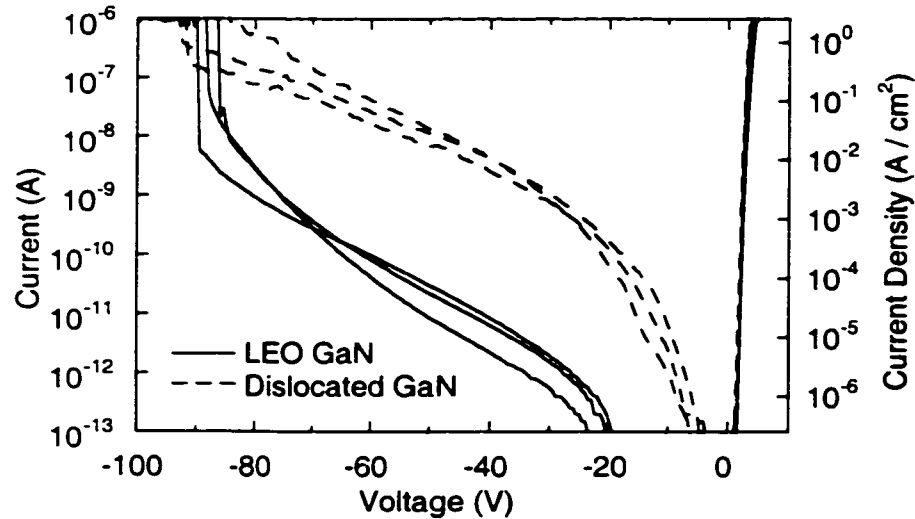

Figure 4.7 I-V characteristics for several diodes on LEO GaN and on the window region (dislocated GaN).

Figure 4.7 shows a comparison of the I-V characteristics for several devices of each type. A dramatic reduction in reverse bias current occurs on LEO GaN; for example the current density at a reverse bias of 25 V was approximately 9×10^{-4} A/cm^2 in the window region and 9×10^{-7} A/cm^2 on LEO GaN, a reduction of 3 orders of magnitude. This result clearly indicates that leakage current in standard (dislocated) GaN p-n junctions is dominated by defect levels associated with TDs, and that this leakage current can be greatly reduced by eliminating the dislocations. Below a reverse bias of approximately 20 V, the leakage current on LEO devices was below the measurement limit of 100 fA (corresponding to a current density below 2.5×10^{-7} A/cm^2). These very low dark current values have
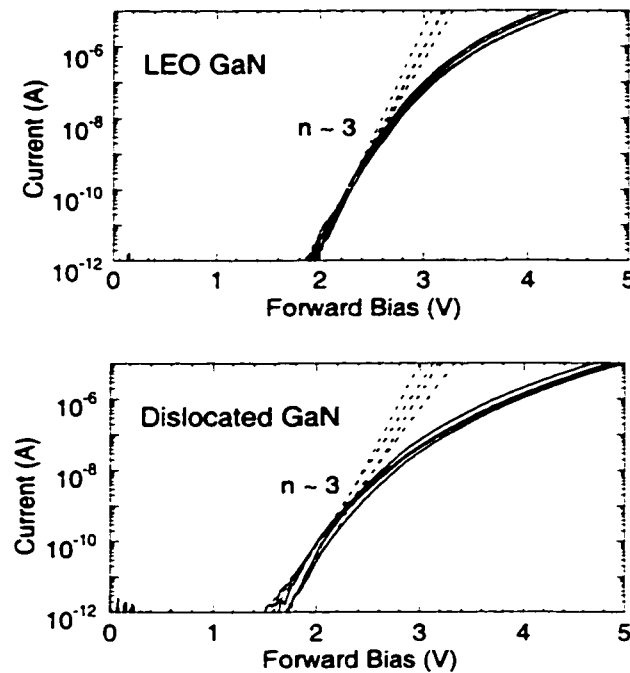

Figure 4.8 Forward-bias I-V characteristics of diodes on LEO GaN (top) and dislocated GaN (bottom). The dashed lines indicate fits to the diode equation (4.1).

106

The *p-n* junction diodes were characterized by current-voltage (I-V) measurements performed with a Hewlett-Packard 4145 semiconductor parameter analyzer. Extra care had to be employed in order to accurately measure the small leakage currents that were obtained at high reverse bias. Moisture that had accumulated on the sample surface provided a leakage path that obscured the sample current; this issue was addressed by baking the sample at 120°C prior to measurement. Another source of measurement error was leakage through the dielectric insulator used in the coaxial cables. In order to avoid incorrect results, the current flow measurement was performed on the grounded lead, where there was no potential difference between the inner and outer conductors of the coaxial cable. We believe that through the use of these precautionary steps, accurate measurements of the sample I-V characteristics were obtained.
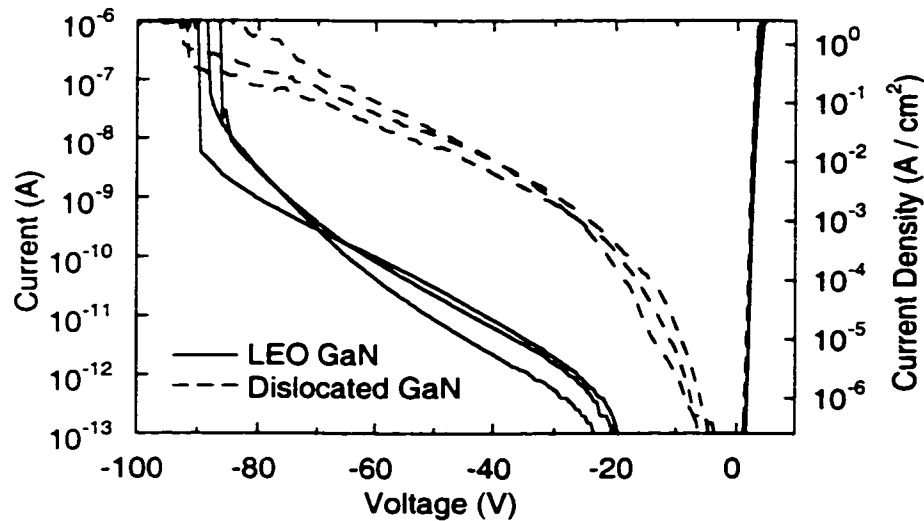

Figure 4.7 I-V characteristics for several diodes on LEO GaN and on the window region (dislocated GaN).

Figure 4.7 shows a comparison of the I-V characteristics for several devices of each type. A dramatic reduction in reverse bias current occurs on LEO GaN; for example the current density at a reverse bias of 25 V was approximately 9×10^{-4} A/cm^2 in the window region and 9×10^{-7} A/cm^2 on LEO GaN, a reduction of 3 orders of magnitude. This result clearly indicates that leakage current in standard (dislocated) GaN p-n junctions is dominated by defect levels associated with TDs, and that this leakage current can be greatly reduced by eliminating the dislocations. Below a reverse bias of approximately 20 V, the leakage current on LEO devices was below the measurement limit of 100 fA (corresponding to a current density below 2.5×10^{-7} A/cm^2). These very low dark current values have
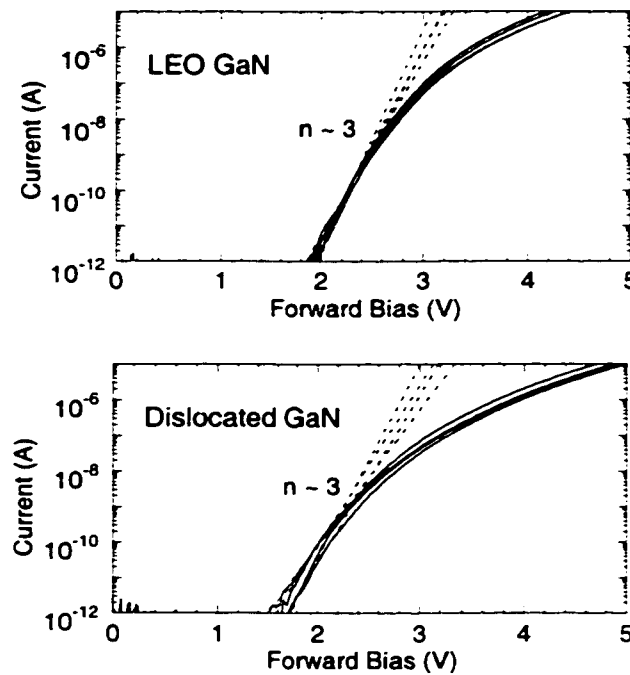

Figure 4.8 Forward-bias I-V characteristics of diodes on LEO GaN (top) and dislocated GaN (bottom). The dashed lines indicate fits to the diode equation (4.1).

recently been utilized by Parish, et al., to form solar-blind UV photodiodes with high responsivity using LEO GaN.[17]

Both types of diodes exhibit rectification and emit light under forward bias. The forward-bias characteristics of the two devices are very similar. As shown in figure 4.8, both types of devices yield ideality factors of $n \sim 3$, although in both cases the fit to equation (4.1) is quite poor. It is clear from these measurements that the mechanism responsible for the forward-bias leakage current (reflected in the high ideality factors) is not linked to the dislocations; the cause of this phenomenon is still unknown.

The diodes exhibit a sharp breakdown at a reverse bias between 70 and 90V. Although the exact doping densities are unknown, we estimate that this corresponds to a peak electric field of approximately 2×10^6 V/cm. This breakdown causes permanent damage to the diode—reverse leakage is significantly higher once the device has been brought past the breakdown point.
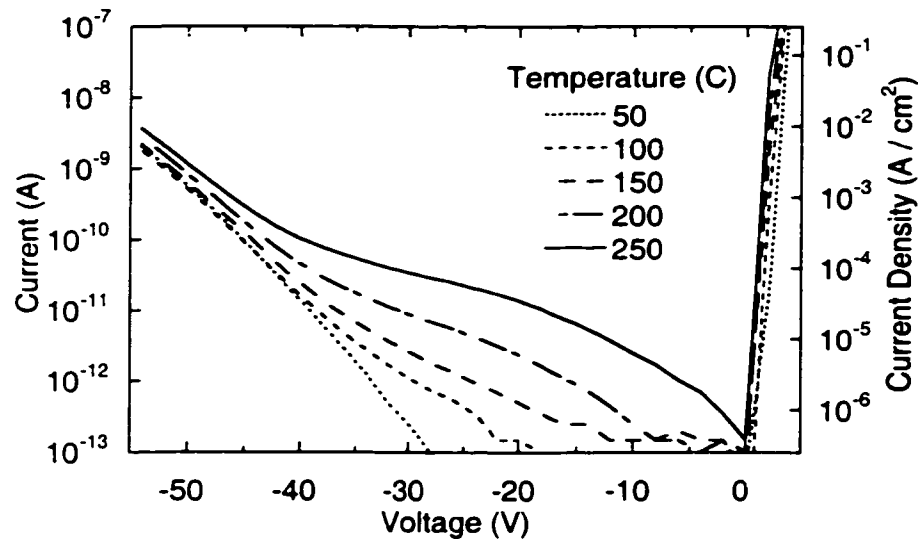

Figure 4.9 I-V characteristics of p-n junction diode on LEO GaN at various temperatures.

We note that even the diodes on LEO GaN exhibit much higher leakage currents than would be expected in an ideal GaN junction, indicating that some trap levels remain within the band-gap. These levels are most likely associated either with sidewall damage or with point defects. A study of leakage current as a function of area-to-perimeter ratio is needed to determine which effect dominates. Such a study has not been carried out and would be difficult due to the geometry of these samples. Nonetheless, an analysis of this leakage current is valuable as a first step toward characterizing the performance of GaN devices in the absence of dislocations.

The reverse-bias I-V characteristics of the diodes on LEO GaN were recorded as a function of temperature by placing the sample on a heated chuck during the measurements. The temperature-dependent data, presented in figure 4.9, show two regimes. At reverse bias greater than ~ 40V the current is strongly field-dependent but only weakly temperature-dependent, indicating that tunneling is likely the dominant transport mechanism. The current at low bias exhibits a much stronger temperature dependence and a weaker field dependence, suggesting that thermionic emission over a barrier dominates in this regime (at
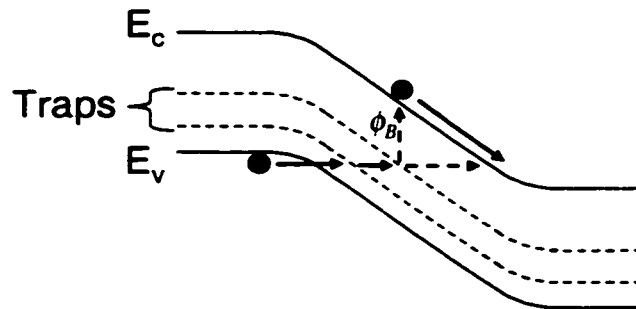

Figure 4.10 Possible band-diagram to explain reverse-bias current in LEO *p-n* junction. ϕ_B is the height of the barrier to thermionic emission from the trap level. At high bias, a tunneling current path dominates.

room temperature this thermionic current component is too small to be measured). This barrier most likely corresponds to emission from a deep trap level into the band. The increase in thermionic current with increasing bias is indicative of the Frenkel-Poole field-induced barrier lowering effect.[18] A possible band-diagram that could account for the observed behavior is shown in figure 4.10. As the field increases further, the barrier becomes so thin that tunneling current begins to dominate over thermionic emission.

Current measurements near zero bias, where the barrier lowering effect is small, are required in order to accurately determine the energy level of the trap.
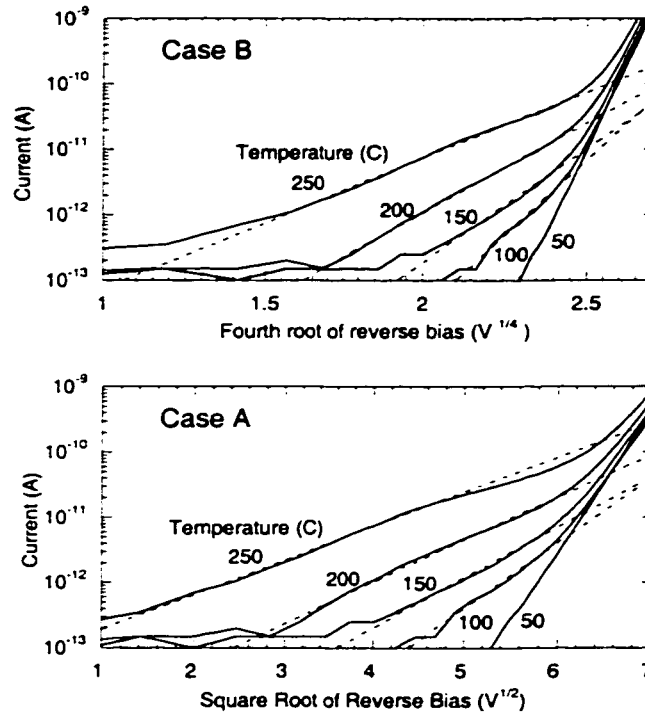

Figure 4.11 In these plots, the temperature-dependent data of figure 4.9 are fit to equation 4.2 (dashed lines). In the top plot, the electric field is assumed to vary as the square root of the applied bias, while in the bottom plot it is assumed to scale linearly with bias.

However, no data could be obtained in this bias range because the dark current was below the measurement sensitivity limit; instead we have extrapolated these values from the thermionic current component at higher bias. The standard Frenkel-Poole formula for field-induced barrier lowering is given by

$$I = I_0 \exp\left(\frac{a\sqrt{E}}{kT}\right),$$ (4.2)

$$I_0 \sim \exp\left(-\frac{\phi_B}{kT}\right),$$ (4.3)

where ϕ_B is the barrier height and E is the electric field (a is a constant). Because the electric field is not known, its value must be extracted from the applied voltage in the diode. If the electric field is constant across the depletion region (as
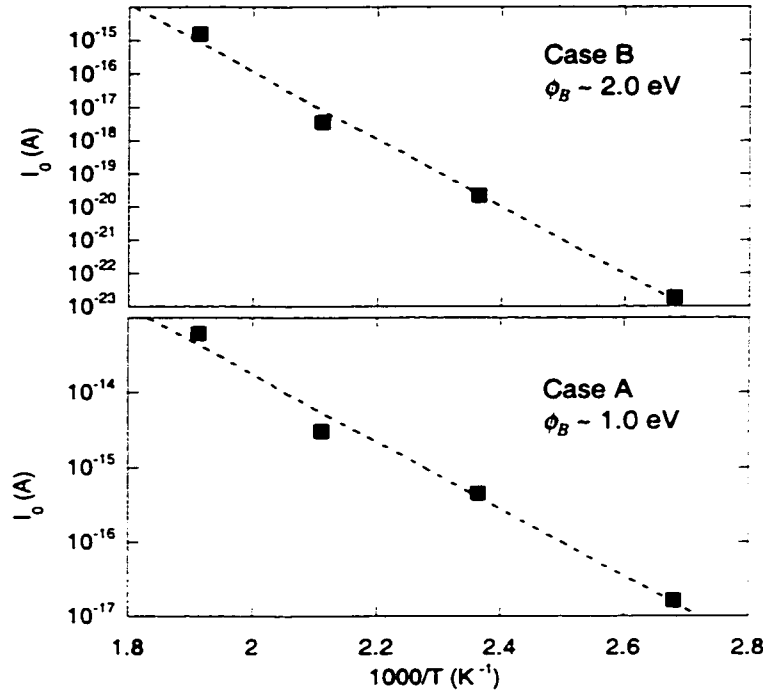

Figure 4.12 Barrier height extracted from the fitting results shown in figure 4.11.

110

in a p-i-n diode) so that current increases exponentially as $V^{1/2}$ (case A), a trap energy of 1.0 eV is calculated. If the electric field is assumed to decrease linearly with distance, as is the case for an abrupt junction with uniform doping, and if the trap emission is assumed to occur at the point of highest electric field, an energy of 2.0 eV is obtained. In this case, the current increases exponentially as $V^{1/4}$ (case B). These two extrapolations are shown in figure 4.11, and in figure 4.12 the resulting values of I_0 are analyzed to extrapolate the trap energy ϕ_B. The true trap energy is believed to lie somewhere between the two calculated values. We note that with this analysis it is not possible to extract the trap density or to distinguish between an electron trap and a hole trap.

In conclusion, the studies on LEO GaN have demonstrated that eliminating dislocations leads directly to improved electrical properties: reverse-bias leakage is reduced by over three orders of magnitude. No change in the ideality factor was observed. Temperature dependent measurements that have been performed on the dislocation-free diodes indicate that a deep trap limits device performance in the absence of dislocations.

4.4 References

1   H. Amano, M. Kito, K. Hiramatsu, and I. Akasaki, "P-type conduction in Mg-doped GaN treated with low-energy electron beam irradiation (LEEBI)." *Jpn. J. Appl. Phys.* **28**, L2112-4 (1989).

2   J. B. Fedison, T. P. Chow, H. Lu, and I. B. Bhat, "Electrical characteristics of magnesium-doped gallium nitride junction diodes." *Appl. Phys. Lett.* **72**, 2841-3 (1998).

3   M. Trivedi and K. Shenai, "Performance evaluation of high-power wide band-gap semiconductor rectifiers." *J. Appl. Phys.* **85**, 6889-97 (1999).

4   A. N. Kovalev, F. I. Manyakhin, V. E. Kudryashov, A. N. Turkin, and A. E. Yunovich, "Impact ionization luminescence of InGaN/AlGaN/GaN p-n-heterostructures." *Fiz. Tekh. Poluprovodn. (Russia)* **32**, 63-7 (1998).

5   V. A. Dmitriev, K. G. Irvine, C. H. Carter, Jr., N. I. Kuznetsov, and E. V. Kalinina, "Electric breakdown in GaN p-n junctions." *Appl. Phys. Lett.* **68**, 229-31 (1996).

6   N. G. Weimann, L. F. Eastman, D. Doppalapudi, H. M. Ng, and T. D. Moustakas, "Scattering of electrons at threading dislocations in GaN." *J. Appl. Phys.* **83**, 3656-9 (1998).

7   H. El-Ghitani and M. Pasquinelli, "Influence of dislocations on dark current of multicrystalline silicon N+ P junction." *J. Phys. III (France)* **3**, 1931-9 (1993).

8   F. M. Ross, R. Hull, D. Bahnck, J. C. Bean, L. J. Peticolas, and C. A. King, "Changes in electrical device characteristics during the in situ formation of dislocations." *Appl. Phys. Lett.* **62**, 1426-8 (1993).

9   R. S. List, "Electrical effects of dislocations and other crystallographic defects in $Hg_{0.78}Cd_{0.22}Te$ n-on-p photodiodes." *J. Electron. Mater.* **22**, 1017-25 (1993).

10 D. V. Kuksenkov, H. Temkin, A. Osinsky, R. Gaska, and M. A. Khan, "Low-frequency noise and performance of GaN p-n junction photodetectors." *J. Appl. Phys.* **83**, 2142-6 (1998).

11 D. Kapolnek, S. Keller, R. Vetury, R. D. Underwood, P. Kozodoy, S. P. Den Baars, and U. K. Mishra, "Anisotropic epitaxial lateral growth in GaN selective area epitaxy." *Appl. Phys. Lett.* **71**, 1204-6 (1997).

12 A. Usui, H. Sunakawa, A. Sakai, and A. A. Yamaguchi, "Thick GaN epitaxial growth with low dislocation density by hydride vapor phase epitaxy." *Jpn. J. Appl. Phys.* **36**, L899-902 (1997).

13 T. S. Zheleva, N. Ok-Hyun, M. D. Bremser, and R. F. Davis, "Dislocation density reduction via lateral epitaxy in selectively grown GaN structures." *Appl. Phys. Lett.* **71**, 2472-4 (1997).

14 H. Marchand, J. P. Ibbetson, P. T. Fini, P. Kozodoy, S. Keller, S. DenBaars, J. S. Speck, and U. K. Mishra, "Atomic force microscopy observation of threading dislocation density reduction in lateral epitaxial overgrowth of gallium nitride by MOCVD." *MRS Internet J. Nitride Semicond. Res.* **3** (1998).

15 S. Nakamura, M. Senoh, S. I. Nagahama, N. Iwasa, T. Yamada, T. Matsushita, H. Kiyoku, Y. Sugimoto, T. Kozaki, H. Umemoto, M. Sano, and K. Chocho, "InGaN/GaN/AlGaN-based laser diodes with modulation-doped strained-layer superlattices grown on an epitaxially laterally overgrown GaN substrate." *Appl. Phys. Lett.* **72**, 211-13 (1998).

16 N. Kuroda, C. Sasaoka, A. Kimura, A. Usui, and Y. Mochizuki, "Precise control of pn-junction profiles for GaN-based LD structures using GaN substrates with low dislocation densities." *J. Cryst. Growth* **189-190**, 551-5 (1998).

17 G. Parish, S. Keller, P. Kozodoy, J. P. Ibbetson, H. Marchand, P. T. Fini, S. B. Fleischer, S. P. DenBaars, U. K. Mishra, and E. J. Tarsa, "High-performance (Al,Ga)N-based solar-blind ultraviolet p-i-n detectors on laterally epitaxially overgrown GaN." *Appl. Phys. Lett.* **75**, 247-9 (1999).

18 J. Frenkel, "On pre-breakdown phenomena in insulators and electronic semi-conductors." *Phys. Rev.* **54**, 647-8 (1938).

Chapter 5

Depletion region effects in Mg-doped GaN

5.1 Introduction

There is increasing research into the use of many wide band-gap semiconductors, including GaN, for both electronic and optoelectronic devices.[1] As discussed in chapter 1, progress in many of these materials has been handicapped by the lack of shallow dopants of one or both types and the consequent difficulty in obtaining high carrier concentrations. The deep nature of the dopants will also have implications for the high-frequency behavior of depletion regions in these materials. In this chapter we discuss the dynamics of depletion regions involving deep dopants, with a particular focus on the Mg acceptor in GaN. The results, however, are quite general and should be equally applicable to other wide band-gap semiconductors.

When shallow dopants are used, the dopant atoms are always ionized and space-charge modulation is provided only through the presence or absence of mobile carriers. Thus the depletion region edge necessarily represents both the carrier edge and the space-charge edge. Deep dopants, in contrast, have a changing ionization state: they are only partially ionized in the bulk, but band-bending causes full ionization in the depletion region. Rapid modulation of the depletion region will require the acceptors to change ionization state, a process with a finite time constant.

There are a number of important consequences of these facts. First we note that in the presence of heavy doping (as typically applied in Mg-doped GaN), the DC depletion region widths are expected to be very thin despite the low

carrier concentration in the bulk. Secondly, there exists a transition region at the depletion region edge that separates the ionized acceptor profile from the free carrier profile. Finally, we must address the dispersion phenomena that result from the finite capture and emission times of the deep acceptor. In large-signal measurements the effect will be severe: because only the mobile holes can respond, depletion regions will extend much farther at high-frequency than they will in the low-frequency case. The small-signal dispersion is a more subtle effect, and may be used as a tool to probe the form of the DC depletion region. The small-signal dispersion has been analyzed in the cases of Au-doped silicon,[2,3] B-doped diamond,[4] and the Si DX center in AlGaAs,[5] and some recent work has been published for the case of Mg-doped GaN.[6-8]

In section 5.2, the effect of large-signal dispersion on the performance of GaN-based BJTs is briefly addressed. The discussion is minimal as experimental data on this effect are not yet available and detailed calculations of the large-signal dispersion are beyond the scope of this work. The small-signal dispersion, however, is amenable both to analytical calculation and experimental measurement. This effect is discussed in section 5.3 using an analogy with the case of deep traps in a semiconductor with shallow dopants. The form of the depletion region edge in the presence of deep acceptors is discussed in section 5.4.

The calculations in this chapter assume a hole effective mass $m^*_h = 0.8$ m_O,[9] degeneracy $g = 2$, and dielectric constant $\varepsilon = 9.5$ ε_O.[10] The first two values differ somewhat from those used in chapter 2; these discrepancies, which are discussed at the end of section 5.4, have little impact on the calculations. As discussed in chapter 2, the reported values for the acceptor activation energy (ΔE_A) in Mg-doped GaN vary widely. Because of the spread in reported data, and in order to keep the discussion of greater general applicability, a variety of activation energies are considered in each section. Compensation by background

114

donors is also considered—these donors may play a significant role in determining the band-diagram since their density may easily exceed the free carrier concentration in the bulk.

Comparison to the calculated results is provided by variable-frequency capacitance measurements performed on GaN p-n junction samples employing Mg-doping in the top (p-type) layer. A p-n junction layer structure is preferable to a Schottky diode for these capacitance measurements because a much lower series resistance can be obtained using the n-GaN layer (a large series resistance may lead to erroneous data in high-frequency measurements).[4] Samples with different doping levels in the p-type layer were studied; these are the same samples discussed in section 2.6.

5.2 Large signal dispersion

The impact of the large-signal dispersion can be illustrated by considering a GaN-based n-p-n BJT with a Mg-doped p-type base layer. In this device, we expect base narrowing to be a much more significant problem in high-frequency operation than will be evident from low frequency measurements. The distribution of the depletion region at the base-collector junction will be determined by the relative magnitudes of the ionized acceptor concentration in the base and the (shallow) donor concentration in the collector. Thus the Early voltage will be strongly dependent on the ionized acceptor concentration within the depleted portion of the base, as shown in figure 5.1. The calculations for this figure were performed at various collector doping levels, and at a total collector-base bias of $V = V_{bi}+V_{CB} = 8$ V (where V_{bi} is the built-in voltage). We assume a metallurgical base thickness of $W = 1000$ Å and an infinite collector thickness.

The Early voltage was calculated by determining the undepleted base width w_b:

$$w_b = W - \sqrt{\frac{2\varepsilon}{qN_A^-}fV} \ , \tag{5.1}$$

where N_A^- is the ionized acceptor concentration within the base, and base-width modulation from the emitter-base junction has been neglected. fV represents the portion of the potential drop V which falls within the base:

$$f = \frac{N_D}{N_A^- + N_D} \ , \tag{5.2}$$

where N_D is the donor concentration in the collector. The Early voltage V_A was calculated from the derivative of the collector current density J_C with respect to bias V:

$$J_C = qD_n \frac{n_p(0)}{w_b} = J_{C0} \frac{1}{1 - \sqrt{\dfrac{2\varepsilon}{qN_A^-} \dfrac{fV}{W^2}}} \ , \tag{5.3}$$
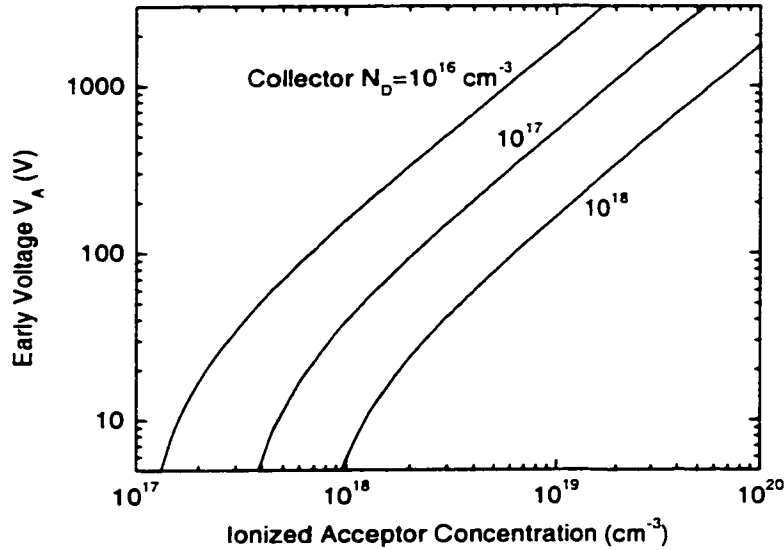

Figure 5.1 Calculated Early voltage (V_A) for a GaN bipolar transistor with a 1000 Å thick base, as a function of the ionized acceptor concentration within the depleted portion of the base. The collector doping is varied.

$$V_A = J_C \left(\frac{dJ_C}{dV}\right)^{-1} = W \sqrt{\frac{2qN_A^-}{\varepsilon} \frac{V}{f}} - 2V, \tag{5.4}$$

where $n_p(0)$ is the minority carrier concentration at the emitter-edge of the base and D_n is the electron diffusion constant.

In low-frequency operation, all the acceptors within the depletion region will ionize. As a result, depletion will occur almost entirely in the collector, leading to a high Early voltage. Under large-signal high-frequency operation, however, only the mobile holes will be able to respond and the depletion region will therefore extend significantly farther into the base. This dispersion mechanism is illustrated in figure 5.2. Under continuous-wave operation, the depleted base will be in a non-equilibrium condition so the steady-state ionized acceptor concentration is difficult to calculate. We examine a worst-case scenario in which the ionized acceptor concentration remains fixed at the equilibrium hole concentration. For a collector doping level $N_D = 1\times10^{16}$ cm^{-3} and Mg-doping in the base of $N_A = 1\times10^{19}$ cm^{-3} (equilibrium hole concentration $p_0 = 4\times10^{17}$ cm^{-3} assuming $\Delta E_A = 160$ meV and no compensation), we calculate a DC Early voltage of 1700 V which may drop as low as 50 V at high frequency. In this case, base
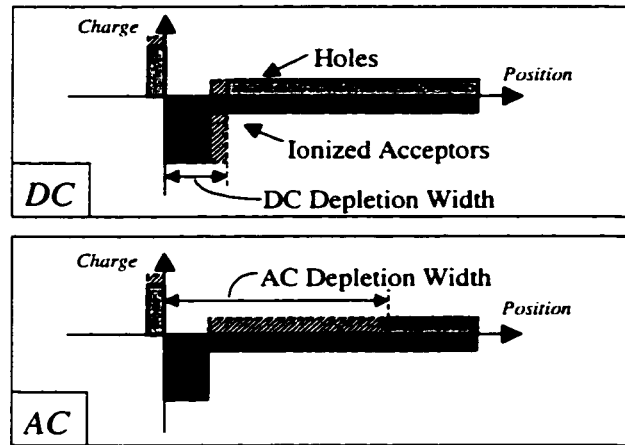

Figure 5.2 Schematic diagram illustrating the mechanism of large-signal dispersion in Mg-doped GaN.

punch-through will occur at $V_{CB} \approx 150$ V, a significant concern since GaN based BJTs are proposed as high power switching devices. These calculated results are summarized in table 5.1.

The dispersion is expected to play an important role in the high-speed performance of any GaN-based device employing reverse-biased p-n junctions, including photodiodes and junction-gated field effect transistors in addition to BJTs. Indeed, it has already been suggested that this phenomenon dominates the AC performance of AlGaN-based photodiodes.[8] A full calculation of the large-signal dispersion involves both the trap response time and field-enhanced ionization effects, and therefore is not readily tractable. The best way to develop an understanding of the large-signal dispersion may be to analyze the high-frequency performance of GaN-based bipolar transistors, once such data becomes available. It is interesting to note that the use of deep dopants in the base of a bipolar transistor has recently been implemented intentionally in a Si n-p-n transistor. Kizilyalli, et al. report on a BJT with an In-doped base which exhibits a high current gain due to the low Gummel number, and a high DC Early voltage because of the full ionization of the In acceptor within the depletion region.[11] The authors, however, do not discuss the AC implications of this device design, or provide any data on the Early voltage at high frequency.

Frequency	Early Voltage V_A	Base punch-through V_{CB}
Low	1700 V	~ 100 kV
High	50 V	150 V

Table 5.1 Calculated parameters for GaN n-p-n bipolar junction transistor performance. A base width of 1000 Å is assumed. Base doping is $N_A=10^{19}$ cm^{-3} without compensation ($p_0=4\times10^{17}$ cm^{-3}), collector doping is $N_D=10^{16}$ cm^{-3}. The high frequency values represent a worst-case scenario in which the ionized acceptor concentration remains fixed at p_0.

5.3 Small-signal dispersion

The depletion region of Mg-doped GaN is shown schematically in figure 5.3. The band-bending and small-signal dispersion that will be observed in this case are similar in form to that which will be obtained in the more commonly studied case of a deep trap in a semiconductor doped with a shallow dopant. This equivalence was first suggested in a study by Schibli and Milnes of In-doped Si, in which a simpler model was used for the time-response of the depletion
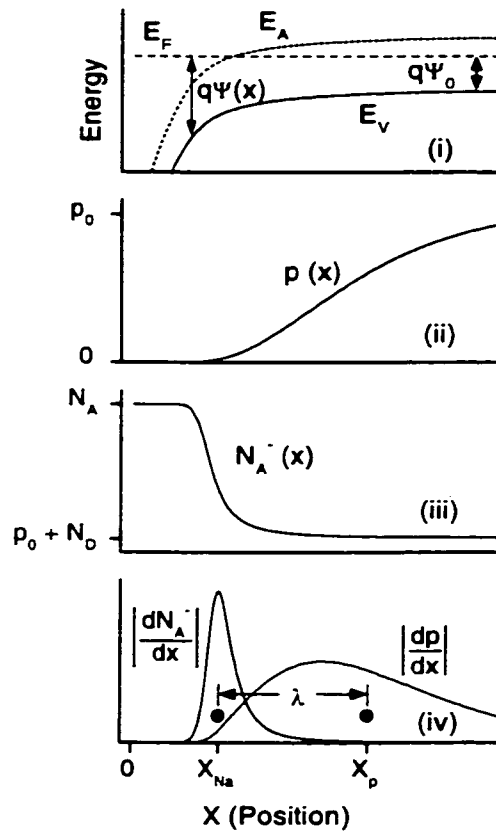

Figure 5.3 Schematic diagram of depletion region with deep acceptor level. Valence band-diagram is shown in (i). Hole and ionized acceptor concentrations are plotted in parts (ii) and (iii) respectively. In part (iv) the charge distributions resulting from a shift in the depletion region are plotted (not to scale). The solid circles represent the centroids of the two charge distributions.

region.[12] In both cases there is a spatial separation (labeled λ) between the position where the deep level ionizes and the depletion edge for the free carriers. When shallow dopants are present they are ionized throughout, and are the source of free carriers within the bulk. In the absence of shallow dopants, free carriers come only from the ionized deep levels. In this case, therefore, the free carrier tail will necessarily overlap with the region of changing ionization of the deep level. We define three regions in this case: a fully-depleted region in which the deep level is completely ionized, a transition region in which the ionization of the deep level is varying, and a bulk region in which space-charge neutrality is obtained.

Shifting the depletion region profile by applying a small bias results in two charge distributions, one due to the changing ionization of the deep levels and one due to the motion of the free carriers. The centroid of each distribution is indicated in figure 5.3 and the positions are labeled x_{Na} and x_p respectively. The distance between the two centroids is λ.

In low-frequency capacitance measurements both of these charge distributions will form. The resulting capacitance will be determined by a weighted average of the two centroid positions. By collapsing each distribution to a pulse located at the centroid, the charge response position for the low-frequency capacitance (x_{LF}) may be calculated. For a semiconductor with deep acceptor concentration N_A, compensating donor concentration N_D (these are assumed to be ionized throughout), and bulk hole concentration p_0, the value of x_{LF} is given by equation (5.5).

$$x_{LF} = \frac{(N_A - N_D - p_0)x_{Na} + p_0 x_p}{N_A - N_D} \qquad (5.5)$$

At room temperature $N_A - N_D \gg p_0$ so that $x_{LF} \approx x_{Na}$. (As a result, the net acceptor density $N_A - N_D$ can be obtained in the usual way from the low-frequency

capacitance measured as a function of DC bias.) At high frequency only the mobile holes can respond to the applied bias, so the high frequency charge response position is simply $x_{HF} = x_p$. The resulting dispersion in the small-signal capacitance measurements has been extensively investigated in the case of lightly-doped materials with deep levels—the phenomenon forms the basis of the admittance spectroscopy technique.[13] The existing theory can be applied to the present case with only minor modifications.

The exact form of the C-f curve for the case of a shallow dopant and a deep trap has been analyzed by Oldham and Naik,[3] using a model subsequently generalized by Ghezzi.[14] In this work we extend this model to apply to the case of a single deep dopant. The capacitance behavior in either case is described by equation (5.6) where f_1 is the transition frequency and C_{LF} is the capacitance in the low-frequency limit.

$$C = C_{LF} - \frac{\Delta C}{1 + (f_1/f)^2}$$ (5.6)

It is clear from physical considerations that both the distance λ and the shift in capacitance response position $\Delta d = x_{HF} - x_{LF} \approx \lambda$ will be independent of the applied DC bias. We note that because the high-frequency capacitance varies from the low-frequency value simply as a result of this Δd, high-frequency capacitance-voltage measurements cannot be used to extract the hole concentration as some authors have claimed.[6]

Experimental measurements of zero-bias capacitance were performed as a function of frequency (C-f measurements) on the GaN p-n junction samples. The experiments used a Hewlett-Packard 4192A LF impedance analyzer, which provided accurate capacitance measurements from 1 kHz to 5 MHz. These small-signal measurements were insensitive to the magnitude of the AC bias applied (an AC bias of 50 mV was used in the majority of the measurements).

We found that proper calibration of the impedance analyzer was imperative for accurate measurements at frequencies above 100 kHz. Because the instrument itself is only able to calibrate at a single, fixed frequency, a separate control program was written which performed an external calibration. The program first performed impedance measurements in the open circuit and short circuit configurations in order to determine the impedance values in series and parallel with the device under test, at every measurement frequency. These values were stored and subsequently used to calculate the true impedance from the values measured on the device under test. Figure 5.4 shows a test measurement performed on a dielectric chip capacitor with a nominal capacitance of 200 pF. Accurate measurements of capacitance as a function of frequency could not be obtained at frequencies above 100 kHz without the external calibration program;
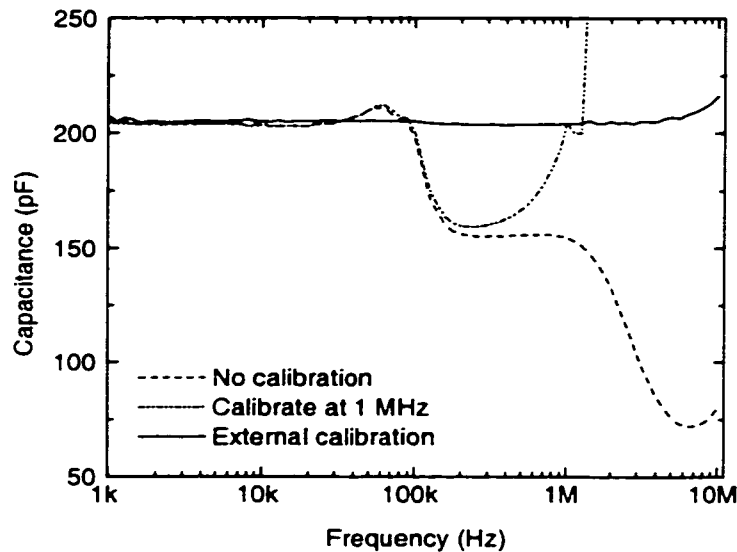

Figure 5.4 Capacitance measured as a function of frequency on a dielectric chip capacitor with a nominal capacitance of 200 pF. Accurate measurements are achieved only with the external calibration program.

122

with the program, accurate measurements were obtained at frequencies up to 5 MHz.

Some representative C-f measurements for the GaN p-n junctions are shown in figure 5.5; they are fit to equation (5.6) with a high degree of success. Figure 5.6 plots the charge response positions x_{LF} and x_{HF} as a function of reverse bias for one of the more lightly doped samples. As expected, the separation Δd is independent of bias.

The close fit between the experimental data and the results predicted by the admittance spectroscopy theory strongly suggests that the capacitance dispersion is indeed due to the response time of the deep Mg acceptor. The data could also support the model of dispersion due to an even deeper trap level within the material, however very high trap concentrations would be required in order to
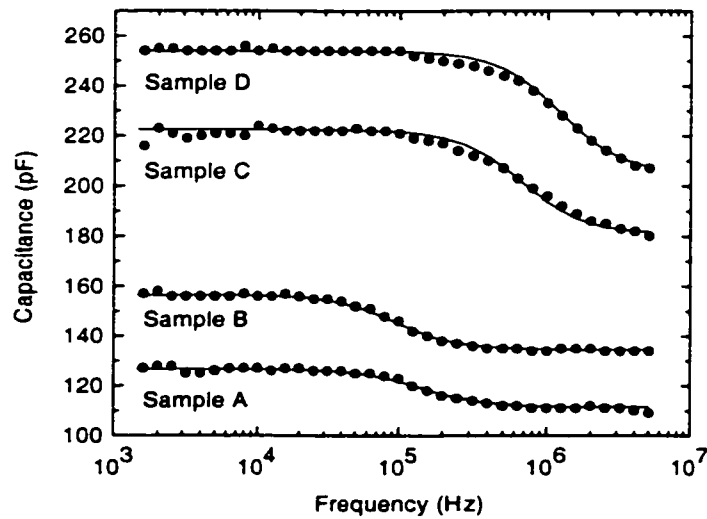

Figure 5.5   Measurements of zero-bias capacitance on GaN p-n junctions as a function of frequency (solid circles). The lines are calculated by using equation (5.6) to fit the measured data.

observe the effect in these heavily-doped materials, so the former hypothesis seems more likely.

In admittance spectroscopy one often measures the transition frequency as a function of temperature in order to extract the energy level of the state. A characteristic frequency f_0 may be defined by assuming a Shockley-Read-Hall form for the emission rate of the deep dopant (where σ is the cross-section):

$$f_0 \propto T^2 \sigma \exp\left(-\frac{\Delta E_A}{kT}\right).$$

(5.7)

However it is important to note, as Ghezzi points out, that this frequency is different from the transition frequency f_1. The difference is often small in the usual case involving shallow dopants with a relatively low concentration of deep states, but it will be a dominating factor in the case at hand where the number of
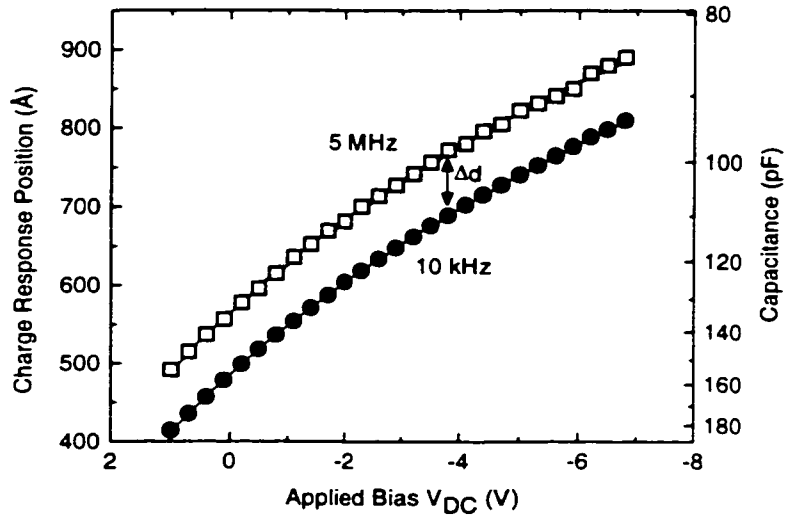

Figure 5.6 Capacitance-voltage measurements performed on sample B at both high and low frequency. The charge response is shifted by Δd = 79 Å, a value which is independent of the applied DC bias.

124

deep levels (N_A) is far greater than the bulk carrier concentration. Modifying Ghezzi's equation to fit the present case we find:

$$f_1 = f_0 \left(1 + \frac{x_{Na}}{x_p} \frac{N_A - N_D - p_0}{p_0} \right).$$ (5.8)

Thus the temperature-dependence of f_1 is much more complicated than that of f_0. The second term within the parentheses in equation (5.8) will dominate at room temperature, and its temperature dependence will act to nearly cancel that of f_0. There have been attempts within the literature for Mg-doped GaN to fit f_1 to an equation of the form (5.7);[8] while these have yielded reasonable values for ΔE_A, the physical interpretation of the data is unclear. Efforts to fit the temperature dependence of the capacitance in the present samples have not been successful. Finally, we note that the room temperature values of f_1 appear to scale roughly with the net acceptor density N_A-N_D. The value of N_A-N_D for each of the samples is listed in table 5.2 and was determined from low-frequency C-V measurements combined with knowledge of the donor doping on the n-side of the junction.

Sample	p_0 (cm^{-3})	μ (cm^2/Vs)	N_A-N_D (cm^{-3})
A	1.7×10^{17}	25	1.5×10^{18}
B	2.7×10^{17}	20	2.3×10^{18}
C	5.3×10^{17}	13	4.1×10^{18}
D	6.1×10^{17}	5.8	9.1×10^{18}

Table 5.2 Summary of room-temperature electrical measurements performed on Mg-doped GaN samples. Hole concentration and mobility were measured using the Hall effect, and the net acceptor concentration was obtained through low-frequency capacitance-voltage measurements.

5.4 Form of the depletion region

In this section we analyze the band-bending within the transition region of the depletion region for a semiconductor doped with a deep acceptor and some compensating donors. An analytical approximation is derived which allows us to estimate the distance λ; this is compared to the experimental values extracted from the capacitance measurements.

The hole concentration and the ionized acceptor concentration are determined using the standard formulas given in equations (5.9) and (5.10). The Boltzmann approximation is used in equation (5.9). E_F represents the energy of the Fermi level, E_V is the energy of the valence band edge, and N_V is the effective valence-band density of states.

$$p = N_V \exp\left[-\frac{(E_F - E_V)}{kT}\right]$$ (5.9)

$$N_A^- = \frac{N_A}{1 + g\exp\left(\frac{E_A - E_F}{kT}\right)}$$ (5.10)

The equilibrium hole concentration in the bulk (p_0) is calculated by finding the Fermi energy that satisfies the requirement of charge neutrality.

Within the transition region we define the energy of the valence band edge by $\psi(x)$ so that:

$$\psi(x) = \psi_0 + \Delta\psi(x) = \left[E_F - E_V(x)\right] / q,$$ (5.11)

where q is the electronic charge. The ionized acceptor concentration is written approximately as:

$$N_A^- \approx (p_0 + N_D)\exp\left(\frac{q\Delta\psi}{kT}\right),$$ (5.12)

so that both $p(x)$ and $N_A^-(x)$ vary exponentially with the band-bending $\Delta\psi(x)$. Applying Poisson's equation within the transition region then yields:

$$\frac{d^2 \Delta \psi}{dx^2} = \frac{q}{\varepsilon} \left[(p_0 + N_D) \exp\left(\frac{q \Delta \psi}{kT} \right) - p_0 \exp\left(-\frac{q \Delta \psi}{kT} \right) - N_D \right]. \quad (5.13)$$

This differential equation is easily solved by employing a Taylor expansion for the exponentials. The band bending is found to be exponential and characterized by a modified Debye length L_{D*}:

$$\Delta \psi(x) \propto \exp(-x / L_{D*}) \quad (5.14)$$

$$L_{D*} = \sqrt{\frac{\varepsilon \, kT}{q^2 (2p_0 + N_D)}} \quad (5.15)$$

This straightforward result is extremely useful in providing a simple equation for the band-bending in the transition region.

These equations now allow the easy construction of approximate band-diagrams for the depletion region based solely on the knowledge of bulk parameters (p_0, N_A, N_D) and the total voltage drop $\Delta \psi(0)$. An example is shown in figure 5.7, where we have considered a depleted p-type GaN layer doped at $N_A = 2 \times 10^{19}$ cm^{-3} and $N_D = 2 \times 10^{18}$ cm^{-3} with $\Delta E_A = 230$ meV. The results are compared with the band diagram calculated numerically using a self-consistent Poisson equation solver[15]—the fit is excellent over the great majority of the depletion region.

In order to calculate the band-bending shown in figure 5.7, we introduced the position x'_{Na}, which is defined as the boundary between the transition region, where equation (5.14) is applied, and the fully depleted region, in which complete ionization of the acceptor and the complete absence of mobile holes is assumed. The position of x'_{Na} is determined as the location where equation (5.12) predicts full ionization, so that:

$$\Delta \psi(x'_{Na}) = \frac{kT}{q} \ln\left(\frac{N_A}{N_D + p_0} \right) \quad (5.16)$$

This simplified model for the dependence of the ionized acceptor concentration on the Fermi level position, combined with the breakdown of the Taylor expansion at $\Delta\psi \gtrsim kT/q$, is responsible for the slight deviations evident in figure 5.7.

In order to find x'_{Na} as a function of the total band bending $\Delta\psi(0)$, one must consider band bending due both to the transition region and the fully depleted region:
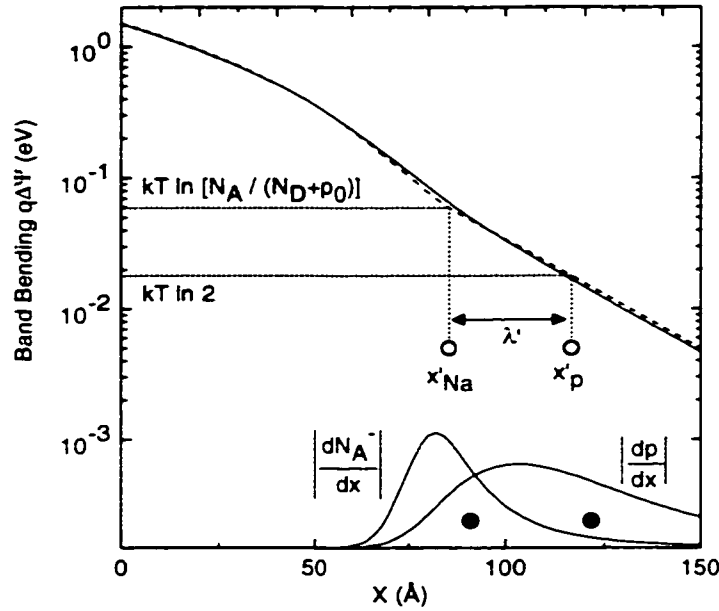

Figure 5.7   Comparison of band-bending $q\Delta\psi$ as calculated numerically by a self-consistent Poisson equation solver (solid line) and approximated using the analytical formulae developed in the text (dashed line). The calculations are carried out for p-type GaN with acceptor activation energy $\Delta E_A=230$ meV and density $N_A=2\times10^{19}$ cm^{-3} with compensating donors $N_D=2\times10^{18}$ cm^{-3}. Shown on the bottom are the differential charge distributions (not to scale); the solid dots represent the positions of x_{Na} and x_p.

$$\Delta \psi(0) = \Delta \psi(x'_{Na}) + x'_{Na} E(x'_{Na}) + \frac{q(N_A - N_D)}{2\varepsilon}(x'_{Na})^2, \quad (5.17)$$

where $E(x'_{Na})$ is the electric field at x'_{Na} given by:

$$E(x'_{Na}) = \frac{\Delta \psi(x'_{Na})}{L_{D^*}}. \quad (5.18)$$

x'_{Na} is found by combining these equations and solving the resulting quadratic equation.

The positions of the charge centroids x_{Na} and x_p for this case were extracted by numerically analyzing the simulated band-diagram, and their positions are also plotted on figure 5.7. We find that x'_{Na} reasonably approximates the position of x_{Na}. The position of x_p can also be approximated: we define x'_p as the position where the hole concentration falls to half its bulk value.

$$\Delta \psi(x'_p) = \frac{kT}{q} \ln 2 \quad (5.19)$$

The approximate transition region thickness λ' can then be easily calculated:

$$\lambda' = x'_p - x'_{Na} = L_{D^*} \ln\left\{\frac{\ln[N_A/(p_0 + N_D)]}{\ln 2}\right\} \quad (5.20)$$

Values of λ (extracted from simulations using the Poisson equation solver) and λ' (calculated using equation (5.20)) for various doping conditions are plotted in figure 5.8. The fit is quite good; equation (5.20) provides useful estimates of the transition region width over a wide range of doping conditions. The calculations in figure 5.8 assume no compensation; it is clear from equations (5.15) and (5.20) that a high compensation ratio will severely reduce the width of the transition region λ.

Also plotted on figure 5.8 are experimental values of λ obtained from the capacitance measurements on the GaN p-n junctions. The values obtained are consistent with an acceptor activation energy $\Delta E_A \approx 160$ meV with negligible

compensation. The values of N_A for this plot are obtained from the low-frequency C-V measurement results presented in table 5.2, with the assumption of no compensation. We note that the acceptor concentration obtained in this fashion is significantly lower than that extracted from variable temperature Hall effect measurements on these samples (see section 2.6). This discrepancy may be due to a reduced acceptor doping density near the p-n junction, which might result from the Mg "doping delay" frequently linked to the memory effect in MOCVD growth of Mg-doped GaN.[16] The relatively low compensation ratio and constant activation energy implied by the capacitance measurements also vary from the results of section 2.6; these discrepancies might also be linked to a lower doping density.
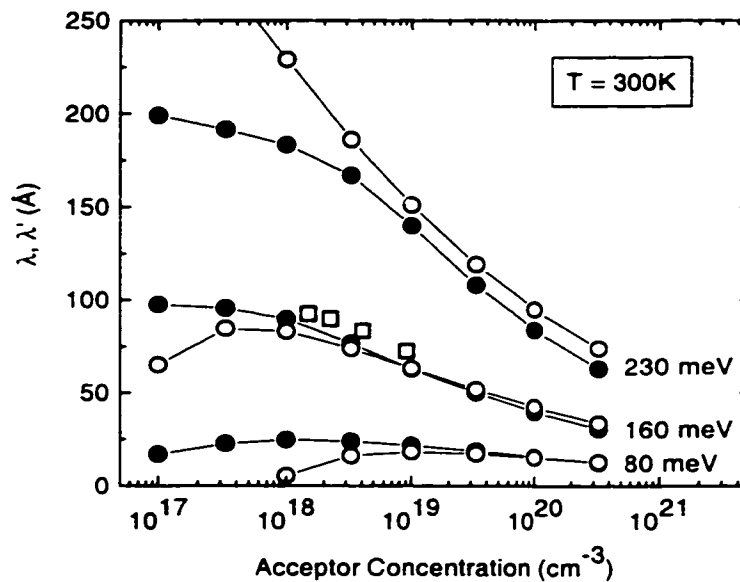

Figure 5.8 Width of the transition region as a function of acceptor concentration in p-type GaN. The acceptor energy level ΔE_A is varied. The solid circles represent values of λ extracted from band-diagrams simulated using a self-consistent Poisson equation solver; the open circles are values of λ' calculated using equation (5.20). The squares represent values of λ measured from the Mg-doped GaN samples.

Another source of the discrepancy may be the value of the hole effective mass used in these calculations. The hole mass will influence the results by changing the valence-band density of states N_V and therefore the bulk hole concentration p_0. Figure 5.9 illustrates the values of λ' which result from varying m^*_h. While the overall trends in λ' are clearly independent of hole mass, the uncertainty in m^*_h is an additional factor that complicates efforts to numerically match the measured results with calculated values.
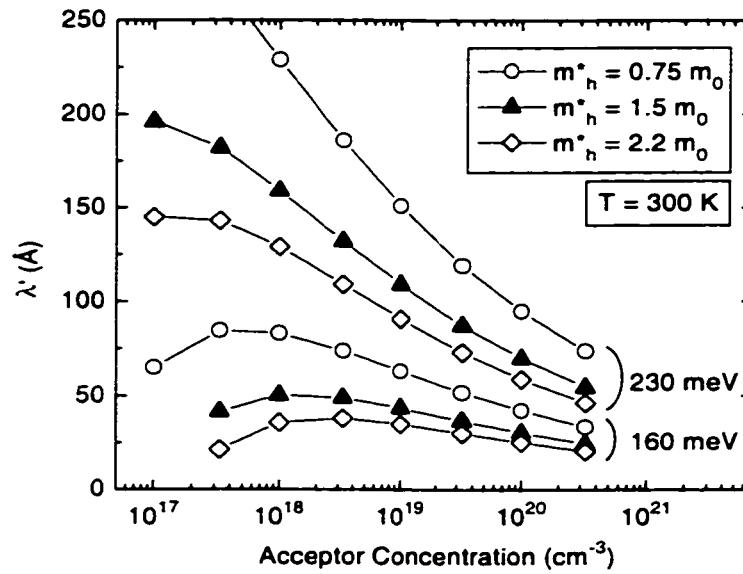
Figure 5.9 Calculated transition region width λ' as a function of acceptor concentration. The acceptor binding energy and valence band hole mass are varied. The calculations assume no compensation.

131

5.5 Conclusions

The nature of the depletion region in the presence of deep dopants has been examined, with particular focus on the case of Mg-doped GaN for bipolar transistor applications. The form of the depletion region is similar to the well-studied case of a material doped both with shallow dopants and deep traps. Dispersion effects will result from the time required for the dopant to change ionization states. The extent of the dispersion in large-signal high-frequency modulation is difficult to calculate; however, a worst-case scenario has been discussed for the case of GaN bipolar transistors. Dispersion effects in the small-signal capacitance have been used to characterize the transition region. Experimental data fits the theory well and suggests a reduced doping density near the *p-n* junction.

5.6 References

1   H. Morkoc, S. Strite, G. B. Gao, M. E. Lin, B. Sverdlov, and M. Burns, "Large-band gap SiC, III-V nitride, and II-VI ZnSe-based semiconductor device technologies." *J. Appl. Phys.* **76**, 1363-1398 (1994).

2   C. T. Sah and V. G. K. Reddi, "Frequency Dependence of the Reverse-Biased Capacitance of Gold-Doped Silicon P+N Step Junctions." *IEEE Trans. on Electron Devices* **11**, 345-349 (1964).

3   W. G. Oldham and S. S. Naik, "Admittance of p-n Junctions Containing Traps." *Solid-St. Electron.* **15**, 1085-1096 (1972).

4   G. H. Glover, "The C-V Characteristics of Schottky Barriers on Laboratory Grown Semiconducting Diamonds." *Solid-St. Electron.* **16**, 973-983 (1973).

5   T. Ohori, M. Takikawa, and J. Komeno, "Frequency dependence of capacitance-voltage characteristics caused by DX centers in Si-doped AlGaAs." *J. Appl. Phys.* **63**, 1223-4 (1988).

6   J. W. Huang, T. F. Kuech, L. Hongqiang, and I. Bhat, "Electrical characterization of Mg-doped GaN grown by metalorganic vapor phase epitaxy." *Appl. Phys. Lett.* **68**, 2392-4 (1996).

7   Y. Zohta, H. Kuroda, R. Nii, and S. Nakamura, "Frequency dependence of the reverse-biased capacitance of blue and green light-emitting diodes." *J. Cryst. Growth* **189/190**, 816-819 (1998).

8   E. Monroy, M. Hamilton, D. Walker, P. Kung, F. J. Sanchez, and M. Razeghi, "High-quality visible-blind AlGaN p-i-n photodiodes." *Appl. Phys. Lett.* **74**, 1171-1173 (1999).

9   J. J. Pankove, S. Bloom, and G. Harbecke, "Optical Properties of GaN." *RCA Rev.* **36**, 163-176 (1975).

10   M. Razeghi and A. Rogalski, "Semiconductor ultraviolet detectors." *J. Appl. Phys.* **79**, 7433-7473 (1996).

11   I. C. Kizilyalli, A. S. Chen, W. J. Nagy, T. L. Rich, T. E. Ham, K. H. Lee, M. S. Carroll, and M. Iannuzzi, "Silicon npn bipolar transistors with indium-implanted base regions." *IEEE Electron Device Lett.* **18**, 120-2 (1997).

12   E. Schibli and A. G. Milnes, "Effects of Deep Impurities on n+p Junction Reverse-Biased Small-Signal Capacitance." *Solid-St. Electron.* **11**, 323-334 (1968).

13   D. L. Losee, "Admittance Spectroscopy of impurity levels in Schottky barriers." *J. Appl. Phys.* **46**, 2204-2214 (1975).

14   C. Ghezzi, "Space-Charge Analysis for the Admittance of Semiconductor Junctions with Deep Impurity Levels." *Appl. Phys. A* **26**, 191-202 (1981).

15   The simulation program used, "1D-Poisson" by G. L. Snider, is available through the internet at http://www.nd.edu/~gsnider.

16   Y. Ohba and A. Hatano, "A study on strong memory effects for Mg doping in GaN metalorganic chemical vapor deposition." *J. Cryst. Growth* **145**, 214-218 (1994).

133

Chapter 6

Mg-doped AlGaN/GaN superlattices

6.1 Introduction

The deep nature of the Mg acceptor and the consequently low hole concentration in p-type GaN and AlGaN are serious obstacles for achieving high-performance optoelectronic and electronic devices. This problem is further exacerbated when device operation at lower temperatures is desired, as these lower temperatures lead to a diminishing hole concentration. New techniques are needed to increase the p-type conductivity and eliminate the temperature sensitivity in these materials in order for GaN-based devices, especially bipolar transistors, to achieve their full potential.

The low doping efficiency that is an inherent property of a deep acceptor can be partially overcome through the application of a periodic oscillation to the valence band edge. Acceptors are ionized where the band edge is far below the Fermi energy and the resulting holes accumulate where the band edge is close to the Fermi level, forming confined sheets of carriers. Although the free carriers are separated into parallel sheets, their spatially-averaged density will be much higher than in a simple bulk film. Superlattices produce the necessary valence band edge oscillation by employing alloys with different valence band edge positions. As first proposed by Schubert et al., this technique increases the overall hole concentration by allowing deep acceptors in the barriers to ionize into the valence band of the neighboring narrow band-gap material, rather than into the (deeper) valence band of the host material.[1,2] Such doped AlGaN/GaN superlattices (both n-type and p-type) have been applied in laser diodes for strain

135

relief purposes,[3] and some data suggesting a reduced acceptor activation energy have been reported.[4]

There is significant evidence of large polarization fields in nitride materials.[5,6] An AlGaN/GaN superlattice will support polarization fields due both to the piezoelectric effect in the strained AlGaN layers and the difference in spontaneous polarization between the two layers.[7,8] These fields create a periodic sawtooth variation in the band-diagram, a phenomenon that has been studied in conventional compound semiconductors grown on (111) substrates.[9] The polarization-induced valence band edge oscillation adds to that created by the valence band discontinuity, resulting in further enhancement of the hole concentration. The impact of the AlGaN/GaN superlattices on the average carrier density is addressed in this chapter through both numerical simulations and experimental measurements.

6.2 Uniformly-doped superlattices

For these experiments, the sample design consisted of an $Al_{0.2}Ga_{0.8}N/GaN$ superlattice in which the barrier and well thickness (L) were kept equal. The superlattice period ($2L$) was varied. The aluminum percentage in the barrier was fixed at 20%, a value easily achieved in MOCVD growth. Mg doping was applied uniformly throughout both the barrier and well. Modulation doping by MBE is discussed in section 6.3—the severe Mg memory effect makes modulation doping by MOCVD difficult to realize.

Superlattice structures were simulated using a one-dimensional Poisson and Schrödinger equation solver.[10] The simulations assumed a uniform Mg doping of $N_A=5\times10^{19}$ cm^{-3}, no compensation, and an acceptor ionization energy of $\Delta E_A=230$ meV in both the GaN and AlGaN layers. The simulations also assume a hole effective mass of $m^*_h=0.8\,m_0$, a dielectric constant of $\varepsilon=9.5\,\varepsilon_0$ and

degeneracy $g=2$. These values are somewhat different from those used in chapter 2; the effects of this discrepancy are minor and are discussed below. The valence band discontinuity (ΔE_V) was assumed to be 20% of the bandgap difference; for an aluminum mole fraction of 20% this yields $\Delta E_V=112$ meV, which is significantly less than ΔE_A.

Calculated values of the hole concentration at 300K (averaged over the superlattice period) are shown as a function of superlattice dimension L in figure 6.1. Three important effects are addressed independently. The first is that described by Schubert, et al., in which quantization and polarization effects are neglected and the valence band-edge modulation is provided only by the discontinuity ΔE_V. Holes accumulate at each interface, so a dense array of
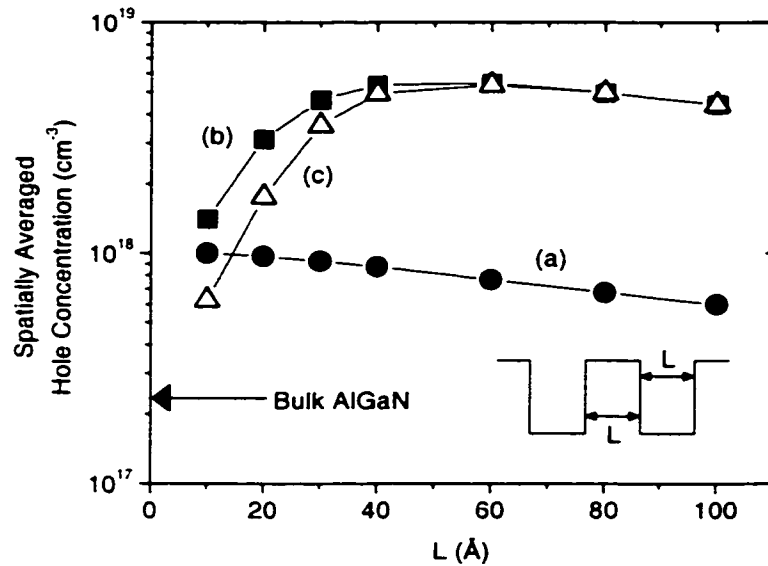
Figure 6.1 Calculations of the spatially averaged hole concentration (at 300K) for Mg-doped AlGaN/GaN superlattices as a function of the superlattice dimension L. The calculations (a) ignore the polarization fields, (b) include them and (c) include both polarization fields and quantization effects. The hole concentration calculated for a bulk AlGaN film is indicated by the arrow.

137

interfaces (hence a short dimension superlattice) will maximize the spatially-averaged carrier density. Thus the calculated hole concentration shown in curve (a), which is significantly higher than that of the bulk sample, decreases as L is increased. The valence-band diagram for this system is shown in figure 6.2 (a).

Polarization effects were simulated by including fixed charge sheets of equal magnitude but opposite type at alternating heterointerfaces. The total polarization charge due to the change in spontaneous polarization (ΔP_{SP}) as well as the piezoelectric effect (P_{PZ}) is calculated (neglecting shear strain) as:

$$\Delta P = \Delta P_{SP} + P_{PZ} = (P_{SP}^{AlGaN} - P_{SP}^{GaN}) + 2(e_{31} + \frac{c_{13}}{c_{33}}e_{33})E_x \qquad (6.1)$$

where E_x is the in-plane strain of the pseudomorphic AlGaN layer and is calculated from the lattice constants of the binaries AlN and GaN,[11] using a linear interpolation to estimate the value for $Al_{0.2}Ga_{0.8}N$. A similar interpolation
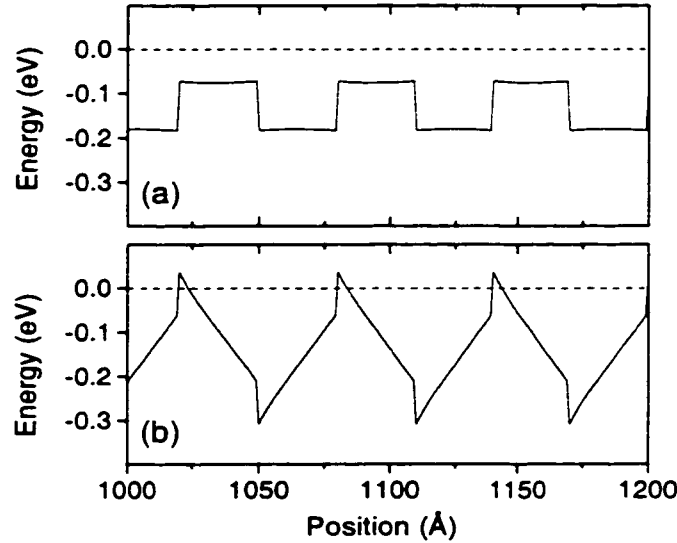

Figure 6.2   Calculated valence band diagram for Mg-doped $Al_{0.2}Ga_{0.8}N/GaN$ superlattice in which the thickness of each layer is $L=30$ Å, shown (a) without and (b) with the polarization fields taken into account. In both plots the Fermi energy is indicated by the dashed line.

between published values for AlN and GaN is performed in order to find the spontaneous polarization P_{SP} and piezoelectric constants e_{31} and e_{33},[8] and the elastic coefficients c_{13} and c_{33}.[12] The resulting calculation yields a charge density of 1.8×10^{-6} C / cm^2 at each interface.

Figure 6.2 (b) shows the calculated valence band-edge for a superlattice with L=30 Å. The polarization fields significantly increase the total valence band-edge oscillation. As L is increased, the band-bending caused by the polarization fields increases, resulting in a higher hole concentration. This effect is clear in curve (b) of figure 6.1, where the hole concentration is observed to increase with L in contrast to curve (a). At the optimal superlattice dimension the average hole concentration is calculated to be twenty times that achieved in the bulk film. As L is increased further the enhancement in sheet hole concentration slows due to the high space-charge which develops and screens the polarization
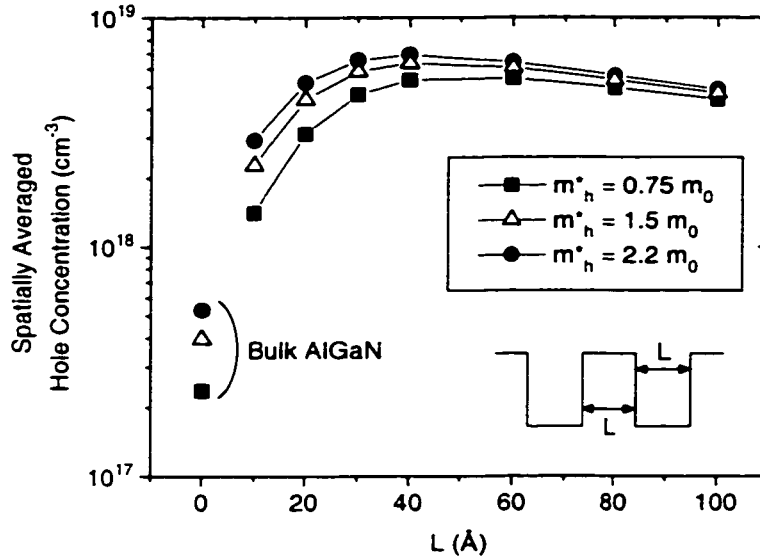

Figure 6.3   Spatially-averaged hole concentration in a uniformly Mg-doped AlGaN/GaN superlattice.   Polarization charges are taken into account; quantization effects are not.   The valence band effective mass is varied.

139

field. Eventually, the spatially-averaged hole concentration is observed to slowly decline with increasing L, a consequence of the increasing separation of the carrier sheets.

In figure 6.3, the hole concentration has been calculated as a function of L for a variety of different hole mass values. The trend is the same regardless of the value used for this parameter, and the effect of the hole mass is actually reduced at higher values of L. This is because the mass affects the hole concentration through the valence band density of states; this value plays an important role when the Fermi level is always far from the valence band edge, as in bulk
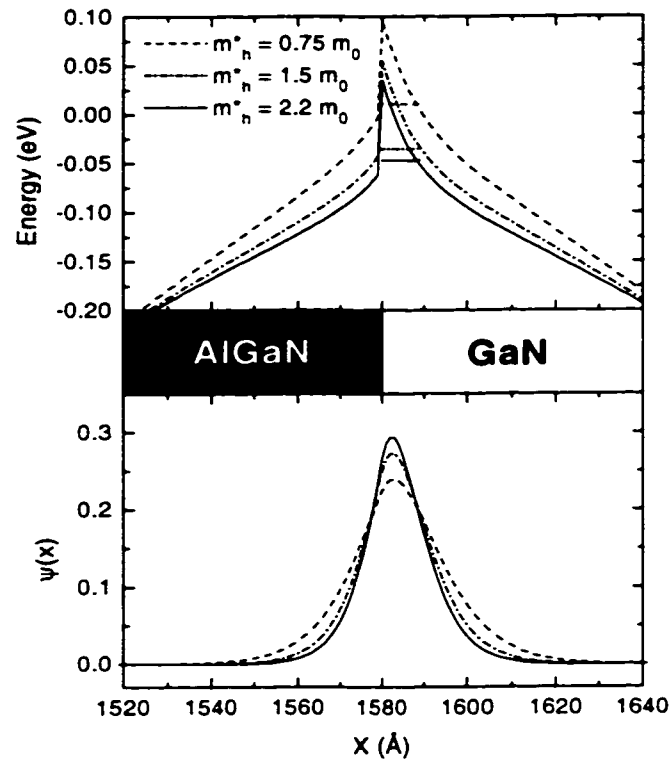

Figure 6.4 Valence band diagram (top) at AlGaN/GaN interface. The calculations assume a uniformly Mg-doped AlGaN/GaN superlattice with $L = 80$ Å. Quantization effects are included; the horizontal lines represent the ground state energy for holes. The corresponding wavefunctions are also shown (bottom). The valence band effective mass is varied.

material, but is less important when depletion and accumulation determine the hole concentration.

Finally, quantization effects must be considered. Curve (c) of figure 6.1 shows the hole concentration calculated through a simultaneous solution of the Poisson and Schrödinger equations. For the narrow-dimension superlattices the hole concentration is somewhat reduced from that calculated in curve (b), an expected result of the high ground state energy in these structures. The valence band diagram of the confined wells is shown in figure 6.4, calculated for various values of the hole mass, for a superlattice with $L = 80\text{Å}$. The ground-state wavefunctions are also displayed; the states are quite narrowly confined, with a full-width at half-maximum between 15 and 20 Å.

The experimental work was performed on samples grown by MOCVD on c-plane sapphire. The Mg-doped superlattices were approximately 0.4 μm thick, and were grown above several microns of unintentionally doped n-type GaN and
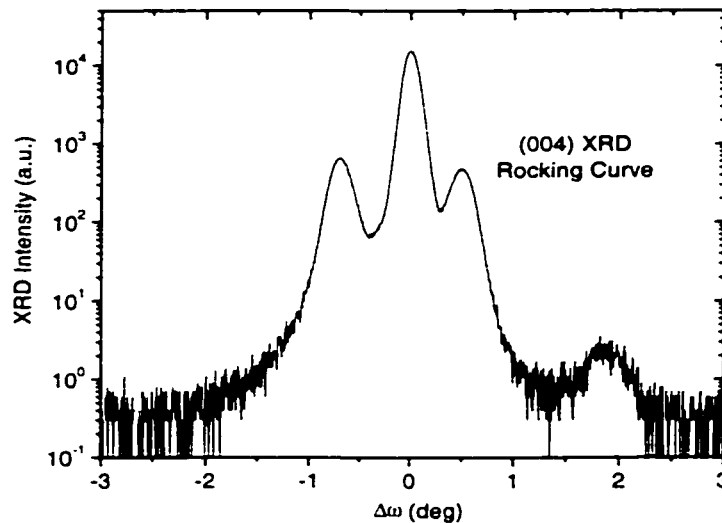

Figure 6.5 X-ray diffraction rocking curve of AlGaN/GaN superlattice. A diffraction peak from the InGaN compliance layer is also visible.

an $In_{0.05}Ga_{0.95}N$ compliance layer to prevent cracking. A thin GaN:Mg contact layer was grown as the final step. Samples with various superlattice periods were prepared. For comparison, bulk films of GaN:Mg and $Al_{0.1}Ga_{0.9}N$:Mg were grown under similar growth conditions. The aluminum mole fraction and period of the superlattices were verified through x-ray diffraction rocking-curve measurements. Figure 6.5 shows a typical x-ray diffraction rocking-curve; all the x-ray measurements were performed by Monica Hansen at UCSB.

The results of room temperature Hall-effect measurements on all the films are shown in figure 6.6. The hole concentration of the bulk GaN film was 4×10^{17} cm^{-3} and its mobility was 16 cm^2/Vs; for $Al_{0.1}Ga_{0.9}N$ these values were $1.7\times10^{17}\ cm^{-3}$ and 13 cm^2/Vs, respectively. In all the superlattice samples the mobility has been reduced to around 10 cm^2/Vs, probably as a result of increased scattering from the heterointerfaces. Interface scattering has been shown to

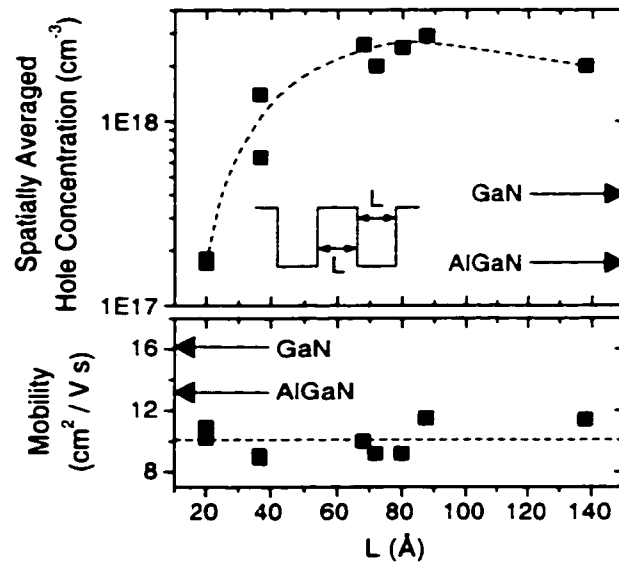Figure 6.6 Room temperature Hall effect measurements $Al_{0.2}Ga_{0.8}N$/GaN superlattices. The superlattice dimension L is varied. The arrows indicate values obtained on bulk samples of Mg-doped GaN and $Al_{0.1}Ga_{0.9}N$. The dashed lines are eye-guides.

severely reduce the electron mobility in AlGaN/GaN heterojunction field effect transistors,[13] and we expect the effect to be even stronger in p-type layers due to the very high hole mass.

As the superlattice dimension L is increased, the measured hole concentration rises quickly to around 2.5×10^{18} cm^{-3}, more than ten times the value obtained in the bulk alloy. Beyond $L \approx 70$ Å the measured hole concentration saturates and then appears to decline slightly. This sensitive dependence on the superlattice dimension L is similar to that calculated in curve (c) of figure 6.1, strongly suggesting that the polarization effects dominate the formation of the hole sheets.

Figure 6.7 shows the resistivity of the samples as a function of temperature. An effective acceptor activation energy is extracted from the Arrhenius plot by assuming the mobility is approximately constant. We note that
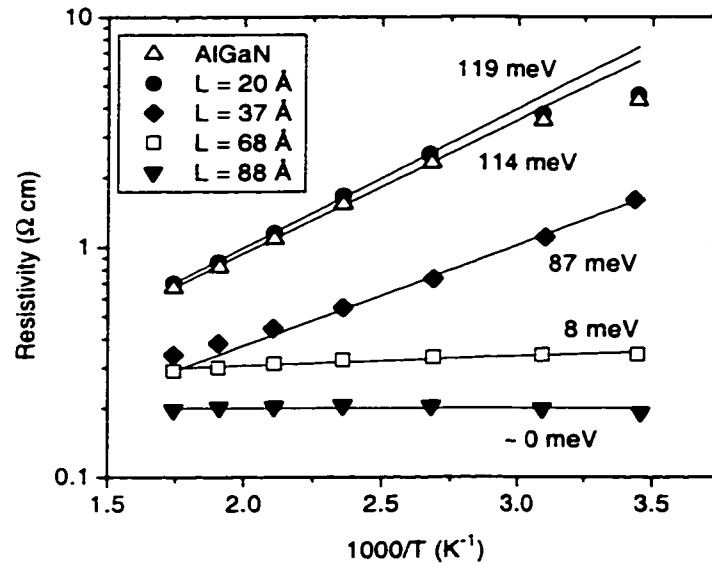

Figure 6.7 Temperature-dependent resistivity measurements. Values obtained on a bulk film of Mg-doped Al$_{0.1}$Ga$_{0.9}$N are included for comparison. The effective activation energies are obtained by fitting the data to an exponential dependence (solid lines).

the activation energies originally reported were twice the values that are shown on figure 6.7. This was due to an assumption of no compensation, so that $p \sim \exp(-\Delta E_A/2kT)$ according to case 1 of section 2.2. Because compensation has been demonstrated to play an important role, it is more accurate to apply the conditions of case 2, yielding $p \sim \exp(-\Delta E_A/kT)$.

The data for the bulk samples fit well to an activation energy of ~ 114 meV. As the superlattice dimension L is increased, the temperature dependence drops rapidly. For samples with $L=70$ Å or longer, the resistivity is nearly constant with temperature. In these films the band-bending caused by the polarization effect is enough to ensure the ionization of acceptors and the formation of a hole sheet, whereas in bulk films the ionization of the acceptor is strongly dependent on temperature. We note that the sample with $L=20$ Å shows the same hole concentration and temperature dependence as the bulk AlGaN film, suggesting either poor interface quality or that the true valence-band discontinuity ΔE_V may be quite small.
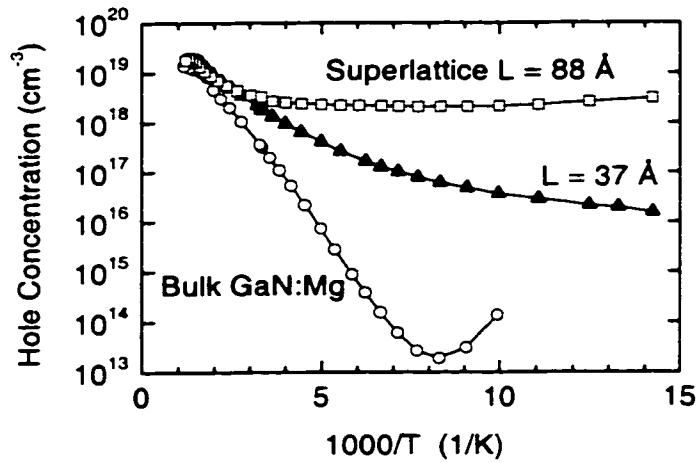

Figure 6.8 Temperature-dependent Hall effect measurements on $Al_{0.2}Ga_{0.8}N$/GaN superlattices with different values of the dimension L. Data from a bulk Mg-doped GaN sample are included for comparison.

Two superlattice samples and a bulk Mg-doped GaN film were prepared for variable-temperature Hall effect measurements, as described in section 2.3. The results of these measurements are shown in figure 6.8. At very high temperatures, all three samples exhibit the typical thermally activated hole concentration profile. As the temperature is reduced the hole concentration in the bulk film continues to fall exponentially (below 120 K the measured hole concentration appears to increase again, indicating the onset of impurity conduction). The hole concentration in the L=88 Å superlattice film, however, remains fixed at approximately 2×10^{18} cm^{-3}, which is the spatially-averaged hole concentration resulting from the polarization-induced band-bending. At room temperature this superlattice provides an enhancement of the hole concentration by approximately a factor of nine compared to the bulk film. However it is at lower temperatures that the superlattice provides the greatest advantage—the enhancement in hole concentration at a temperature of 120 K, for example, is over
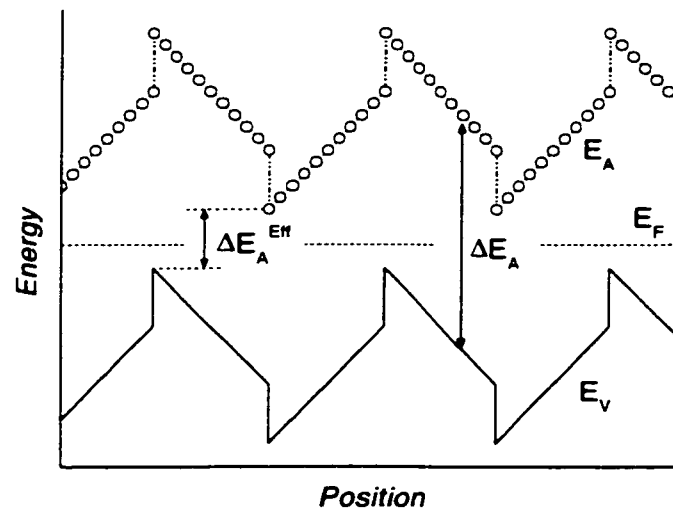

Figure 6.9 Schematic diagram of effective acceptor activation energy reduction through polarization effects in AlGaN/GaN superlattices. The solid line represents the valence band edge, the open circles represent the acceptor energy. The dashed line is the Fermi energy.

five orders of magnitude. It is also near this temperature that the mobility measured for carriers in this superlattice sample reached its peak: the highest value measured was $18 \text{ cm}^2/\text{Vs}$ at a temperature of 140 K.

In figures 6.7 and 6.8, we note that as the superlattice dimension L is increased, the effective acceptor activation energy declines steadily until reaching zero. Figure 6.9 schematically illustrates how this reduced activation energy is formed. The measured activation energy is given approximately by the energy separation of the maximum valence band energy and the minimum acceptor energy. When L is sufficiently large this separation becomes zero as both of these values line up with the Fermi energy. Further increasing L does not lead to significant changes, since both the acceptor level and the valence band pin close to the Fermi level.

6.3 Modulation-doped superlattices

To determine the optimal modulation-doping scheme we examine the band-diagram shown in figure 6.10. In the absence of polarization fields the two types of AlGaN/GaN interfaces would be equivalent, but the polarization introduces charge sheets of opposite types at these interfaces. Assuming that the surface of the crystal is Ga-face (this is the case when MOCVD is used to initiate growth on sapphire),[14] a positive sheet charge is obtained when AlGaN is grown on GaN. In this region, labeled region A, the bands are pulled down so that the acceptor ionization rate is high but the mobile hole concentration is low. Acceptor doping in this region is very effective since many of the acceptors will be ionized. At the opposite interface, region B, a negative sheet charge is obtained and the bands are pulled up—holes accumulate here, but the acceptor

ionization rate is very low. Mg-doping in this region will not yield many holes, but may considerably reduce the mobility of the accumulated carriers.

A high hole mobility is expected even in the case of uniform Mg-doping because the polarization fields separate the mobile carriers from the ionized acceptors. The fairly low hole mobility values which were obtained in the uniformly-doped films are attributed to interface scattering and poor material quality due to the high Mg concentration. The latter problem can be eliminated through modulation Mg-doping limited to region A. We note that this modulation-doping scheme, where the dopant is applied across one interface, is very different from the traditional scheme used in non-polar materials where the dopant is typically confined to the center of the barrier.
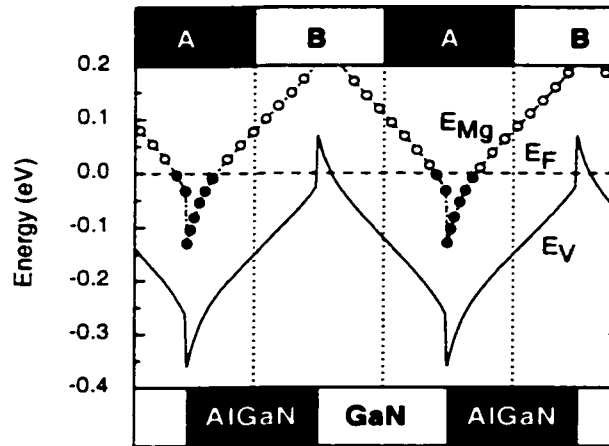

Figure 6.10 Calculated valence band diagram for Mg-doped $Al_{0.2}Ga_{0.8}N$/GaN superlattice with spontaneous and piezoelectric polarization fields taken into account. The thickness of each layer is L=80 Å. The dashed line indicates the Fermi energy, and the circles represent the energy of the Mg acceptor (solid when ionized). The regions A and B defining each interface are indicated. The sapphire substrate is on the left and the free surface of the film is on the right.

In order to achieve sharp dopant profiles, plasma-assisted molecular beam epitaxy (MBE) was used to grow the modulation-doped superlattice samples. The growths were performed at UCSB by Yulia Smorchkova. MOCVD-grown GaN base layers were used as the underlying template. Two $Al_{0.12}Ga_{0.88}N$/GaN superlattice samples were prepared, both with $L = 80$ Å. In each case the Mg-doping was applied through only half the structure, either in region A or in region B. The results of room-temperature Hall effect measurements on these samples are shown in table 6.1.

As expected, the sample doped only in region A exhibited both a higher hole concentration and a higher mobility value—the conductivity of this sample was almost an order of magnitude higher than that of the sample doped only in region B. This is an unambiguous demonstration of the crucial role played in these structures by polarization fields—without these fields the two interfaces are equivalent and so the two films should behave identically.

The sample doped only in region A also exhibits a higher mobility than the earlier, uniformly-doped samples. This increase is attributed both to the improved material quality due to modulation-doping and to reduced interface scattering due to a lower aluminum composition.

Sample	Doped Region	Hole Conc. (cm^{-3})	Mobility (cm^2/Vs)
1	A	1.9×10^{18}	19
2	B	6.8×10^{17}	5.6

Table 6.1   Room temperature Hall effect measurements on modulation-doped $Al_{0.12}Ga_{0.88}N$/GaN superlattices.

6.4 Conclusions

In conclusion, we have demonstrated highly conductive *p*-type AlGaN/GaN superlattices. Polarization effects create a periodic oscillation of the energy bands. This enhances the ionization of the deep acceptors and leads to the accumulation of carriers in hole sheets. Through this mechanism, the average hole concentration at room temperature is increased by more than a factor of ten over that achieved in a bulk AlGaN film; the enhancement at reduced temperature is more than five orders of magnitude. These structures can eliminate the strong temperature dependence of the conductivity that is obtained in bulk films, since the free carriers in the superlattice result not from thermal ionization but from band-bending produced by the polarization fields. Application of this technique to GaN-based laser diodes and LEDs may lead to a much wider range of operating temperatures for these devices. The superlattices will also be useful in any device layer requiring highly conductive lateral transport of holes (e.g. the sub-collector of a *p-n-p* transistor).

Despite the success of this superlattice scheme in producing p-type layers of low lateral resistivity, application of the technique in various device structures may introduce serious problems because the superlattice produces valence and conduction band barriers that will impede vertical carrier transport. For example, recent experiments at UCSB by Hansen, et al., demonstrated that the threshold voltage of a laser diode with a *p*-type AlGaN/GaN superlattice increases when the superlattice dimension *L* is increased. As a result, the long-period superlattices necessary for hole enhancement do not appear suitable for use in lasers designed for room-temperature operation.[15]

The barriers are also a problem for application to bipolar transistors, in which vertical electron flow occurs across the base layer. The conduction band barriers, due both to the polarization fields and the conduction band discontinuity, are expected to be large and severely disrupt current flow. In future work this

149

problem may be partially overcome through the use of quaternary alloys, allowing independent control of band line-up and lattice constant. However, even if the conduction band barriers are eliminated entirely, the superlattices may not be suitable for use in bipolar transistors. This is because the holes are still separated into sheets, and therefore unable to move back and forth to properly neutralize the injected electron concentration. This effect will result in a Coulombic "drag force" on the electrons crossing the base, which will degrade the high-frequency performance of the device.[16]

6.5 References

1   E. F. Schubert, W. Grieshaber, and I. D. Goepfert, "Enhancement of deep acceptor activation in semiconductors by superlattice doping." *Appl. Phys. Lett.* **69**, 3737-3739 (1996).

2   L. Hsu and W. Walukiewicz, "Theoretical transport studies of p-type GaN/AlGaN modulation-doped heterostructures." *Appl. Phys. Lett.* **74**, 2405-7 (1999).

3   S. Nakamura, M. Senoh, S. I. Nagahama, N. Iwasa, T. Yamada, T. Matsushita, H. Kiyoku, Y. Sugimoto, T. Kozaki, H. Umemoto, M. Sano, and K. Chocho, "InGaN/GaN/AlGaN-based laser diodes with modulation-doped strained-layer superlattices grown on an epitaxially laterally overgrown GaN substrate." *Appl. Phys. Lett.* **72**, 211-13 (1998).

4   A. Saxler, W. C. Mitchel, P. Kung, and M. Razeghi, "Aluminum gallium nitride short-period superlattices doped with magnesium." *Appl. Phys. Lett.* **74**, 2023-5 (1999).

5   T. Takeuchi, C. Wetzel, S. Yamaguchi, H. Sakai, H. Amano, I. Akasaki, Y. Kaneko, S. Nakagawa, Y. Yamaoka, and N. Yamada, "Determination of piezoelectric fields in strained GaInN quantum wells using the quantum-confined Stark effect." *Appl. Phys. Lett.* **73**, 1691-3 (1998).

6   E. T. Yu, G. J. Sullivan, P. M. Asbeck, C. D. Wang, D. Qiao, and S. S. Lau, "Measurement of piezoelectrically induced charge in GaN/AlGaN heterostructure field-effect transistors." *Appl. Phys. Lett.* **71**, 2794-6 (1997).

7   A. D. Bykhovski, B. L. Gelmont, and M. S. Shur, "Elastic strain relaxation and piezoeffect in GaN-AlN, GaN-AlGaN and GaN-InGaN superlattices." *J. Appl. Phys.* **81**, 6332-6338 (1997).

8   F. Bernardini and V. Fiorentini, "Spontaneous polarization and piezoelectric constants of III-V nitrides." *Phys. Rev. B* **56**, R10024 - R10027 (1997).

9   D. L. Smith and C. Mailhiot, "Piezoelectric effects in strained-layer superlattices." *J. Appl. Phys.* **63**, 2717-19 (1988).

10   The simulation program used, "1D-Poisson" by G. L. Snider, is available through the internet at http://www.nd.edu/~gsnider.

11 J. H. Edgar, *Properties of Group III Nitrides* (INSPEC, London, 1994).

12 A. F. Wright, "Elastic properties of zinc-blende and wurtzite AlN, GaN, and InN." *J. Appl. Phys.* **82**, 2833-9 (1997).

13 Y. Zhang and J. Singh, "Charge control and mobility studies for an AlGaN/GaN high electron mobility transistor." *J. Appl. Phys.* **85**, 587-594 (1999).

14 F. A. Ponce, D. P. Bour, W. T. Young, M. Saunders, and J. W. Steeds, "Determination of lattice polarity for growth of GaN bulk single crystals and epitaxial layers." *Appl. Phys. Lett.* **69**, 337-339 (1996).

15 M. Hansen, A. C. Abare, P. Kozodoy, T. M. Katona, M. D. Craven, J. S. Speck, U. K. Mishra, L. A. Coldren, and S. P. DenBaars, "Effect of AlGaN/GaN strained layer superlattice period on InGaN MQW laser diodes." *Phys. Status Solidi (a)* **176**, 59-62 (1999).

16 H. Kroemer, private communication (1998).

Chapter 7

Conclusions and future work

7.1 Growth, processing, and characterization

The research presented in this dissertation has focused in large part on developing successful recipes for the growth and processing of Mg-doped p-type GaN. These experiments have provided insight into a number of fundamental issues for this material and have also yielded recipes that have proved useful for fabricating a wide range of devices (see section 1.4).

MOCVD growth of Mg-doped GaN was studied extensively in this dissertation, and a number of conclusions can be stated on this topic. SIMS measurements indicate that Mg incorporation into the crystal is a fairly well behaved process. The incorporation efficiency does depend on reactor pressure, however, and exhibits a very strong memory effect. The latter is a major problem and prevents the achievement of sharp dopant profiles. The memory effect is expected to be strongly dependent on reactor geometry in MOCVD; it can be avoided entirely by using MBE growth.

Hall effect measurements on bulk Mg-doped GaN layers reveal a number of phenomena. Using this technique, the acceptor binding energy has been measured, and was found to depend strongly on the dopant concentration. The doping efficiency was observed to peak at a Mg concentration of 2×10^{20} cm^{-3}. Perhaps the most important conclusion in this area is that high compensation levels are found in heavily doped films, with severe consequences for the hole mobility. The hole concentration is also reduced by compensation, but the effect is partially offset by the binding energy reduction which accompanies the

increased compensation level. The nature of the compensating species is unknown, but one candidate is the nitrogen vacancy. Indeed, the compensation level is observed to rise during growth under nitrogen-poor conditions.

Growth in a nitrogen-rich atmosphere may therefore be expected to help somewhat in reducing the density of compensating donors in Mg-doped GaN films. In future work, this could be achieved by increasing the NH_3 cracking efficiency, either through a modified reactor design or by pre-cracking the NH_3 before injection. An interesting approach would be to use UV or microwave radiation to help dissociate the NH_3 molecules.

Growth at higher temperatures may also help to reduce compensation by providing a more nitrogen-rich atmosphere. The experiments on growth temperature described in section 2.8 suggest that this may be the case, but that other effects may limit the hole concentration achieved under these conditions. This is an area that deserves further investigation. For this study, and indeed for all growth studies, temperature-dependent Hall effect measurements are a very important tool. An easier process and more accessible measurement setup for obtaining these measurements at UCSB would greatly facilitate future experimental work.

Another important issue for the growth of Mg-doped GaN is determining how many of the Mg atoms incorporate on the desired sites, and how the incorporation in other locations may be reduced. Electrical measurements are not the most direct way of answering these questions—structural characterization techniques are needed. Raman spectroscopy measurements may be useful in this regard, and transmission electron microscopy (TEM) is likely to be a very important tool.

TEM measurements of Mg-doped GaN have received little attention in the literature, but should be very useful in detecting Mg precipitation or the formation of Mg_3N_2 inclusions. This sort of microscopy work on Mg-doped GaN has

154

recently begun in earnest at UCSB and the results, while preliminary, are quite promising. For example, figure 7.1 shows a TEM image of a stack of Mg-doped layers (the TEM work was performed by Lifan Chen). In this film, alternating layers were grown at atmospheric pressure and 76 torr; this Mg-doped stack was grown on a Si-doped template. A contrast is visible in TEM both between the Si-doped and Mg-doped regions, and between the individual Mg-doped layers. The latter contrast is presumably related to the higher Mg concentration in the low-pressure-grown layers (the Mg profile for this sample was measured by SIMS and is shown in section 2.7). A detailed analysis of these TEM results is currently underway and should reveal whether or not the presence of small precipitates or inclusions is responsible for the contrast. An increasing effort in microscopy of Mg-doped GaN may also yield useful information about the interaction of the Mg atoms with the threading dislocations within the film, as well as the structural consequences of very high Mg doping densities.
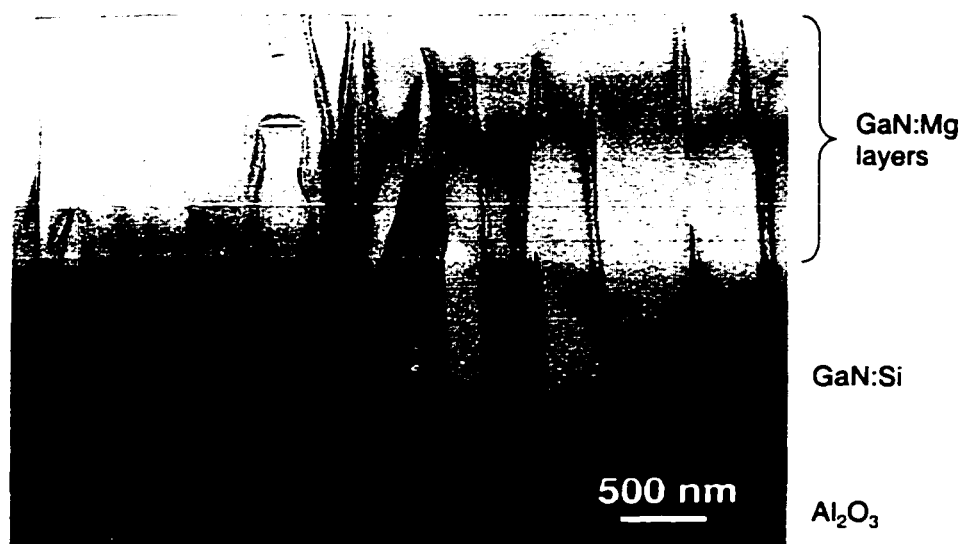

Figure 7.1   TEM image of Mg-doped GaN layers grown on top of Si-doped GaN.   Contrast is visible between the Si-doping and the Mg-doping, as well as between different Mg-doped layers. The Mg dopant concentration in the layers alternates between two different values.

A number of processing issues have also been addressed in this dissertation. Recipes for the activation anneal and p-contact preparation have been presented, and the issue of plasma-induced damage has been investigated in some detail. Experimental work in this area was complicated by significant problems with material variation, both between growth runs and over the area of a single wafer. Greater material uniformity will be needed in future work in order to fine-tune these process recipes. The inhomogeneity problem may be reduced somewhat in the near future as the MOCVD facilities at UCSB evolve and more uniform epitaxial tools come on-line; whether the run-to-run variation may be brought under strict control remains to be seen.

A number of experiments were performed on the optimization of the activation anneal procedure. Short, high-temperature anneals appear to provide the best results. Surface damage may occur at these high temperatures, and the use of a capping layer (usually SiO_2) was found to help preserve the surface. Additional experiments in high-temperature annealing, perhaps under a high N_2 pressure, may prove useful in further optimizing the procedure.

A fairly successful ohmic contact scheme using a Pd/Au metallization was developed. In addition, a detailed analysis of the current flow characteristics of these slightly-non-ohmic contacts has been performed—this discussion is presented in appendix B. Proper surface preparation was found to play an important role in achieving low-resistance contacts. Annealing the Pd/Au contacts at 650 °C led to a significant drop in contact resistance. This annealing procedure needs to be more carefully investigated; an even lower contact resistance is expected once the anneal temperature and time have been fully optimized. It is also important to develop an understanding of the mechanism for the contact resistance reduction. TEM measurements will be useful for identifying new phases that may be formed during the anneal, and SIMS may be used to investigate the possibility that hydrogen is gettered into the metal.

The issue of plasma damage to p-type GaN has also been investigated in this dissertation. The p-GaN surface was found to be extremely sensitive to plasma damage, and only Schottky-type contacts were obtained on plasma-exposed surfaces. Lowering the plasma power helped to minimize the damage. Plasma processing should be avoided whenever possible, but unfortunately cannot be eliminated altogether since there is presently no viable alternative for etching GaN.

A number of approaches should be investigated to address the issue of plasma-induced etch damage. Inductively coupled plasma etching systems offer a dense, low-energy plasma source that may produce significantly less damage than the reactive ion etching configuration employed in this work. Another possible approach is to remove the plasma-induced damage in a clean-up step using wet chemical treatments. Preliminary experiments in this area were unsuccessful, but there are a number of possible chemical treatments that deserve careful testing. The best approach would likely be to eliminate the plasma exposure altogether by using photo-electrochemical (PEC) etching. This technique also offers the advantage of type-selective etching, which could be very useful for processing devices such as bipolar transistors. It currently remains unproven, however, that PEC etching can, in fact, be used to expose p-GaN layers without surface damage. Considerable further work is needed both to qualify this etch technique and to develop it into a practical device processing tool.

7.2 Device issues

Aside from the need for more conductive *p*-type material and improved contact technologies, one of the main issues for device performance is the presence of deep levels within the GaN layers. Using lateral epitaxial overgrowth (LEO), we have shown that some of these levels are associated with threading dislocations within GaN, and that these are responsible for the high reverse-bias leakage current observed in GaN *p-n* junctions. Dislocation-free diodes formed on LEO GaN display a much lower leakage current, a discovery which has already seen application in photodiodes. However, even in the dislocation-free diodes, some leakage current remains; this may be due to point defects within the crystal or surface damage on the etched side-wall of the device.

The forward bias characteristics of GaN *p-n* junctions are still not understood. The I-V behavior deviates significantly from the ideal junction equation, and does not appear to be affected by the presence or absence of dislocations. In order to determine the forward current flow mechanism, further experiments that examine the I-V characteristics as a function of temperature are needed. These experiments should be performed on a number of devices grown under different conditions so that the factors affecting the I-V characteristics may be identified.

There is another type of deep level in this material, one which cannot be eliminated: the Mg acceptor level itself. While this level may be too shallow to play a major role in generation and recombination, it can be a source of dispersion during high-frequency operation. The deep acceptor level will also impact the DC depletion region, which was found to vary significantly in Mg-doped GaN from the depletion region obtained in the usual case with shallow dopants.

The finite response time of the Mg acceptor will lead to both small-signal and large-signal dispersion effects. The former effect has been measured

experimentally in GaN *p-n* junctions; the experimental data agrees fairly well with the results of analytical calculations. The large-signal effect will be of much greater significance, especially for the efforts to produce high-power and high-frequency GaN-based bipolar transistors. The device consequences of this dispersion effect are discussed in chapter 5, however the magnitude of the large-signal effect is difficult to calculate and will not truly be known until AC measurements are performed on these transistors.

7.3 Using polarization effects

The deep nature of the Mg acceptor is a fundamental problem that currently limits the hole concentration which may be achieved in GaN; it also leads to a strong temperature dependence in the electrical properties of these layers. The nitride material system supports very strong polarization fields, however, and this phenomenon may be used in various schemes to address some of the limitations posed by the deep Mg acceptor.

One such technique is the AlGaN/GaN superlattice discussed in chapter 6. This superlattice makes use of polarization effects to provide an oscillation in the energy of the valence band edge, allowing holes to collect in sheets at alternate interfaces where the valence band edge is pulled up to the Fermi level. The technique results in enhanced hole concentrations that are maintained even at very low temperatures. Modulation doping experiments have confirmed that polarization effects play a pivotal role in the operation of the superlattice. The superlattice scheme demonstrates the potential for using polarization effects as an engineering tool, and may prove useful in selected device applications. However, the large barriers to vertical conduction that are imposed by the heterointerfaces may make this technique unsuitable for most device structures.

Figure 7.2 shows the calculated sheet charge density due to polarization effects that will occur at the interface between a relaxed GaN template and a strained alloy layer. These sheet charge values were calculated using the method and references detailed in chapter 6. For AlGaN, the charge density due to the piezoelectric effect and the difference in spontaneous polarization are comparable in magnitude, while for InGaN the effect of spontaneous polarization is quite minor. When grown on a GaN template, InGaN is in compression while AlGaN is in tension. Because of the opposite strain sign, the piezoelectric effect causes opposite polarization fields in the two types of layers (the values shown in figure 7.2 give only the magnitude of the charge sheets which are formed).
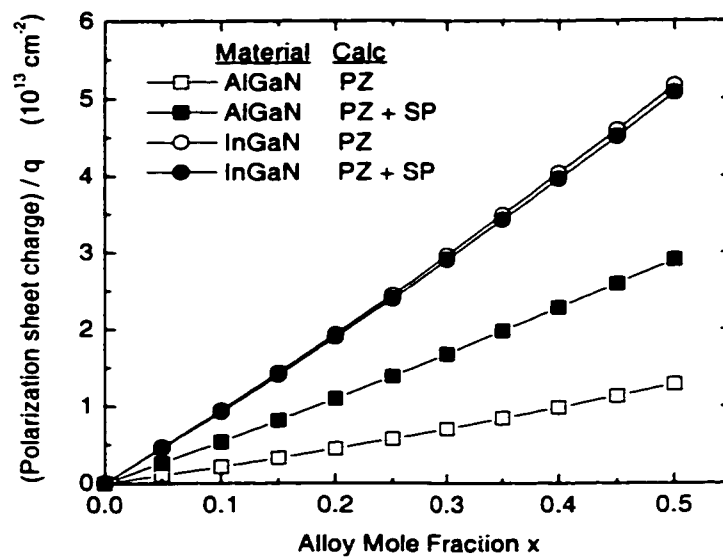

Figure 7.2 Polarization sheet charge at an interface between a strained alloy layer and a relaxed GaN film. The magnitude of the sheet charge, divided by the electronic charge q, is plotted. The squares represent AlGaN alloys and the circles represent InGaN; open symbols are calculations based solely on the piezoelectric effect (PZ) while solid symbols also take into account differences in spontaneous polarization (PZ+SP).

The sheet charge densities shown in figure 7.2 are very large—the polarization charge at heterointerfaces can easily be sufficient to provide volts of band-bending over very short distances. Alternatively, the alloy composition may be graded instead of changed abruptly at a heterointerface. An alloy grade distributes the sheet charge over an extended volume. Using a 1000 Å grade, for example, space-charge densities around 10^{18} cm^{-3} are calculated. This is a very high space-charge density, comparable to that typically achieved in heavily-doped layers. The polarization effects are therefore very powerful tools for band-diagram engineering, and will likely be a major topic of future research.

A distributed negative space-charge created by an alloy grade will act very much like negative ionized acceptors, and will attract mobile holes in order to achieve space-charge neutrality. To preserve overall neutrality, the holes will be balanced by electrons accumulated elsewhere in the device (most likely where the positive polarization charge resides). This technique therefore holds the promise of p-type layers achieved without any actual acceptor doping. The resulting material would offer a high hole mobility due to the absence of ionized impurities,

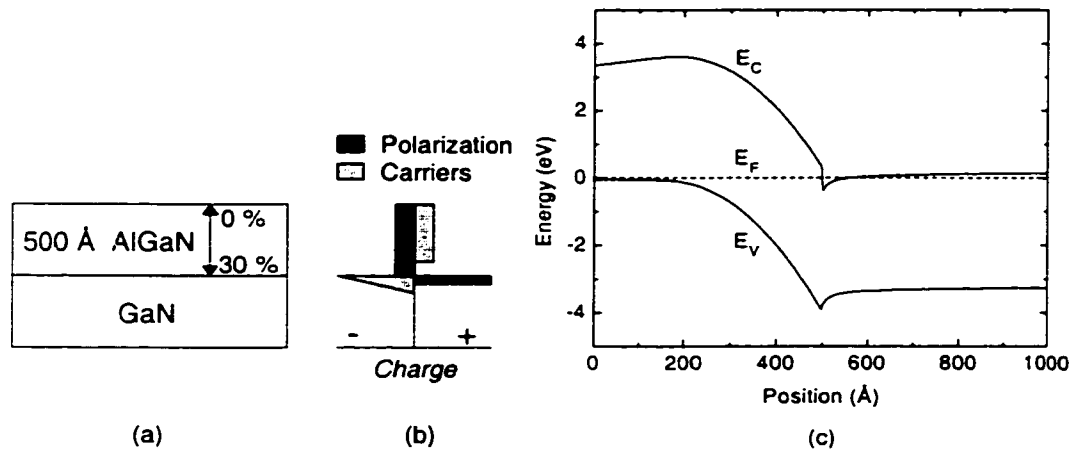(a)   (b)   (c)

Figure 7.3 JHEMT device structure formed using polarization effects. The layer structure (a), charge distribution (b), and band diagram (c) are shown.

and should be free of memory effect and dispersion issues. Two possible device structures based on this technique are described below.

A junction-gated high electron mobility (JHEMT)-like structure may be produced using these polarization effects. A GaN buffer layer would be grown first, followed by an abrupt transition to AlGaN. The growth would be finished by grading the aluminum composition of the barrier layer down to zero at the surface. This alloy grade will produce a negative polarization space-charge within the barrier layer. Holes will therefore accumulate in the AlGaN layer and balance the charge of the two-dimensional electron gas, forming a p-n junction-like structure. This device structure is shown in figure 7.3.

Polarization effects could also be used to replace the Mg-doping in the base layer of n-p-n bipolar transistors. Unfortunately, the alloy grade that is required in order to achieve p-type material also causes a quasi-electric field that opposes vertical electron transport in a downward direction. This quasi-electric field in the base layer would severely degrade device performance. In order to
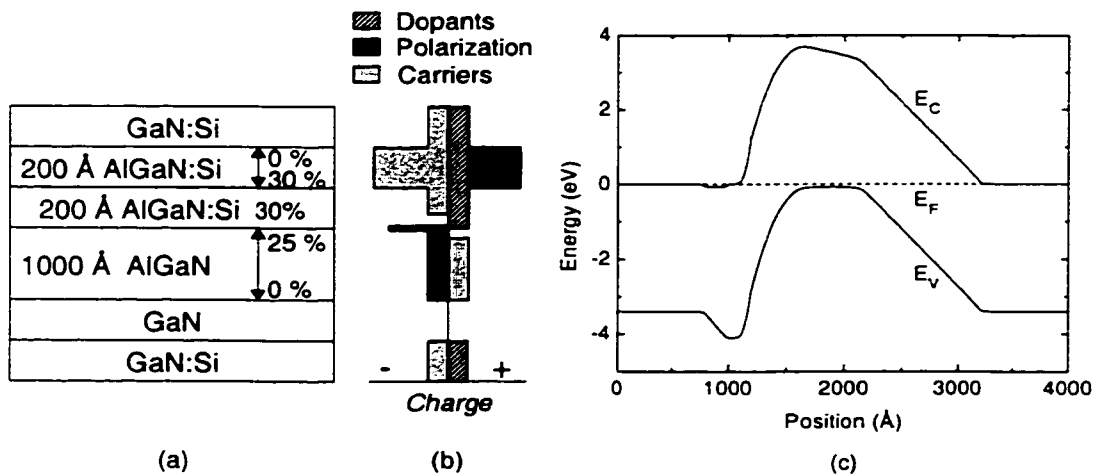

Figure 7.4   HBT structure formed using polarization effects. The structure is grown on N-face GaN in order to flip the polarization fields. The layer structure (a), charge distribution (b), and band diagram (c) are shown.

162

avoid this, either the layer order must be flipped, creating a collector-up design (some undercut technique would then have to be employed to aperture the emitter current), or the sign of the polarization fields must be flipped. The latter could be achieved using growth on a N-face GaN substrate, once such material becomes available. Either technique would result in a quasi-electric field that *aids* electron transit across the base, just as in a traditional graded-base HBT. Figure 7.4 shows the structure of such a device, using a graded AlGaN layer to create the *p*-type base. The holes accumulated there are offset by electrons near the emitter-base junction.

These device designs represent an exciting area for future work, promising bipolar devices formed without acceptor doping (although Mg acceptors may still be needed in thin contact regions in order to achieve ohmic contacts). In order to achieve these devices, it will be important to limit the density of defects and unintentional dopants; these may compensate the polarization-induced space-charge and prevent the necessary band-bending.

Some preliminary experimental work was performed on this type of device structure, but *p*-type conduction without Mg doping has not yet been convincingly demonstrated. Deep defect formation is probably the major stumbling block that currently limits work in this field. Better substrates and an improved understanding of growth conditions may allow future workers to overcome these problems. If so, polarization engineering may emerge as an important new technology that may be used to address the fundamental limitations of the deep Mg dopant.

Appendix A

Standard processing recipes

A.1 Activation

1. Solvent clean
   - Acetone ultrasonic treatment, 1 minute
   - Isopropanol ultrasonic treatment, 1 minute
   - Rinse with DI water, 1 minute
   - Blow dry with N_2
2. Deposit SiO_2 cap
   - Clean PECVD chamber by running program "30clnsio"
   - Deposit 1000 Å SiO_2 (program "sio10")
3. Anneal
   - Anneal in RTA at 950°C for 3 minutes, in N_2 atmosphere
   - Use clean Si carrier wafer
   - Perform test run of RTA before loading samples
4. Remove SiO_2 cap
   - Soak in BHF, 10 minutes
   - Rinse in DI water, 1 minute
   - Blow dry with N_2

A.2 Ohmic contact

1. Solvent clean
   - Acetone ultrasonic treatment, 1 minute
   - Isopropanol ultrasonic treatment, 1 minute
   - Rinse with DI water, 1 minute
   - Blow dry with N_2

2. Image-reversal photolithography
   - Dehydration bake in 120 °C oven, 15 minutes
   - Allow samples to cool, 3 minutes
   - Spin HMDS 6000 RPM, 40 seconds
   - Spin 5214 photoresist 6000 RPM, 40 seconds
   - Softbake 95 °C hotplate, 1 minute
   - Expose with mask, 7.5 W/cm^2 UV light power, 9 seconds
   - Image reversal bake 110 °C hotplate, 1 minute
   - Flood expose, 7.5 W/cm^2 UV light power, 30 seconds
   - Develop in AZ400K:DI 1:5.5, ~ 45 seconds
   - Second exposure: flood expose, 7.5 W/cm^2, 1 minute
   - Develop in fresh AZ400K:DI 1:5.5, 15 seconds
3. Acid dip
   - Soak in HCl, 20 seconds
   - Rinse in DI water, 1 minute
   - Blow dry with N_2
4. Metal evaporation
   - Evaporation in thermal evaporator: 200 Å Pd, 2000 Å Au
   - Base pressure: ~ 7×10^{-7} torr
   - Evaporation rate: ~ 1 Å/sec for Pd, ~ 5 Å/sec for Au
5. Lift-off
   - Soak in acetone 10 minutes
   - Finish lift-off with acetone spray and/or ultrasonic dip
   - Ultrasonic isopropanol clean, 1 minute
   - Rinse in DI water, 1 minute
   - Blow dry with N_2

Appendix B

TLM Measurements on non-ohmic contacts

The transfer length model (TLM) method of characterizing contact resistance is commonly used in semiconductor processing characterization. When ohmic contacts are obtained, the method is straightforward and provides a simple contact characterization technique. When the contacts are not perfectly ohmic, however, the analysis must be considered much more carefully.

We first briefly summarize the technique as applied with perfectly ohmic contacts. A good discussion is provided in *Modern GaAs Processing Methods* by Ralph Williams (Artech House, Boston, 1990). A series of contact pads separated by different spacings, L, are prepared on the wafer. Each contact pad has width W, and they are placed upon a conducting layer of thickness t. A mesa is etched around the entire pattern so that current is constrained to flow directly between the two contacts being tested. This arrangement is shown in figure B.1. The resistance between any two adjacent pads will be given by
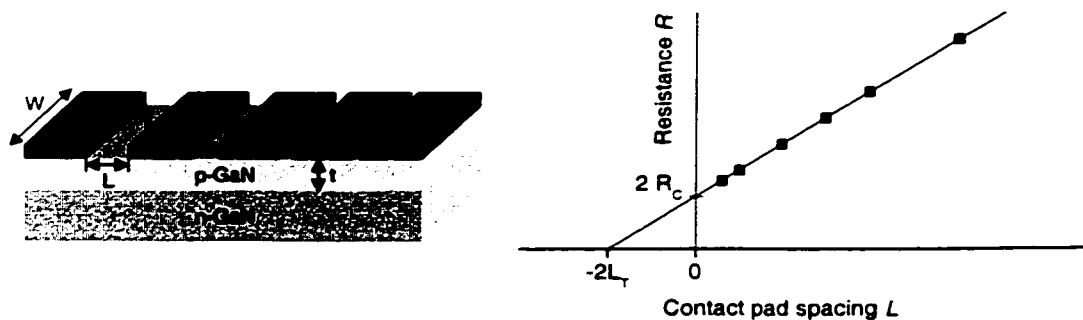

Figure B.1 Diagrams of TLM measurement configuration (left) and fitting procedure (right).

$$R = 2R_C + R_{SH}\left(\frac{L}{W}\right) = 2R_C + \frac{\rho L}{tW}, \tag{B.1}$$

where R_C is the contact resistance, R_{SH} is the sheet resistance and ρ is the resistivity of the layer. The contact resistance R_C may be obtained from the y-intercept of a line-fit to a plot of R as a function of L (see figure B.1). The x-intercept of this plot gives twice the transfer length L_T (here we assume that the sheet resistance does not change under the contact, a safe assumption for non-alloyed contacts):

$$L_T = W(R_C / R_{SH}). \tag{B.2}$$

This transfer length represents the active part of the contact. The specific contact resistance r_C is the resistance presented by the contact to uniform vertical current flow over a unit area. Its value is given by
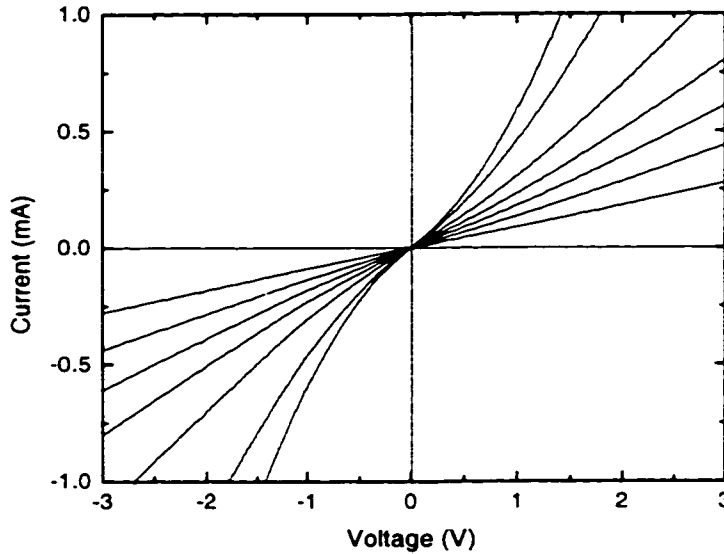
$$r_C = R_C W L_T, \tag{B.3}$$

Figure B.2   I-V characteristics obtained from a set of TLM pads. The contact width W is 200 μm, the spacings L are 3, 5, 10, 15, 20, 30, and 50 μm.

168

which is equivalent to assuming that R_C is due to a uniform current flow through the active contact area $A_{EFF} = L_T W$.

The current flow from underneath the contact may be modeled as a semi-infinite resistor network, in which each node is separated by a distance dx. The resistance to lateral current flow through the semiconductor is therefore $(R_{SH} dx/W)$, while the resistance to vertical current flow into the contact is $(r_C W dx)$. When this system is analyzed, both the lateral current flow through the semiconductor and the vertical current flow into the contact are found to fall off as $\exp(-x/L_T)$ where x is the distance under the contact.

We now turn our attention to the case where the contacts are not quite ohmic. Figure B.2 shows the I-V characteristics obtained from TLM patterns formed by non-alloyed Pd/Au contacts on Mg-doped p-type GaN. The non-ohmic nature of the contacts is particularly evident in the curves for small values of L, where the resistance of the bulk layer is small. In this case, it is important to realize that the contact is not characterized by a single resistance but instead by a
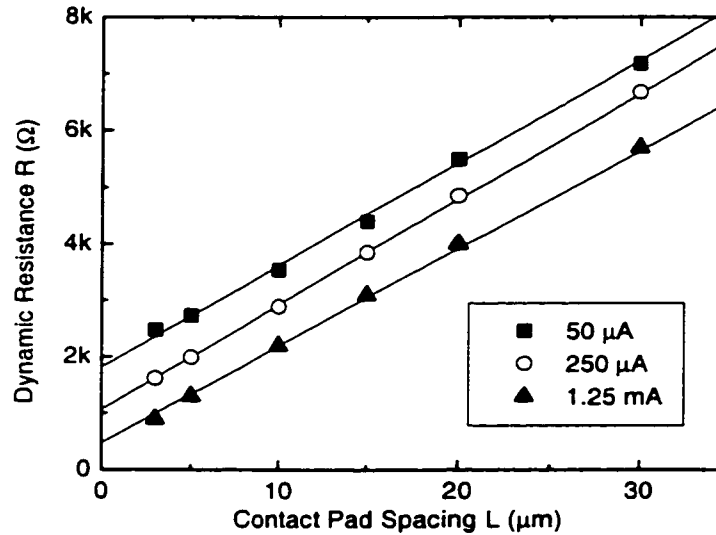

Figure B.3 TLM fit of the dynamic resistance as a function of pad spacing L. The total current is varied.

169

particular, non-linear, I-V curve. The voltage that will be measured between two contacts at a particular current level will be determined by the contact voltage at that current level $V_{CONT}(I)$, as well as by the sheet resistance:

$$V(I) = 2V_{CONT}(I) + I \times R_{SH}\left(\frac{L}{W}\right),$$ (B.4)

assuming the contact I-V characteristic is symmetric.

If the dynamic resistance at a particular current is measured from the slope of the I-V curve at that current level, equation (B.1) may be used to find the contact resistance R_C. In this case R_C represents the *dynamic contact resistance at the current level used.* Figure B.3 shows such TLM fits carried out at different current levels; these are based on the same I-V curves displayed in figure B.2. The results show the expected result that the contact resistance obtained depends strongly on the measurement current value.
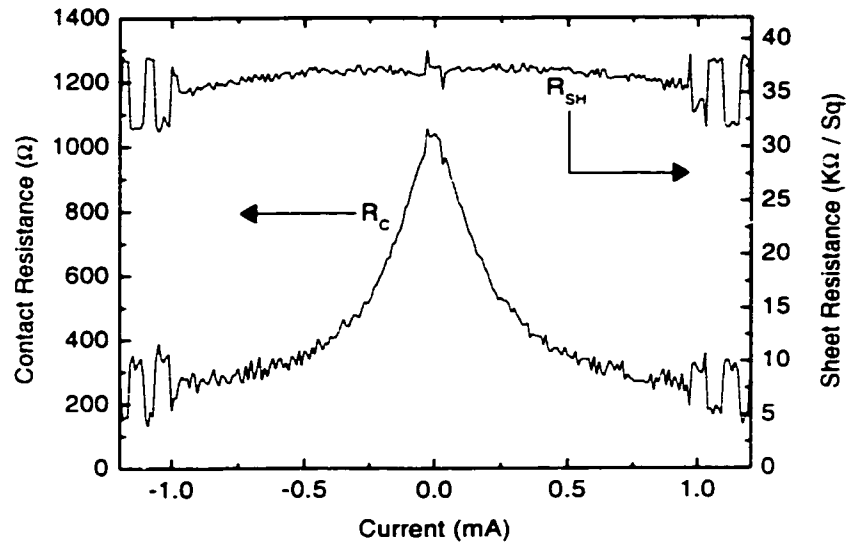

Figure B.4 Contact resistance and sheet resistance obtained from TLM fit as a function of current level.

170

Using a spreadsheet, the I-V curves presented in figure B.2 have been fit to the TLM model at every current value measured. The resulting values of R_C and R_{SH} are shown in figure B.4. As expected, the sheet resistance is independent of measurement current but the contact resistance exhibits a dramatic peak at low current levels. The oscillations seen at high current levels are a measurement artifact.

Based upon the measured values of R_C and R_{SH}, we could now forge ahead and calculate L_T and r_C. However, it is not clear that these values are necessarily meaningful. It is important to remember that in this case the measured contact resistance is actually a *dynamic* resistance value. The semi-infinite resistor network model is not valid in our case because the contact cannot be described as a resistor. Therefore if the transfer length is calculated in the standard way, the value will not necessarily correspond to the true active area of the contact, and there is no guarantee that equation (B.3) will yield correct values of r_C. The true
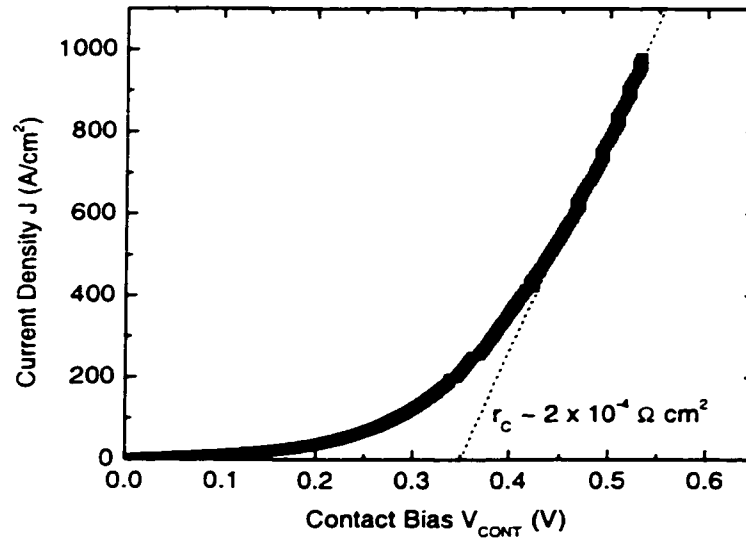

Figure B.5 Plot of current density J as a function of bias drop across the contact V_{CONT}. The line fit to the high-bias data gives the specific contact resistivity r_C at high current values.

171

active contact area is important to know not only for calculating r_C, but also because it is an important parameter for device design (e.g. for determining the necessary size of the base contact metal in a bipolar transistor).

It stands to reason that the standard transfer length equation will be approximately correct for contacts that are only slightly non-ohmic, while it is completely invalid for contacts that are totally Schottky in nature. The important question is whether the contacts in this case are sufficiently ohmic for the equation to be valid. In order to investigate this, we first assume that the transfer length can be calculated in the standard way, and then use the results to simulate the original I-V curves; if these simulated curves match well with the measured ones, the method is judged sound.

The first step is to find an approximate formula for the I-V characteristic of the contact $V_{CONT}(J)$. We extracted the numerical data for the function $V_{CONT}(I)$ according to equation (B.4), subtracting the voltage drop due to the sheet resistance from the I-V curve measured between two pads separated by 3 μm. We note again that this equation assumes that the voltage drop is equally divided between the two contacts. This assumption is most likely incorrect as more of the voltage is expected to drop across the reverse-biased contact.

Next we must calculate the current density. This is done by assuming that the current flows uniformly through an active contact area of $A_{EFF} = L_T W$, in
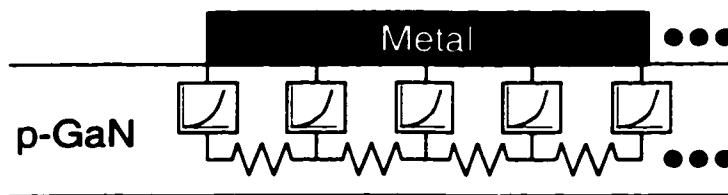

Figure B.6   Schematic diagram of the finite element model discussed in the text.

analogy with the conventional case, in which this approximation yields the correct result. The transfer length here is calculated according to the standard formula (B.2); it is in this step that the validity of this equation is assumed. We now have two sets of data: $V_{CONT}(I)$ and $J(I)=I/A_{EFF}$. Figure B.5 shows a scatter plot of this data in which V_{CONT} is placed on the x-axis and J is placed on the y-axis. The resulting curve is the desired $V_{CONT}(J)$ relation which characterizes the contact properties. From this data it appears that the contact has a "turn-on" voltage of approximately 350 mV, and a specific contact resistance at high current levels of 2×10^{-4} Ω cm^2. A numerical routine was used to fit the data to a third-order polynomial equation, providing a formula labeled $J_{FIT}(V)$, which describes the characteristics of the contact.

We next prepare a finite-element model of the current flow. This is analogous to the semi-infinite resistor network, but the contact is modeled with a full J-V curve, as indicated in the diagram shown in figure B.6. The finite
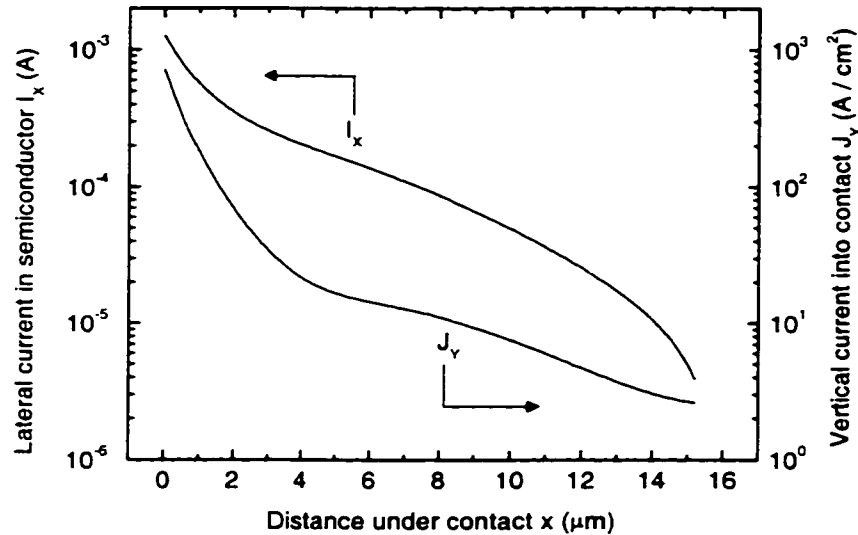

Figure B.7 Lateral and vertical current flow I_X and J_Y underneath the contact. The plotted data were calculated using the finite element model.

element calculations were carried out in a spreadsheet. An input current was specified and the contact voltage V_{CONT} was adjusted until the model converged. At each position x under the contact, the spreadsheet calculated the voltage in the semiconductor (V_{SC}), the current flowing vertically into the contact (J_Y), and the current flowing laterally through the semiconductor (I_X). The equations for a standard node (number i) are given below:

$$V_{SC,i} = V_{SC,i-1} + I_{X,i-1} R_{SH}\left(\frac{dx}{W}\right),$$ (B.5)

$$J_{Y,i} = J_{FIT}(V_{CONT} - V_{SC,i}),$$ (B.6)

$$I_{X,i} = I_{x,i-1} - Wdx\, J_{Y,i}.$$ (B.7)

Figure B.7 shows a plot of I_X and J_Y as a function of x, the distance under the contact, which was obtained using the finite element model to find the current distribution at a particular total current level I. The effect of the non-ohmic
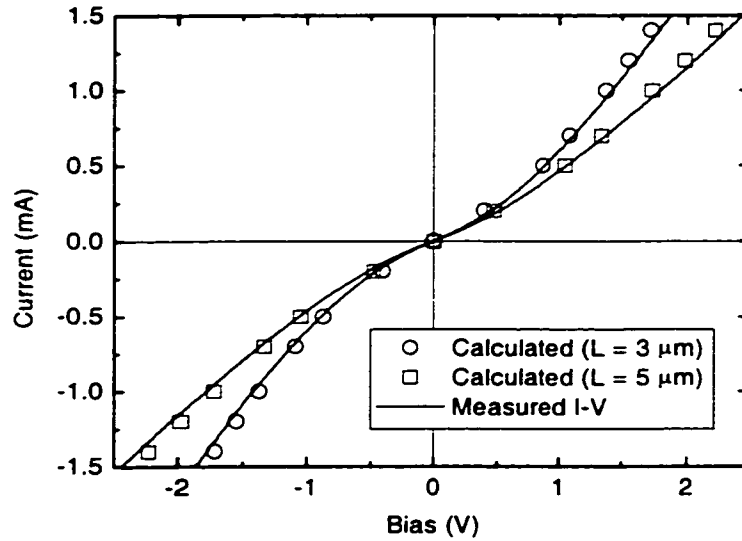

Figure B.8 Total voltage calculated as a function of current for a pad spacing of 3 μm (open circles) and 5 μm (open squares). The data are compared to the measured I-V curves for these spacings.

contact is clearly visible in this plot. Because this model is different from the standard resistor network, neither I_X nor J_Y is observed to fall off exponentially— instead a more complicated dependence is evident for both. In addition, the distance in which the current drops by a factor of $1/e$ is different for the two directions.

The finite element model was used to find the value of V_{CONT} for several different values of the total current I. The total voltage drop between two contacts was then calculated according to equation (B.4). The resulting calculated values are compared to the measured I-V curves in figure B.8. The two are observed to match fairly closely, indicating the validity of this overall procedure.

We conclude that the transfer length can be safely used to estimate the active contact area of these Pd/Au contacts, and that equation (B.3) may be used to calculate values of the specific contact resistance r_C at a particular current level I. (Such values are used extensively in chapter 3 to characterize contact quality.)
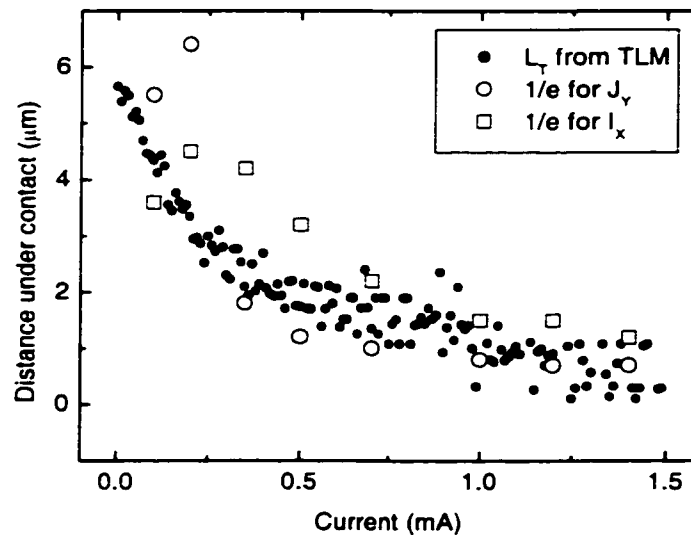

Figure B.9 Comparison of transfer length L_T from TLM fit (solid circles) and 1/e length for J_Y (open circles) and I_X (open squares) calculated using the finite element model.

The full-blown finite element model that has been developed in this appendix is also very useful for providing a more detailed understanding of the current flow under the contact. Figure B.9 shows the transfer length L_T calculated at each total current value I, as well as the $1/e$ distance for both I_X and J_Y at the particular current values to which the finite element model was applied. It is clear that the transfer length provides a fairly accurate estimate of the minimum contact length required at high current values, but becomes increasingly less accurate at low current levels. These results may be of importance in the design of base contacts for high-speed GaN based bipolar transistors.